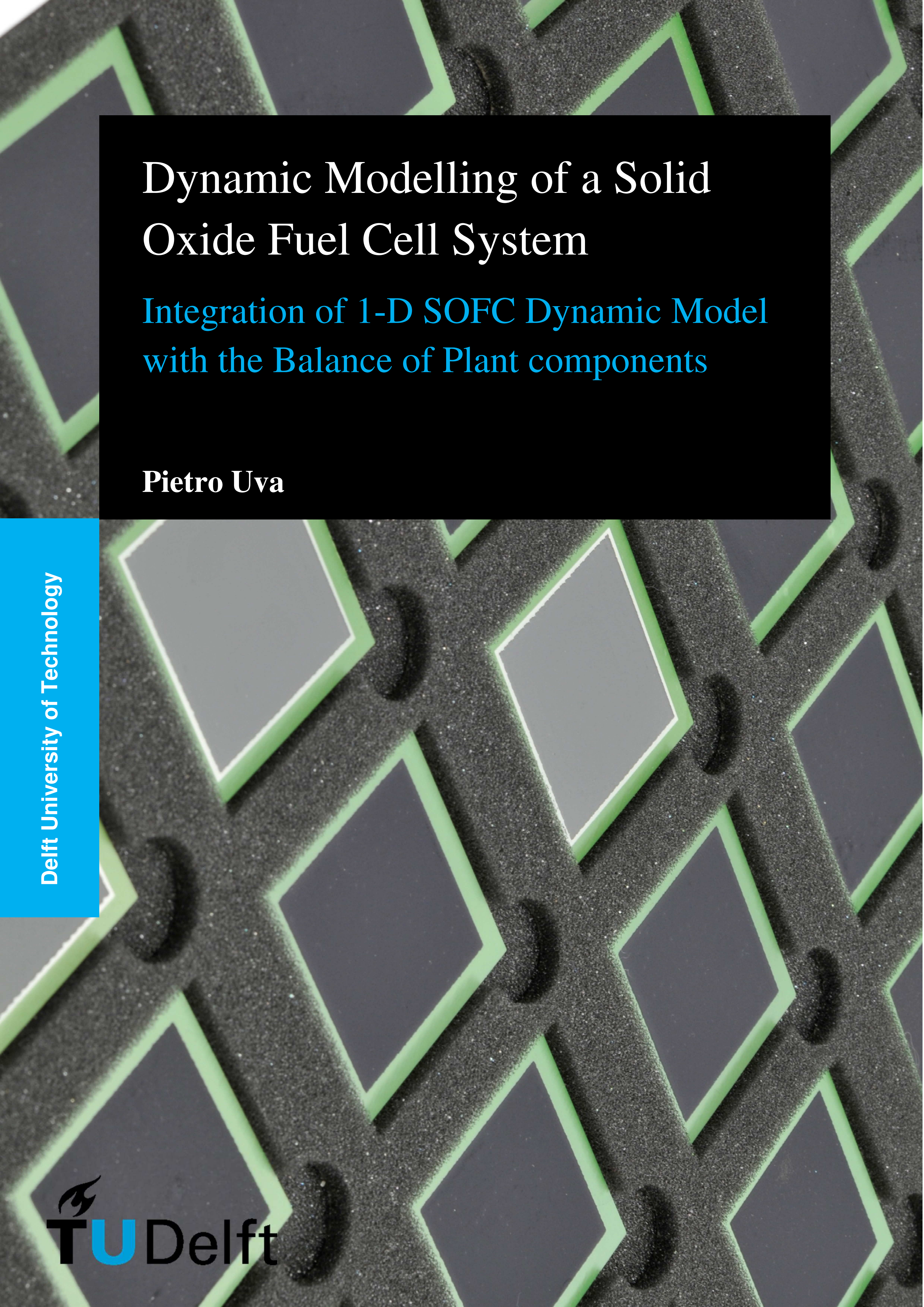

Dynamic Modelling of a Solid Oxide Fuel Cell System

Integration of 1-D SOFC Dynamic Model with the Balance of Plant components

Pietro Uva

Delft University of Technology

Dynamic Modelling of a Solid Oxide Fuel Cell System

Integration of 1-D SOFC Dynamic Model with the Balance of Plant components

by

Pietro Uva

In partial fulfilment of the requirement for the degree of

Master of Science
in Marine Technology

at the Delft University of Technology
to be defended publicly on September the 29th, 2020 .

Student number :	4787870
Thesis number :	SDPO.20.024.m.
MTI report number :	AO 165

Thesis committee :

Ir. K. Visser	TU Delft, Chairman
Dr.Ir. L. van Biert	TU Delft, Supervisor
Ir. B.T.W. Mestemaker	Royal IHC, Supervisor
Dr. C. De Servi	External Committee Member

To my very big family...

Abstract

The constant pressure on the maritime sector to reduce Greenhouse Gas (GHG) emissions has led the shipping industry to search for alternatives, such as zero-emissions propulsion systems, which would allow meeting the 2050 target imposed by International Maritime Organization (IMO) regulation. Fuel cells have demonstrated to substantially contribute to the greening of energy conversion technologies. Specifically, Solid Oxide Fuel Cells have proven to be a reliable technology to produce energy from Liquid Natural Gas (LNG). However, the limited understanding of the effect of the components around the stack (also known as Balance of Plant, BoP) in SOFC power generation system represents one of the reasons of the slow development of this technology. Therefore, developing a model which predicts the performance of a complete SOFC power generation system, would allow studying the dynamic loads and all the possible system modification without resulting in the higher costs and the time required of a real system modification.

Extensive literature studies have been conducted on modelling and simulation of the performance of single or multiple cell SOFC systems. Either by analysing only the time evolution of the system itself or by estimating both time and space variation of the system characteristics. However, relatively few research has been done on how the performance and the dynamics of the BoP components influence the efficiency and the load following capabilities of an SOFC power generation system.

The main objective of this research is to gain insight in the performance of the BoP components and their influence on the SOFC power generation system for maritime applications. A dynamic model describing a complete SOFC power generation system is developed in this work. The chosen system configuration consists of three blowers, two heat exchangers, a mixer, an external pre-reformer, an SOFC stack and an afterburner. Specifically, each BoP component is modelled dynamically using a 0-D approach and verified individually by using the software Cycle-Tempo. Then, the BoP models are integrated with an existing 1-D SOFC stack model. A dedicated control system is implemented and the load following capabilities of the complete system are studied.

The model developed is able to simulate the time variation of all the BoP component characteristics and provides insights in the system efficiency when varying operating parameters such as stack current, anode recirculating ratio and fuel utilization. In particular, it is proven that working at low current enables higher cell voltage and, thus, higher system and stack efficiency.

System fuel utilization significantly contributes to the system efficiency, which reaches the highest value for the highest fuel utilization. Additionally, the effect of the fuel utilization rate on the stack and system is the highest at lower currents. System and stack efficiency of respectively 58 % and 66 % are possible with the chosen system configuration. Anode recirculating contributes more to the system efficiency than the stack efficiency. The highest system efficiency is obtained for low current values and high recirculating ratio. Moreover, significant CO_2 emission reduction is obtained for high recirculating ratio.

The chosen control strategy succeeds on ensuring thermal safe operation, but does not guarantee fast response to load changes. In particular, a system response within 2 hours is achieved with the controller developed when the stack current is changed from 27 A to 23 A . Moreover, a load ramp of the stack current is a better choice in terms of thermal safe operation than a stepped change.

The developed model represents a solid base for future development and research in the modelling of SOFC power generation systems for maritime applications. Nevertheless, future investigations on model validation, control system, start-up operations and system optimization are recommended.

Contents

Nomenclature

Acronyms

LH_2	liquefied hydrogen
NO_x	nitrogen oxides
SO_x	sulphur oxides
0-D	zero dimensional
1-D	one dimensional
2-D	two dimensional
3-D	three dimensional
AC	alternating current
AGR	anode gas recirculation
BoP	balance of plant
CPOX	catalytic partial oxidation
DAE	differential algebraic equations
DC	direct current
EMF	electromotive force
FC	fuel cell
GHG	greenhouse gas
HDS	hydrodesulphurisation
HEX	heat exchanger
HFO	heavy fuel oil
HT	high temperature
IMO	International Maritime Organization
ISM	integrated stack module
LHV	lower heating value
LMTD	logarithmic mean temperature difference
LNG	liquefied natural gas

LT	low temperature
MSR	methane steam reforming
MT	medium temperature
NASA	National Aeronautics and Space Administration
NIST	National Institute of Standards and Technology
ODEs	ordinary differential equations
PEMFC	polymer electrolyte membrane fuel cell
PEN	positive electrode-electrolyte-negative electrode assembly
PID	proportional integral derivative
PM	particulate matter
RR	recirculating ratio
SOFC	solid oxide fuel cell
SR	steam reforming
WGS	water gas shift

Greek Symbols

β	compression ratio [-]
ε	porosity [-]
η	efficiency [-] or [%]
$\varkappa$	ratio of specific heats [-]
λ	thermal conductivity [W/m K]
ρ	density [kg/m^3]
σ_e	exit passage contraction ratio [-]
σ_i	entrance passage contraction ratio [-]
σ_{an}	anode electrical conductivity [1/Ωm]
σ_{ca}	cathode electrical conductivity [1/Ωm]
σ_{el}	electrolyte electrical conductivity [1/Ωm]
τ	thickness [mm]

Roman Symbols

$\bar{r}$	mean pore radius [m]
ΔH	enthalpy change [J/mol]
Δp_c	core pressure loss [Pa]
Δp_e	exit pressure loss [Pa]

Δp_i	entrance pressure loss [Pa]
$\dot{C}$	heat capacity rate [W/K]
$\dot{m}$	mass flow [kg/s]
A	area [m^2]
C	heat capacity [J/K]
c_p	specific heat capacity at constant pressure [J/kg K]
f	fraction [-]
G	Gibbs free energy [J]
G^*	Gibbs free energy of formation [J]
H	Gibbs free energy [J]
I_{stack}	stack current [A]
j	current density [A/m^2]
k	reactor catalyst heat capacity [J/K]
K_c	contraction loss coefficient [-]
K_d	derivative gain [-]
K_e	expansion loss coefficient [-]
K_i	integral gain [-]
K_p	proportional gain [-]
N	molar flow [mol/s]
O/C	oxygen to carbon ratio [-]
P	power [W]
R	universal gas constant [J/mol K]
r	reaction rate [mol/s]
Re	Reynolds number [-]
T	Temperature [K]
U	overall heat transfer coefficient [W/m^2K]
$U_{f,g,stack}$	stack global fuel utilization [-]
$U_{f,sp,stack}$	stack single pass fuel utilization [-]
$U_{f,sys}$	system fuel utilization [-]
U_{ox}	oxygen utilization [-]
U_{stack}	stack voltage [V]
V	volume [m^3]

Superscripts

0	standard conditions

Subscripts

an	anode
BL	blower
c	cold
ca	cathode
cf	cold fluid
ch	channel
el	electrolyte
f	formation
h	hot
hf	hot fluid
IC	interconnect
ins	insulation
is	isentropic
j	species
m	mechanical
sys	system
tpb	triple phase bound
W	wall

List of Figures

List of Tables

Chapter 1

Introduction

1.1 Background

International shipping significantly contributes to CO_2 emissions. In 2017, shipping accounted for almost 2.6% of annual global CO_2 emissions [2]. The *Third IMO Greenhouse Gas (GHG) Study* from October 2014 forecast that GHG emissions from international shipping might grow up to 250 % by 2050 [1]. This is mainly related to the expected increase of the shipping volume and the size of the maritime fleet [3, 4]. Consequently, in April 2018, the International Maritime Organisation decreed that the industry must reduce the total annual GHG emissions to 50% of the 2008 level by 2050 [5]. Amongst the different alternatives which could allow shipping industry to meet the 2050 target, developing (near) zero-emission propulsion systems represents the most promising option.

According a DNV-GL report of July 2019 [7], over the past 10 years, the number of all-electric or hybrid ships has grown from zero to more than 350 units in operation and on order. However, the majority of these vessels operates in the short-sea segment for offshore and/or passenger ships/ferries. In other words, none of the current hybrid vessels are deep-sea trading vessels and this is mainly caused by the large energy requirements of these vessels.

Fuel cells have proven to be a reliable technology to produce clean energy from hydrogen. In a fuel cell, electrical energy is produced through conversion of chemical energy of molecules, commonly hydrogen (i.e. H_2). Used as energy source for fuel cells, hydrogen represents the best solution for zero emission deep-sea shipping, having a gravimetric energy density of almost 120 MJ/kg (circa three times higher than diesel). However, as shown in Figure 1.1, when taking into account the required storage system, the situation changes completely and the gravimetric energy density reduces by 90% for liquid hydrogen (LH_2) and comparable value for compressed hydrogen.

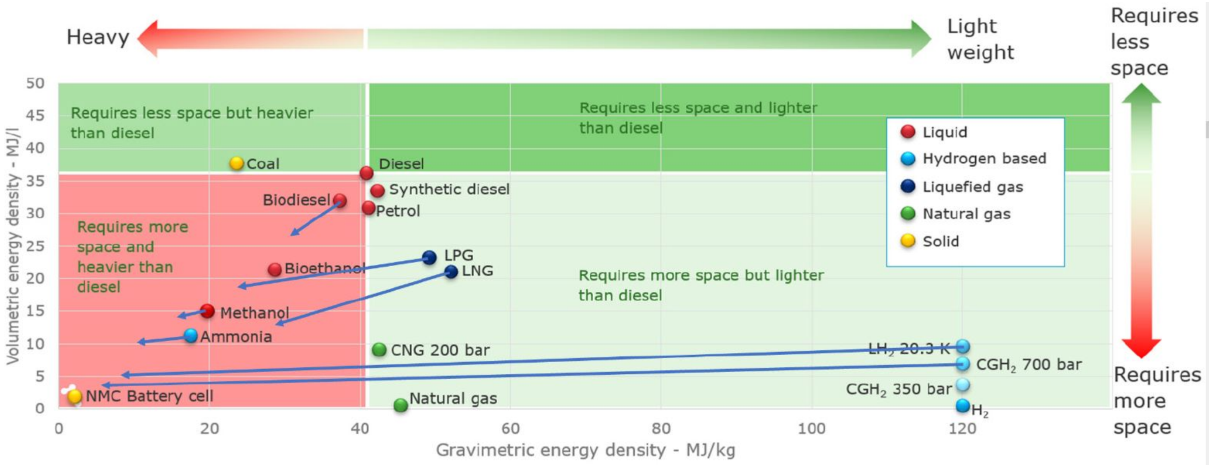

Figure 1.1: Comparison of energy density for different energy carriers. The arrows represent indicative values of the energy density reduction when storage systems are taken into account [7].

Consequently, most of fuel cell systems use a hydrogen carrier, such as methane (CH_4) representing the main component of natural gas. The latter is characterised by lower gravimetric energy density compared to pure hydrogen but higher volumetric and gravimetric energy density when its liquid form (LNG) is compared with LH_2. Moreover, when storage requirements are taken into account, the reduction of energy density is much lower for LNG than for LH_2. The uptake of LNG in the maritime sector has a significant effect on the global fleet growth. The United Nations *Review of Maritime Transport 2019*, reported a gas carriers growth of 7.25% with expected further expansion in view of the pressure on the maritime sector to switch to cleaner fuels [8].

Ammonia (NH_3) and Methanol (CH_3OH) represent alternative hydrogen carriers which might be used in the future in FC systems. Despite the lower gravimetric energy density, the technological maturity level of NH_3 and CH_3OH fuelled FC systems is equivalent to LNG's [7]. Figure 1.2 shows that the combustion of LNG results in less harmful emissions such as nitrogen oxides (NOx), sulphur oxides (SOx) and particulate matter (PM) compared to heavy fuel oil (HFO) and ammonia and similar to methanol.

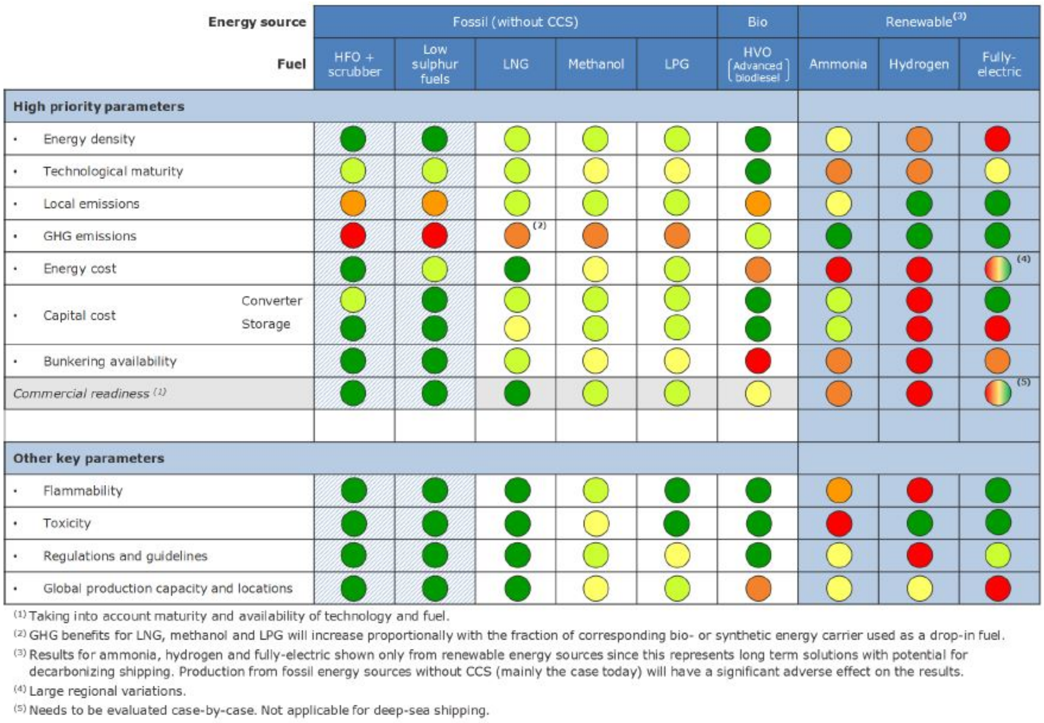

Energy source	Fossil (without CCS)					Bio	Renewable[3]		
Fuel	HFO + scrubber	Low sulphur fuels	LNG	Methanol	LPG	HVO (Advanced biodiesel)	Ammonia	Hydrogen	Fully-electric
High priority parameters									
• Energy density	🟢	🟢	🟩	🟩	🟩	🟢	🟡	🟠	🔴
• Technological maturity	🟩	🟩	🟩	🟡	🟡	🟢	🟠	🟠	🟡
• Local emissions	🟠	🟠	🟩	🟩	🟩	🟠	🟡	🟢	🟢
• GHG emissions	🔴	🔴	🟠 [2]	🟠	🟠	🟩	🟢	🟢	🟢
• Energy cost	🟢	🟩	🟢	🟡	🟩	🟠	🔴	🔴	◐ [4]
• Capital cost — Converter	🟩	🟢	🟩	🟩	🟩	🟢	🟩	🔴	🟢
Storage	🟢	🟢	🟡	🟩	🟩	🟢	🟩	🔴	🔴
• Bunkering availability	🟢	🟢	🟩	🟡	🟡	🔴	🟠	🔴	🟠
Commercial readiness [1]	🟢	🟢	🟢	🟩	🟩	🟡	🟠	🔴	◐ [5]
Other key parameters									
• Flammability	🟢	🟢	🟢	🟩	🟢	🟢	🟠	🔴	🟢
• Toxicity	🟢	🟢	🟢	🟡	🟢	🟢	🔴	🟢	🟢
• Regulations and guidelines	🟢	🟢	🟢	🟩	🟡	🟢	🟡	🔴	🟩
• Global production capacity and locations	🟢	🟢	🟢	🟡	🟩	🟠	🟡	🟡	🔴

(1) Taking into account maturity and availability of technology and fuel.
(2) GHG benefits for LNG, methanol and LPG will increase proportionally with the fraction of corresponding bio- or synthetic energy carrier used as a drop-in fuel.
(3) Results for ammonia, hydrogen and fully-electric shown only from renewable energy sources since this represents long term solutions with potential for decarbonizing shipping. Production from fossil energy sources without CCS (mainly the case today) will have a significant adverse effect on the results.
(4) Large regional variations.
(5) Needs to be evaluated case-by-case. Not applicable for deep-sea shipping.

Figure 1.2: DNV-GL's interpretation of results obtained by comparison of alternative fuels. [7].

However, when fuel availability is taken into account, only LNG is able to cover the current energy requirements of the shipping industry with developed bunkering infrastructures in Norway, North West Europe and the Baltic Sea. According to DNV-GL, it would be theoretically possible for the global fleet to switch to LNG considering the current LNG production and the shipping industry current energy requirements [6,7]. An additional upside for LNG is found in the possibility of using its main component, CH_4, directly as fuel for fuel cells which do not require a high level of fuel purity. High temperature Solid Oxide Fuel Cell (SOFC) are the best match for methane fuelled FCs, due to the ability of nickel (used as anode material in SOFCs) to reform hydrocarbons directly on the FC anode and to the capability of SOFC to use CO internally through the 'water-gas shift (WGS)' reaction [12]. Extensive range of applicability, construction material availability and relatively high power density, place this type of fuel cells among the most studied nowadays [13,51].

The performance of a FC power generation system does not depend solely on the FC stack, but also on the components around the stack known as the Balance of Plant (BoP). Most of these components, require electric power which is drawn from the stack, causing parasitic losses, reducing the system efficiency.

1.2 Research Objective and Scope

Modelling and simulating represent the main tools used in System Engineering [46]. Particularly, being able to study the possible modification of an existing systems without running in the higher cost and time requirements of an actual modification, is the key point of modelling.

Extensive studies have been conducted over the past years on modelling and simulating the performance of single or multiple cell SOFC systems ([18–21, 23–36, 41–45]). However, relatively few research has been done on how the performance and the dynamics of the BoP components influence the performance of an SOFC power generation system, especially during load transients and start-up operations ([37, 39, 40, 45]). Moreover, due to the large amount of possible SOFC system configurations and supplier confidentiality on available system-level data, only few modelling studies have been validated ([30, 38]).

The overall objective of this research can be summarised as follow:

Gain insight on the performance of the BoP components and their influence on the SOFC power generation system for maritime applications.

The objective of this study translates in the following main research question:

”How do the BoP components affect the SOFC system efficiency and load following capabilities ?”

To be able to answer the main research question, the following sub-questions must be answered:

- *Which components affect the SOFC system performance the most during the specified operations?*
- *What is the effect of these components on the SOFC system efficiency and load following capabilities?*
- *Which control strategy can ensure a relatively fast system response?*

The research will be conducted according to the following research methodology:

- *Develop a dynamic model of the BoP components*
- *Integrate the developed BoP model with an existing 1-D SOFC dynamic model* [21]
- *Study the load following capabilities of the modelled system*
- *Develop a dedicated system control strategy*

1.3 Thesis Outline

In this research, a model predicting the performance of a complete SOFC system for maritime application is developed. Chapter 2 reports a brief recap of the modelling strategies used in literature for SOFC systems. The complete literature study can be found in [9]. In Chapter 3, the proposed system configuration and the chosen modelling approach and assumptions are described. The characteristics of each system component as well as the equations implemented in the model and describing the physical phenomena, are reported and explained in Chapter 4. Chapter 5 shortly describes the characteristics and the modelling methodology used for the SOFC stack developed model by Biert et al. [21]. The adopted control strategy for the studied SOFC system configuration is described in Chapter 6. Then, Chapter 7, 8 and 9 report respectively the model verification and the discussion of the obtained results. Finally, the conclusions and recommendations are presented in Chapter 10.

Chapter 2

Literature Review

The main objective of mathematical modelling is predicting the performance and behaviour of a system or component to provide answers and understanding. Over the last two decades, several models have been developed to predict the performance and behaviour of SOFC systems. Either by analysing only the time evolution of the system itself, referred to as 0-D dynamic models, or by estimating both time and space variation of the system characteristics, thus 1,2 or 3-D dynamic models. This chapter reports an overview of the different strategies adopted in literature and the respective challenges. A more detailed explanation of the working principles of fuel cells and fuel cell systems can be found in the conducted literature study [9].

2.1 0-D Dynamic Models

Zero-dimensional dynamic models are suitable for systems whose main characteristics and performance are known[15]. These models are characterised by a set of mathematical equations, commonly ordinary differential equations (ODEs) or differential algebraic equations (DAE). These equations are based on the conservation of mass and energy, thus able to describe the time evolution of the system. Despite the lower level of accuracy compared to 1-D models, zero dimensional modelling represents the simplest approach for fuel cell systems. It is important to note that 0-D SOFC models should be used for those studies where the focus is not on the SOFC itself, but on its effect on the system performance [66].

Lu et al. [35] demonstrated that developing a Simulink lumped dynamic model for an SOFC auxiliary power unit represents a perfect compromise between reasonably good accuracy and low computational time. However, in the presented SOFC plant model, only few of the BoP components generally used in an SOFC system were considered. Specifically only the heat exchangers and the post-combustor have been modelled. The results showed that thermal dynamics did not in general affect the electric dynamic responses.

Murshed et al. [25] demonstrated the influence of heat exchangers, afterburner and steam reformer on an SOFC system fed by methane, by developing two models characterised by 0-D non linear ODEs. In particular, it has been shown how the effect of flow rates or disturbances propagates through the entire SOFC system. Specifically, a change in fuel flow rate or inlet temperature leads to a change in hydrogen flow rate in the fuel cell from the reformer, thus changing the fuel cell temperature and stack voltage. The unreacted fuel then moves to after-burner and heat exchangers which again affects the temperatures of the reformer and fuel cell.

With a system configuration similar to Murshed et al. [25], Sorrentino and Pianese [31] used a grey-box approach to dynamically model the performance of a planar co-flow SOFC system fed by methane. The model describes the response of fuel cell and heat exchangers to load change. In particular, it is demonstrated how a step variation in power demand produces a significantly high overshoot in stack temperature difference (ΔT) possibly causing damaging thermal stresses to the system. Therefore it has been necessary to introduce a power rate limiter to limit the ΔT variations within a safe bound.

Barelli et al. [26] conducted a dynamic analysis on an SOFC-based Combined Heat Power (CHP) system characterised by a fuel pre-treatment section (i.e. reformer, burner and steam generator), a mixer and two heat exchangers. Attention was paid on sizing the two heat exchangers properly. The 0-D developed model was able to simulate the response of the system to an electric power step of 800 W (to reach the nominal 3 kWe). The results showed how the large inertia of the steam generator causes an overshoot of the SOFC potential, thus influencing the SOFC stack and system behaviour.

Sorce et al. [30] developed a 0-D dynamic model of an SOFC system by coupling the model of the three main components, i.e. SOFC stack, external pre-reformer and afterburner. The model described with good accuracy the manufactured system used for the validation. Attention was also paid on the effect of different faults on the system performance. In particular, it has been demonstrated how SOFC degradation and fuel leakage cause a decrease of the gas discharge temperature, while the opposite occurs for reformer degradation.

Lisbona et al. [66] modelled a planar anode supported SOFC system including desulphuriser, pre-reformer, after-burner and heat management system. The results showed how by enhancing the degree of pre-reforming, the power production increases and so does the electrical efficiency. The effect of anode recirculation was also studied. In particular, it was shown an electrical efficiency increase up to 51% and a overall efficiency up to 75%.

Omosun et al.[67] developed a steady state model for a 200 kWe SOFC CHP system. It has been demonstrated how the main BoP components responsible for stack cooling, i.e. air blower, significantly affects the efficiency of the system with a power requirement up to 60% the total power demand. Consequently, the use of more efficient cooling methods for the SOFC could have a significant beneficial impact on the total system efficiency.

Kazempoor et al. [68] developed and integrated the models of all the BoP components (e.g. compressor, pre-heaters, burner and air blower) with an SOFC model and studied the effect on system design and efficiency of feeding the system first with methane and then directly with hydrogen. The results showed that a higher electrical efficiency is obtained when the system is fed with methane. Moreover, for both fuel cases, the implementation of cathode gas recycling to the base cases effectively improved the electric efficiencies by 7% and 12% for hydrogen fuelled and methane fuelled respectively.

2.2 1-D Dynamic Models

The main objective of 1-D FC dynamic model is to predict thermodynamic and material properties variations along only one of the three dimensions of the studied system. SOFC systems are characterised by high operating temperatures and consequently being able to identify the temperature levels and temperature gradient variations inside the SOFC stack is extremely helpful to prevent degradation and system failure. Most of the 1-D models found in literature are restricted solely to the SOFC stack thus not including any BoP components.

Cheddie et al. [42] developed a 1-D dynamic model in which a system of differential equations has been derived by applying mass and energy conservation principles over 1-D control volumes of an SOFC stack. The study resulted in a relatively fast and accurate model. In particular, it was proven that the pumping power required to supply air and fuel to the cell was in the same order of magnitude as the power produced by the fuel cell. It was possible to reduce the pressure drop due to wall friction, and hence the required pumping power, by reducing the amount of channels with larger cross-sectional areas.

Sorrentino et al. [43] proposed a hierarchical modelling approach to provide (accurate) estimates of the spatial variation of the main SOFC operating variables by using results generated via 1-D model of single cell operation. Particular attention was paid on proper controlling the voltage and temperature responses to changes in current load. The PI controller was able to reduce the voltage relaxation time and ensure that the temperature rise subsequent to the load step did not exceed a safe range.

Huangfu et al. [73] developed a 1-D multiphysical SOFC dynamic model to predict the non-uniform distributions of current density, gas pressure and temperature in SOFC during its operation. In particular, transients of the model have been studied through a step current change of 0 A to 3.5 A. Results showed that the anode activation voltage transient time is smaller with a higher H_2 partial pressure .

Kang et al. [44] decided to use two simplification strategies to develop a reduced 1-D dynamic model able to predict the performance of a co-flow planar anode-supported SOFC. It was proven that reduced computational time can be achieved if the SOFC is considered to have only one temperature layer and the current distribution is uniform within the stack. The accuracy of the model was not compromised by these two simplifications.

2.3 2-D and 3-D Dynamic Models

Two and three dimensional models are used mainly for phenomena investigation and rarely for performance investigation and control purposes [15]. Moreover, only the SOFC stack is modelled with a 2-D or 3-D approach, while the BoP components reach at maximum a level of accuracy as for 1-D approach. Using a 2-D or 3-D approach also for the BoP components might be unnecessary and extremely time consuming from a computational point of view, specifically for those components which do not require such a level of detail (e.g. blowers, fans, heat exchangers). 2-D models for fuel cells usually derives from the simplification that the changes that occur in the gas flow direction and in the direction normal to the gas flow are much larger than the changes in the third direction (i.e. transverse direction normal to the gas flow). Therefore, the governing equations significantly simplify. 3-D models are generally very computationally expensive due to the non linear and highly coupled mathematical formulation. Example of these approaches can be found in literature [69–72].

2.4 Integration of BoP and SOFC stack Models

The researches reported in section 2.2 represent a small part of the several researches available in literature. It is interesting to note how in all the presented researches, none of the BoP components of the SOFC system were taken in consideration. Integration of the 1-D fuel cell model in a complete SOFC system is usually done by modelling the BoP components using a 0-D approach as shown by Zhang et al. research [45] who developed a hybrid 0-D/1-D dynamic model of a 5 kW hydrogen fuelled SOFC system. The proposed system configuration is characterized by two heat exchangers, an afterburner and a electronic control unit. The main reason of modelling the BoP components by using a 0-D approach is the reduction of computational time. It is assumed that the system is fed directly with H_2, therefore no fuel processing is considered (e.g. pre-reformer, desulphuriser). The results showed how the SOFC system achieved maximum efficiency while ensuring thermal safety by using properly a step power-switching scheme.

A similar approach was used by Andersson et al. [37] where the 1-D SOFC model has been integrated with some of the BoP components. In particular, an autothermal reformer (ATR), a steam generator and a catalytic burner have been modelled using a 0-D approach, while the stack cells were discretized with four elements along the fuel flow direction. The modelling strategy succeeded to give a good compromise between accuracy and computation time.

Farhad et al. [39] studied the effect of three different bio-gas processing systems on the anode carbon deposition. Anode gas recirculation, steam reforming and partial oxidation have been developed in this model. Moreover, the BoP components of the studied SOFC system have been modelled thermodynamically under steady state operating conditions. Two different reforming processes, i.e. steam reforming and partial oxidation, have been modelled. Results showed that the three biogas-fuelled SOFC systems studied were able to generate electric power with an AC electrical efficiency of 42.4%, 41.7% and 33.9% respectively.

Hotz et al. [40] extended an existing 1-D model of an SOFC to a 2-D model considering convective mass and heat transport along the fuel cell channel and from it to the surroundings. The BoP components involved (i.e. POX reformer, post-combustor, vaporiser and two pre-heaters) have been modelled as control volumes. The results of this study showed that the fuel cell performance can be easily increased by adjusting the operating parameters. In particular, the power can be enhanced by slightly changing the cell voltage and the air/fuel ratio. Moreover, it has been demonstrated how the exergetic efficiency of the system can be increased significantly by choosing the operating conditions properly.

2.5 Literature Study Conclusion

The aim of this literature review was to understand how the presented research objectives can be achieved by properly observing the results accomplished and the methodology used in previous relevant studies. The pressure on the maritime sector to find alternative solutions to be able to meet the IMO 2050 target has led to a growth in research aimed at using fuel cell as zero-carbon propulsion systems. Nowadays, fuel cells are used mainly as auxiliary power unit to supply up to 350 kW of electrical energy and their development as propulsion system is narrowed to small size vessels. The limited understanding of the influence of the BoP components in a FC system represents, among others, the cause of this slow development.

Therefore, to achieve the objective of gaining insight of the influence of the BoP on the dynamic behaviour of an SOFC, a dynamic model of the BoP will be developed. The BoP model will be integrated with the 1-D SOFC dynamic developed model by van Biert et al. [21] and dedicated control strategies will be evaluated. Attention will be paid specifically on load transients and how the BoP components affect the system during these operations.

Chapter 3

Methodology

The main objective of this research consists of gaining insights of the performance of the BoP components and their influence on the SOFC power generation system for maritime applications. Therefore, a mathematical 0-D dynamic model of the BoP components is developed and integrated with an existing 1-D dynamic model of an SOFC stack . The chosen system configuration, the model approach and the adopted control strategies are justified and described in detail in this chapter.

3.1 System Configuration

Based on the conclusion obtained from the literature review [9] and considering the current state of technology, a specific system configuration is chosen and it is shown in Figure 3.1.

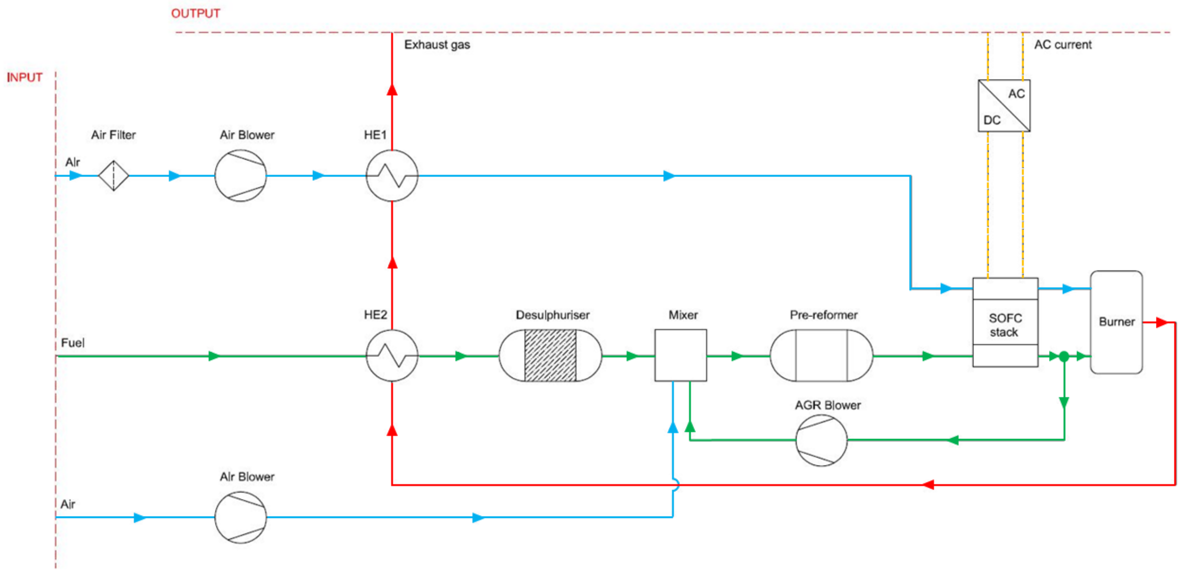

Figure 3.1: Overview of the methane fuelled SOFC system proposed in this research.

The system is characterized by 3 input lines (i.e. air stream, fuel stream and supply air stream) and 2 output lines (i.e. exhaust gas stream and DC current). Air is drawn at ambient condition, filtered and fed in to the system by using a dedicated air blower. The air is pre-heated to reach the stack operating temperature by using a single pass counter flow heat exchanger (HE1), before entering the cathode side of the SOFC stack. The air composition on a molar basis is assumed to be 21% of O_2 and 79% of N_2.

The system is fuelled with LNG which enters the system in the gas phase at ambient condition (the fuel handling system is not considered in this research). Like the air, also the fuel is pre-heated using a single pass counter flow heat exchanger (HE2), mainly to facilitate the process of desulphurisation taking place in the desulphuriser. A LNG composition of 100% CH_4 is assumed. The fuel is then mixed with the supply air and the anode exhaust gas coming from the Anode Gas Recirculating (AGR) blower before entering the external pre-reformer. The latter is used to partially reform the fuel through a chemical process which produces a hydrogen rich mixture (i.e. syngas). In particular, catalytic partial oxidation (CPOX) is used in this system as reforming process to convert methane into hydrogen , i.e. H_2, which is then used in the fuel cell stack to produce electricity. The supply air is mixed with the fuel stream line and the AGR line before entering the chemical reactor, using a dedicated air blower.

The amount of supply air provided for the reforming process is determined by the O/C ratio, which is kept constant mainly to avoid carbon deposition, and consequently by the amount of syngas recirculated in the system (depending on the AGR blower anode recirculating ratio). The CPOX air ensures that partial oxidation of CH_4 takes place so that the pre-reformer outlet gas composition is characterized not only by the presence of CO_2 and H_2O, but also H_2 and CO. It is important to specify that N_2 does not react in any of the reaction above mentioned and complete O_2 consumption is assumed.

Air and fuel enter the SOFC stack unit, consisting of an integrated stack module (ISM) containing two 30 cells stack towers connected in series producing up to 1 kW power [21]. Here, fuel and oxidant react producing power and heat. Part of the exhausts of the SOFC stack are then mixed and burned in a combustor. The high temperature exhaust gasses exiting the burner are then used to pre-heat first fuel and then air to the respective operating temperature. This process increases the system efficiency and prevents CO emissions. The chemical process happening in the SOFC stack produces DC electricity. Since most of the stationary applications (e.g. electric AC motors) require AC power, DC/AC converters are used to produce alternating current.

3.2 Control Strategies

While developing the dedicated control strategies, attention will be paid mainly to the load-following capabilities of the system as well as the stack temperature. It is extremely important to avoid large temperature gradients in the stack, which affect the interconnect and the cell properties causing cell degradation and reduction of system performance. Moreover, stack overheating is responsible of voltage drops and speeds-up the cell degradation mechanism [52].

Two main control systems are developed for the proposed SOFC system. First, feedback control logic is applied to the cathode air blower, by means of a proportional–integral-derivative (PID) controller (see Figure 3.2), developed in such a way so to feed the excess air required to meet the desired temperature value of the PEN assembly (T_{TARGET}). Then, a feed-forward control is used to estimate the new required current related to the new power demand during load transients, by means of a look-up table. The effect of stepping and ramping the current will be evaluated. It is important to specify, that by changing the current, the amount of fuel fed to the system changes so to keep the system fuel utilization constant and equal to the nominal value, according to relation (8.1).

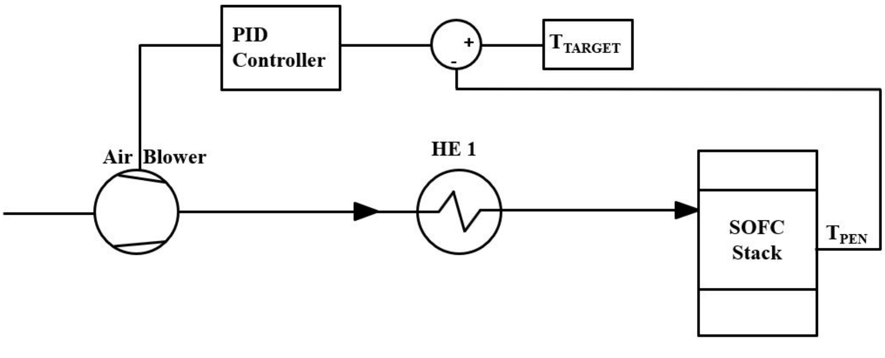

Figure 3.2: Overview of the implemented feed-back loop.

3.3 Modelling Approach and Assumptions

It has been decided to use a 0-D modular causal approach, to be able to simulate the performance of the BoP components around the SOFC stack with good accuracy and relatively fast computations. Particularly, each component will be divided into computational block diagram structures with predefined causalities. Each module will either be a resistive or a storage module (see Figure 3.3) depending on if algebraic or dynamic conservation equations are used respectively [17]. In particular, in a resistive module, a mass flow is estimated by using the pressure difference over the element as input while the the pressure is estimated on the mass flow difference in the storage module.

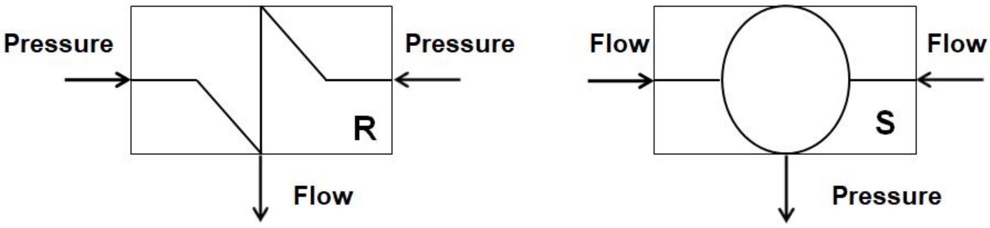

Figure 3.3: Modularity approach modules. Resistive module (left) and storage module (right).

Consequently, the outputs of each module are computed as function of the inputs according to the modularity principle described by Colonna et al. [17]. Moreover, due to their inverse causalities, a resistive and a storage module must be connected in series.

The SOFC stack model used for the chosen system configuration, was first developed by Azzopardi [22] and was later extended and improved upon by Biert et al. [21]. The model is dynamic, thus accounting for time variations of the input conditions and 1 dimensional. In particular, air, fuel, interconnect and positive electrode-electrolyte-negative electrode (PEN) assembly are discretised in the flow direction by using separate control volumes. Additionally, the model accounts for the stack active area, heat transfer in the inactive sections and surrounding heat losses [21].

The BoP model is developed under the following assumptions:

- The air composition is assumed to be 21% of O_2 and 79% of N_2 (on a molar basis);
- The LNG composition is assumed to be 100% of CH_4 (on a molar basis);
- All the gasses are assumed to obey the ideal gas law;
- Heat losses from the two heat exchangers, the CPOX reformer, the mixer and the afterburner are neglected, thus the processes are assumed to be adiabatic;
- The temperature change within the hot and cold fluid channels in the heat exchangers is assumed to be linear
- Pressure losses in the CPOX reformer, mixer and afterburner are neglected;
- The fuel handling system is not modelled in this research;
- Complete O_2 combustion is assumed in both pre-reformer and afterburner;
- N_2 does not react in any of the pre-reformer and afterburner reaction;
- Power estimations refer to the stack operations;

The assumptions of the 1-D SOFC stack model can be found in [21].

Chapter 4

Balance of Plant Component Models

The performance of the BoP is simulated by developing a dynamic 0-D Matlab Simulink model. The characteristics of each system component as well as the equations implemented in the model and describing the physical phenomena, are reported and explained in this chapter.

4.1 Blower

In a Fuel Cell system, blowers represent ancillaries power devices used to supply the right amount of air and fuel so to guarantee the correct functioning of the system. These devices require electrical power, which is usually drawn from the stack causing parasitic losses [51].

The SOFC system studied is equipped with three blowers (see figure 3.1): the cathode air blower, the CPOX air blower and the AGR blower.

In particular, the cathode air blower plays an important role in the SOFC system since it is responsible for supplying the right amount of oxidant at the SOFC cathode inlet so to ensure that the electrochemical reactions take place properly. Moreover, the air provided by the blower is used to cool down the SOFC stack in order to ensure that the specific temperature ranges are not exceeded and consequently the cell performance and lifetime are not diminished.

The CPOX air blower is used to provide the right amount of O_2 necessary for the external CPOX reforming process, which takes place in the pre-reformer. The amount of CPOX air needed is related to the O/C ratio, the anode recirculating ratio and the system fuel utilization $U_{f,sys}$. It is important to note that, during nominal operations, the CPOX blower might be turned off, since enough oxygen is provided from the AGR blower.

Finally, the AGR blower is responsible of recirculating part of the exhaust anode syngas back to the fuel pre-reformer, according to the chosen RR. It is important to specify that, both the CPOX and AGR blower play an important role in the load-following capabilities of the entire system.

4.1.1 Blower Model

Since the blower represents the main device causing parasitic losses, its power estimation is necessary for the complete system performance prediction [15]. Despite the difference in the flow composition (i.e. air or syngas), all three blowers in the FC system are modelled using the same approach. The power needed to drive the blower is evaluated as function of isentropic and mechanical efficiency, ideal compression work and knowledge of the heat capacity of the gas.

$$P_{BL} = \dot{m} \cdot \frac{c_p \cdot T}{\eta_{is} \cdot \eta_m} \cdot \left[\beta^{\frac{k-1}{k}} - 1 \right] \tag{4.1}$$

Where $\dot{m}$ represents the inlet mass flow (kg s^{-1}), η_{is} and η_m the blower isentropic and mechanical efficiency respectively, β the compression ratio ($p_{out/p_{in}}$) and c_p the specific heat capacity at constant pressure (J kg^{-1} K^{-1}). The values of η_{is} and η_m have been chosen according to literature [15].

Table 4.1: Parameters of the blowers used in the SOFC system

Parameter	**Symbol**	**Unit**	**Value**
Compression ratio	β	[-]	1.3
Isentropic efficiency	η_{is}	[-]	0.7
Mechanical efficiency	η_m	[-]	0.8

The heat capacity of the gases is calculated according to the Shomate equation with coefficients provided by the National Institute of Standards and Technology Chemistry WebBook [47,48].

4.2 Heat Exchanger

Thermal management represents a critical aspect for an SOFC system of which the performance is highly affected by stack voltage drops and degradation mechanism enhancement caused by stack overheating [51,52]. The high temperature operating conditions require both the cathode and the anode inlet gases to be heated to the working temperature before feeding the stack. In an SOFC system, this is usually done through heat exchangers, where the cathode and anode inlet flows are heated with the heat carried by the afterburner exhaust gases.

The proposed system configuration is characterised by two single-pass counter-flow tubular heat exchangers, one for the cathode flow, HE1, and one for the anode, HE2 (see Fig. 3.1). It is important to note that, unlike HE1, HE2 is not located before the SOFC stack but before the desulphuriser and consequently the pre-reformer because the heat is required for both processes

Sulphur compounds contained in the fuel must be removed to avoid deactivation of the catalyst used in the reformer and in the fuel cell. This process can be done effectively at elevated temperatures (300° C - 400° C) through hydrodesulphurisation (HDS) [53–55].

Together with the O/C ratio, the pre-heating temperature of the gas mixture entering the reactor, represents an important parameter that strongly affects the CPOX reaction, increasing the CH_4 conversion as well as the reactor temperature [60, 61]. In most SOFC applications, pre-heating temperatures up to 400° C are reached [56].

4.2.1 Heat Exchanger Model

The dynamic performance of the counter-flow heat exchangers have been estimated following the approach proposed by Ataer at al. [62]. This approach allows to estimate (with low computation effort) the response of the heat exchanger to variation in hot and cold fluid temperatures as well as flow. The dynamics of hot and cold fluid are modelled under the assumptions that there are no heat losses from the heat exchanger to the environment, the temperature changes linearly within hot and cold channels and the gases are assumed to obey to the ideal gas law:

$$(\mathrm{C_h} + \mathrm{C_m}) \cdot \frac{\mathrm{dT_h}}{\mathrm{dt}} = \dot{\mathrm{C}}_\mathrm{h} \cdot (\mathrm{T_{h,in}} - \mathrm{T_{h,out}}) - \mathrm{U} \cdot \mathrm{A} \cdot \mathrm{LMTD} \tag{4.2}$$

$$(\mathrm{C_c}) \cdot \frac{\mathrm{dT_c}}{\mathrm{dt}} = \dot{\mathrm{C}}_\mathrm{c} \cdot (\mathrm{T_{c,in}} - \mathrm{T_{c,out}}) - \mathrm{U} \cdot \mathrm{A} \cdot \mathrm{LMTD} \tag{4.3}$$

With the logarithmic mean temperature difference (LMTD) expressed as follow:

$$\mathrm{LMTD} = \frac{\Delta \mathrm{T_0} - \Delta \mathrm{T_1}}{\ln \frac{\Delta \mathrm{T_0}}{\Delta \mathrm{T_1}}} \qquad \text{Where} \quad \Delta \mathrm{T_0} = \mathrm{T_{h,out}} - \mathrm{T_{c,in}} \qquad \Delta \mathrm{T_1} = \mathrm{T_{h,in}} - \mathrm{T_{c,out}} \tag{4.4}$$

In eq. (4.2) and (4.3), U represents the overall heat transfer coefficient (W/m^2 K) and C_h and C_c respectively the heat capacity of hot and cold fluid (J/K). The heat capacity of the wall C_m (J/K) is added to the capacity of the hot fluid as proposed by Ataer et al. [62]. Finally, the hot and cold fluid heat capacity rate, $\dot{C}_c$ and $\dot{C}_h$ are expressed in (W/K) and estimated considering the fluid mass flow and the specific heat capacity. In particular, the latter is calculated as function of temperature using the Shomate equations [47]. Figure 4.1 shows an example of the cold fluid temperature profile obtained from the air heat exchanger model. The hot fluid inlet temperature is kept constant as well as the hot fluid mass flow.

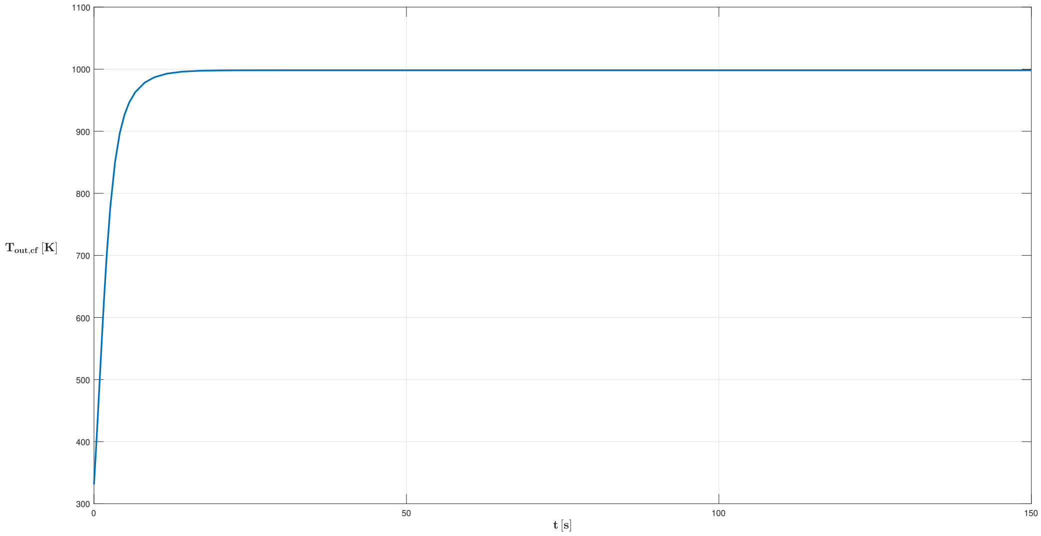

Figure 4.1: Example of temperature profile of the cold fluid exiting the air heat exchanger.

Pressure drop in the heat exchangers is estimated following the procedure proposed by Khayal [63]. The total pressure drop is estimated as sum of three different contributions, namely entrance (Δp_i), exit (Δp_e) and core loss (Δp_c). In particular, entrance and exit losses are caused respectively by a sudden reduction and expansion in flow area and can be evaluated considering Bernoulli's equation. Core losses are caused by friction and other internal losses due to change in flow velocity resulting from temperature variations [63].

$$\Delta p_i = \frac{1}{2} \cdot \left(1 - \sigma_i^2 + K_c\right) \cdot \frac{G^2}{\rho_i} \tag{4.5}$$

$$\Delta p_c = \frac{1}{2} \cdot \frac{G^2}{\rho_m} \cdot \frac{4 f L}{D_h} + G^2 \cdot \left(\frac{1}{\rho_e} - \frac{1}{\rho_i}\right) \tag{4.6}$$

$$\Delta p_e = -\frac{1}{2} \cdot \left(1 - \sigma_e^2 - K_e\right) \cdot \frac{G^2}{\rho_e} \tag{4.7}$$

Where G represents the fluid mass flux $\left(\mathrm{kg}/(\mathrm{s\,m}^2)\right)$, ρ the density $\left(\mathrm{kg}/\mathrm{m}^3\right)$, f the Fanning frictional factor, L and D_h the heat exchanger tubes length and diameter and σ the passage contraction ratio estimated as function of channel radius and HEx volume. Thanks to the relatively small dependency on the Reynolds number, the value of the expansion and contraction loss coefficients K_c and K_e can be determined considering the $Re = \infty$ curves:

$$K_c = 0.42 \cdot (1 - \sigma^2)^2 \tag{4.8}$$

$$K_e = (1 - \sigma)^2 \tag{4.9}$$

The heat exchanger total pressure drop is then estimate as the sum of the three contributions:

$$\Delta p = \frac{G^2}{2\rho_i} \cdot \left[\left(1 - \sigma_i^2 + K_c\right) + f\frac{4L}{D_h} \cdot \left(\frac{\rho_i}{\rho_m}\right) + 2\left(\frac{\rho_i}{\rho_e} - 1\right) - \left(1 - \sigma_e^2 + K_e\right) \cdot \left(\frac{\rho_i}{\rho_e}\right) \right] \tag{4.10}$$

Table 4.2: Characteristics of air (HE1) and fuel (HE2) heat exchangers.

Parameter	**Symbol**	**Unit**	**Value HE1**	**Value HE2**
Overall Heat Transfer Coefficient	U	[W/m^2 K]	20	20
Mean Heat Transfer Area	A_w	[m^2]	5.35e-3	9.74e-5
Total Exchanger Volume	V_{HE}	[m^3]	2.14e-4	3.89e-6
Channel Diameter	D_{ch}	[m]	0.04	0.04
Channel Length	L_{ch}	[m]	0.17	0.0031
Wall Heat Capacity	C_m	[J/K]	0.009	0.009

4.3 Mixer

Before the external reforming process can take place, the fuel exiting the desulphuriser is mixed with the air coming from the CPOX blower and the anode exhaust gases coming from the AGR loop.

4.3.1 Mixer Model

The mixer is modelled as a single control volume and the outlet temperature and flow composition are estimated through mass and energy balance equations considering the process as adiabatic.

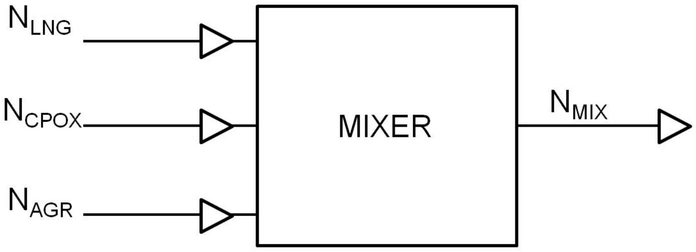

Figure 4.2: Overview of the mixing process. N_{LNG} represents the molar flow of LNG entering the SOFC system. A LNG composition of 100% of CH_4 is assumed.

The mixer outlet temperature is estimated through enthalpy balance on the control volume:

$$\sum_j N_{j,out} \cdot H_{j,out}(T_{out}) = \sum_j N_{j,in} \cdot H_{j,in}(T_{in}) \tag{4.11}$$

$H_{j,in}$ and $H_{j,out}$ correspond respectively to the enthalpy of the species j at T_{in} and T_{out}. The dependency of the enthalpy on the temperature is expressed using the Shomate estimation [47] with coefficients provided by the NIST WebBook [48].

$N_{j,in}$ and $N_{j,out}$ represents the molar flow in and out of the species involved in the mixing process (mol/s). The latter have been estimated considering, for each species, a dynamic mass balance equation in the mixer control volume:

$$
\begin{aligned}
\frac{dN_{CH_4}}{dt} &= N_{CH_4,in} - N_{CH_4,out} = N_{CH_4,LNG} + N_{CH_4,AGR} - N_{CH_4,Mix} \\
\frac{dN_{CO_2}}{dt} &= N_{CO_2,in} - N_{CO_2,out} = N_{CO_2,AGR} - N_{CO_2,Mix} \\
\frac{dN_{CO}}{dt} &= N_{CO,in} - N_{CO,out} = N_{CO,AGR} - N_{CO,Mix} \\
\frac{dN_{H_2}}{dt} &= N_{H_2,in} - N_{H_2,out} = N_{H_2,AGR} - N_{H_2,Mix} \\
\frac{dN_{H_2O}}{dt} &= N_{H_2O,in} - N_{H_2O,out} = N_{H_2O,AGR} - N_{H_2O,Mix} \\
\frac{dN_{N_2}}{dt} &= N_{N_2,in} - N_{N_2,out} = N_{N_2,CPOX} + N_{N_2,AGR} - N_{N_2,Mix} \\
\frac{dN_{O_2}}{dt} &= N_{O_2,in} - N_{O_2,out} = N_{O_2,CPOX} + N_{O_2,AGR} - N_{O_2,Mix}
\end{aligned}
\tag{4.12}
$$

The amount of methane supplied to the system ($N_{CH_4,LNG}$) is estimated as the sum of two contributions: the methane flow that is electrochemically oxides in the fuel cell, $N_{CH_4,SOFC}$ and the methane flow that is oxidised in the CPOX reformer, $N_{CH_4,CPOX}$. The latter is used to estimate the amount of CPOX air (i.e. $N_{O_2,CPOX}$ and $N_{N_2,CPOX}$) needed so that the reforming process can take place.

$N_{CH_4,CPOX}$ is related to $N_{CH_4,SOFC}$ through the following relation:

$$
N_{CH_4,CPOX} = \frac{f_{CH_4,CPOX}}{f_{CH_4,SOFC}} \cdot N_{CH_4,SOFC} = \frac{f_{CH_4,CPOX}}{1 - f_{CH_4,CPOX}} \cdot N_{CH_4,SOFC} \tag{4.13}
$$

Where $f_{CH_4,CPOX}$ and $f_{CH_4,SOFC}$ represent the CPOX reformer and the SOFC fraction of the total fuel supplied to the system. In particular, $f_{CH_4,CPOX}$ is related to the anode recirculating ratio RR, the O/C ratio and the system fuel utilization $U_{f,sys}$ as follow:

$$
f_{CH_4,CPOX} = \frac{\frac{O/C}{4} - U_{f,sys} \cdot RR}{1 - RR \cdot U_{f,sys}} \tag{4.14}
$$

It is important to clarify that, during nominal operations and in steady-state conditions, $f_{CH_4,CPOX}$ is a constant value since system fuel utilization $U_{f,sys}$, O/C ratio and RR are constant values.

The complete derivation of relation (4.13) and (4.14) is reported in Appendix A.

4.4 Pre-Reformer

The studied FC system is equipped with an external reformer represented by a chemical reactor, containing a catalyst. The reformer is used to generate a hydrogen rich mixture through catalytic partial oxidation (CPOX) of methane. Complete oxidation (or combustion) of CH_4 is obtained when the hydrocarbon is combined with the stoichiometric amount of O_2 thus producing CO_2 and H_2O (4.15). However, when CH_4 is combined with less than the stoichiometric amount, a mixture of incomplete combustion products, H_2 and CO, is generated (4.16) [51]. Moreover, for value of O_2/CH_4 between 2 and 0.5, the partial oxidation and the full combustion coexist, producing a mixture of CO, CO_2, H_2 and H_2O [57].

$$
CH_4 + 2\,O_2 \Rightarrow CO_2 + 2\,H_2O \quad \textbf{Complete Combustion} \tag{4.15}
$$

$$
CH_4 + \frac{1}{2}\,O_2 \Rightarrow CO + 2\,H_2 \quad \textbf{Partial Oxidation} \tag{4.16}
$$

Catalytic partial oxidation of methane takes place inside the reactor at temperatures higher than 1073 K where the hydrogen yield is the highest [57]. The hydrogen yield of CPOx is lower than of steam reforming and auto-thermal reforming. . In addition, the use of air instead of steam for the reforming process in an SOFC system, causes a reduction of the Nernst potential of the cell as the presence of nitrogen lowers the partial pressure of hydrogen at the reactor outlet [56]. However, the exothermic nature of the reaction and the presence of a catalyst, make it possible to realize compact reformers which have a relatively fast response to transient load demands [56]. Additionally, since no steam generators, burners and electric heaters are needed, the complexity of a CPOX system as well as the start-up times, are much lower than a steam reforming system [14].

4.4.1 Pre-Reformer Model

The developed CPOX reformer model estimates the reactor outlet molar concentration and the outlet temperature. A Gibbs free energy minimization approach is used, as suggested by Filippi [56] and Koukkari et al. [58].

The model is 0-D, thus accounting for time variations of the input conditions. The adiabatic chemical reactor is described as only one control volume and spatial variations are omitted. The output variables (i.e. outlet temperature and molar concentration) are estimated by solving a system of mass and energy balance equations. All the gases are assumed to obey the ideal gas law and the pressure losses in the reactor are neglected.

In particular, the reactor outlet composition is defined as the product composition which minimize the system Gibbs free energy by reaching the equilibrium [56]. One of the advantage of this approach lies in not having to specify the chemical reactions occurring in the reformer, but only the species involved (i.e. CH_4, CO_2, CO, H_2, H_2O, N_2, O_2).

The reactor outlet temperature and its time variation are estimated according to an energy balance, assuming an adiabatic process and taking into account the heat capacity of the rector catalyst.

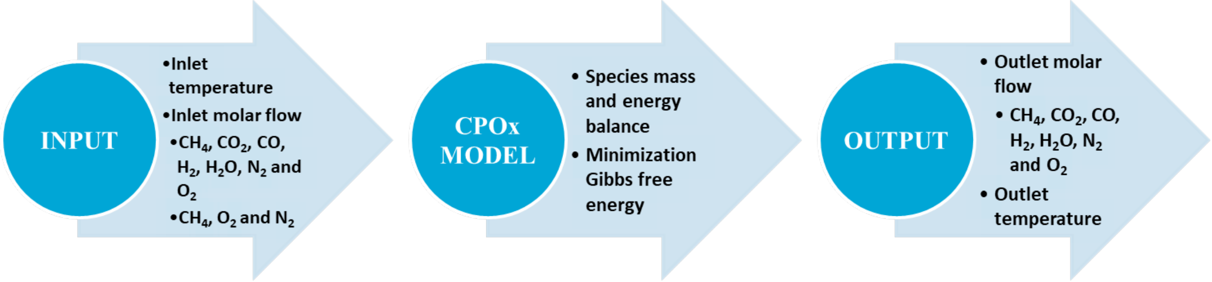

Figure 4.3: Pre- Reformer model approach. The input species involved in the process depend on the reforming process. When anode gas recirculation is involved, not only CH_4, O_2 and N_2 are involved, but also CO, CO_2, H_2 and H_2O. Reproduced from [56].

4.4.1.1 Gibbs Energy Minimization Method

The Gibbs minimization approach is used as alternative to the equilibrium constant approach, to find the equilibrium composition of a system. The equilibrium condition is reached when the composition of the species involved is such that the total entropy of the system reaches a maximum thus not allowing changes in any direction in composition spaces which would involve an entropy decrease [59]. The Gibbs free energy of a species *j* is defined as follow:

$$G_j = U + p \cdot V_j - T \cdot S_j = H_j - T \cdot S_j \tag{4.17}$$

Where U represents the internal energy (J), p the pressure (Pa), V the volume (m^3), T the reaction temperature (K), S the entropy ($J \cdot K$) and H the enthalpy (J). Considering the definition of enthalpy of formation and the pressure correction for ideal gases, the expression (4.17) can be rewritten as follow:

$$G_j = \frac{G_j^*}{R \cdot T} + \ln\left(\frac{N_j}{\sum N_j} \cdot \frac{p}{p_0}\right) \tag{4.18}$$

Where R represents the universal gas constant (8.3145 J/mol K), N_j the outlet molar flow of each species j (mol/s), p the system pressure (Pa) and p_0 the reference pressure ($1.013 \cdot 10^5$Pa). The term G_j^* in (4.18) represents the species free energy of formation, defined as follow:

$$G_j^* = H_{f,j}^0 + (H_j - H_{0,j}) - T \cdot S_j \tag{4.19}$$

Here, $H_{f,j}^0$ is the enthalpy of formation at 298 K, H_j is the enthalpy at the target temperature T, $H_{0,j}$ is the enthalpy at 298 K and S_j is the 1 atm entropy at the temperature T. The thermodynamic properties of the species (i.e. enthalpy and entropy) are calculated according to the Shomate equation with coefficients provided by the NIST WebBook [47,48].

The equilibrium condition is reached when the change of total Gibbs energy of the system is equal to zero, which translates in:

$$dG = \sum_j \left(\frac{G_j^*}{R \cdot T} + \ln\left(\frac{N_j}{\sum N_j} \cdot \frac{p}{p_0}\right)\right) \cdot dN_j = 0 \tag{4.20}$$

In equation (4.20) the N_j are not independent variables. They are constrained such that the number of moles of each element (i.e. C, O, H, N) in the system remains constant. Therefore, the problem translates in a minimization problem with equation (4.20) as objective function that must be solved under the following equality constraint conditions with (4.21) or without (4.22) anode gas recirculation:

$$\begin{aligned}
C &: \quad N_{CH_4,in} + N_{CO_2,in} + N_{CO,in} = N_{CH_4,out} + N_{CO_2,out} + N_{CO,out} \\
H &: \quad 4N_{CH_4,in} + 2N_{H_2,in} + 2N_{H_2O,in} = 4N_{CH_4,out} + 2N_{H_2,out} + 2N_{H_2O,out} \\
O &: \quad 2N_{CO_2,in} + N_{CO,in} + N_{H_2O,in} + 2N_{O_2,in} = 2N_{CO_2,out} + N_{CO,out} + N_{H_2O,out} + 2N_{O_2,out} \\
N &: \quad 2N_{N_2,in} = 2N_{N_2,out}
\end{aligned} \tag{4.21}$$

$$\begin{aligned}
C &: \quad N_{CH_4,in} = N_{CH_4,out} + N_{CO_2,out} + N_{CO,out} \\
H &: \quad 4N_{CH_4,in} = 4N_{CH_4,out} + 2N_{H_2,out} + 2N_{H_2O,out} \\
O &: \quad 2N_{O_2,in} = 2N_{CO_2,out} + N_{CO,out} + N_{H_2O,out} + 2N_{O_2,out} \\
N &: \quad 2N_{N_2,in} = 2N_{N_2,out}
\end{aligned} \tag{4.22}$$

The reactor outlet temperature T is found by applying an enthalpy balance to the system, considering the temperature dynamic term and the adiabatic assumption:

$$\dot{Q} = \sum_j \left(N_{j,out} \cdot H_{j,out} - N_{j,in} \cdot H_{j,in}\right) + k \cdot \frac{dT}{dt} = 0 \tag{4.23}$$

By solving the equation for dT/dt, the outlet temperature is found:

$$\frac{dT}{dt} = -\left(\frac{1}{k}\right) \cdot \sum_j \left(N_{j,out} \cdot H_{j,out} - N_{j,in} \cdot H_{j,in}\right) \tag{4.24}$$

Where k represents the heat capacity of the reactor catalyst (J/K), representing a design parameter of the reactor and dependent mainly on the mass of the catalyst element. A value 0.031 kJ/K of has been chosen based on literature [56]. Figure 4.4 shows an example of the CPOX outlet temperature profile obtained from the pre-reformer model.

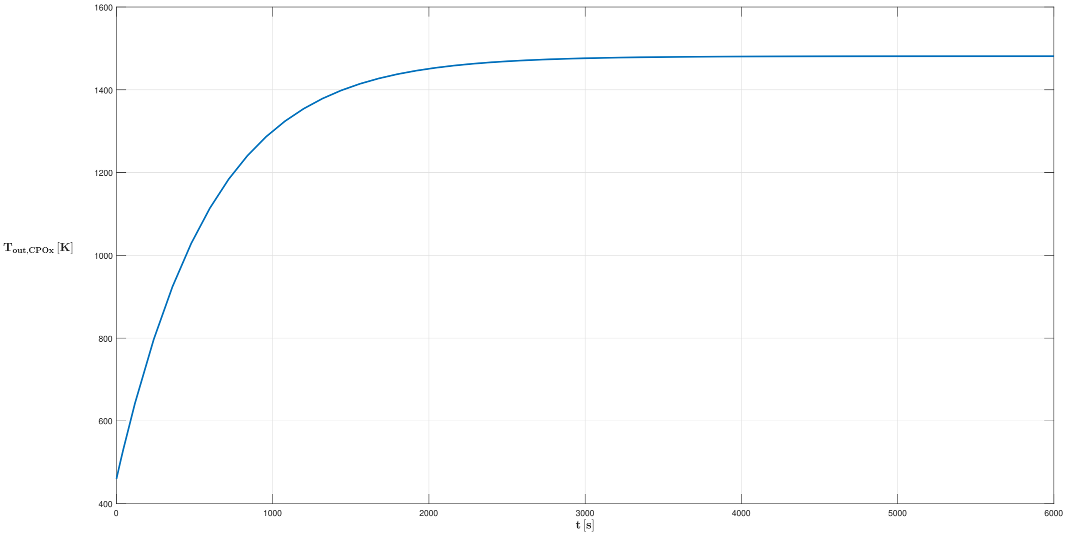

Figure 4.4: Example of pre-reformer outlet temperature profile

4.5 Afterburner

To increase system efficiency and to prevent exhaust of CO, the system is equipped with an afterburner, located downstream the SOFC stack, where the anode and cathode exhausts are mixed and burned. The high temperature exhaust gases exiting the burner are then used in the heat exchangers to pre-heat first the fuel and then the air up to the operating temperature (see Fig. 3.1).

4.5.1 Afterburner Model

Since the combustor is supplied with surplus air (for SOFC cooling purposes, the cathode channels are supply with excess O_2), it is possible to simplify the afterburner modelling. Following the considerations of Lu et al. [64], it is possible to assume complete combustion of H_2, CO and the small amount of CH_4 present at the stack outlet. Consequently, the afterburner exhaust composition is characterized by H_2O, O_2, N_2 and CO_2. The Gibbs minimization approach is used to estimate the outlet molar concentration (see Sec. 4.4.1.1).

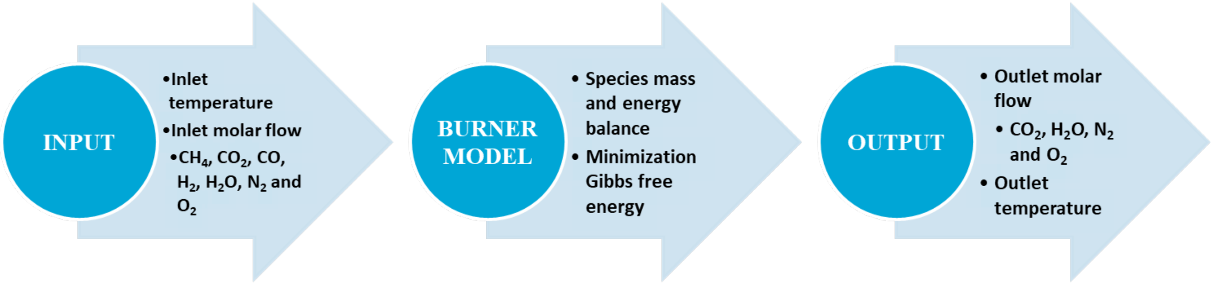

Figure 4.5: Burner model approach.

The combustor outlet temperature is estimated using the adiabatic flame temperature approach [65], according to which the outlet temperature is defined as the highest temperature achievable by a system approaching equilibrium by means of an adiabatic process. The combustor heat losses are neglected and consequently all the combustion heat is used to heat up the products. The value of the outlet temperature is estimated considering that the combustion products enthalpy must equal the reactants enthalpy:

$$\sum_j \mathrm{N_{j,out}} \cdot \mathrm{H_{j,out}(T_{out})} = \sum_j \mathrm{N_{j,in}} \cdot \mathrm{H_{j,in}(T_{in})} \tag{4.25}$$

Where $\mathrm{N_{j,in}}$ and $\mathrm{N_{j,out}}$ represent respectively the molar flows of the species j entering and exiting the combustor (mol/s). $\mathrm{H_{j,in}}$ and $\mathrm{H_{j,out}}$ correspond respectively to the enthalpy of the species j at $\mathrm{T_{in}}$ and $\mathrm{T_{out}}$. The dependency of the enthalpy on the temperature is expressed using the Shomate estimation [47] with coefficients provided by the NIST WebBook [48].

Chapter 5

SOFC Stack Model

The performance of the SOFC stack are estimated using the existing 1-D dynamic developed model by van Biert et al. [21]. The model characteristics, the chosen methodology and the stack characteristics are briefly summarised in this chapter . The reader is encouraged to read the full article [21] describing the SOFC stack model in detail.

5.1 Model Description

The stack model simulates the performance of a commercially available integrated stack module (ISM) containing two 30 cells stack towers connected in series. The model structure and equations are the same as for a single cell model. Geometrical parameters and boundary conditions are adjusted to take into account the difference between stack and single cell operations (see Table 5.1).

The model is a 1 D dynamic capable of accounting for the time variations of the input conditions. The air, fuel, interconnect and positive electrode-electrolyte-negative electrode (PEN) assembly are discretised in the flow direction by using separate control volumes. Additionally, the model accounts for the stack active area, heat transfer in the inactive sections and surrounding heat losses.

All the mass and energy balance equations in the model are dynamic. The gas channels are modelled as a series of stirred-tank reactor control volumes and the dynamics of the species molar concentration are evaluated assuming that the changes in the total molar flow are quasi-static. Therefore, the local time derivative of the molar concentration follows from a molar balance and the molar capacity of the control volume:

$$\frac{\partial y_i}{\partial t} = \frac{\bar{R}\,T}{p\,V_{cv}} \cdot \left(\dot{n}_i{}^{in} - \dot{n}_i{}^{out} + \sum_m v_{i,m}\, r_m\, A_{cv}\right) \tag{5.1}$$

With A_{cv} and V_{cv} being the control volume area (m^2) and volume (m^3) and $\dot{n}$ the molar flow (mol/s) of the species j.

Regarding the dynamic energy balance of the gaseous (5.2) and solid (5.3) control volumes, it is assumed that the heat from the chemical reactions ($\Delta H_m\, r_m$) is assigned to the PEN control volumes rather than the gases. The solid control volumes account for the convective heat transfer (first term right hand side (5.3)) as well as the heat conduction (second term right hand side (5.3)). The term c_p is estimated at each time step according to the Shomate equations but $\frac{d c_p}{dt}$ is neglected.

$$\frac{\partial T_g}{\partial t} = \frac{\bar{R}\,T}{p\,V_{cv}\,\sum_i y_i\, c_{p,i}} \cdot \left[\sum_i \dot{n}_i{}^{in} (h_i^{in - h_i^{out}}) + \sum \bar{h}\, A_{cv}\, (T_s - T_g)\right] \tag{5.2}$$

$$\frac{\partial T_s}{\partial t} = \frac{1}{\rho_s\, c_{p,s}\, \tau_s} \cdot \left[\sum \bar{h}\, (T_g - T_s) + \lambda_s\, \tau_s\, \frac{\partial^2 T_s}{\partial x^2} + \sum_m \Delta H_m\, r_m - j\, U_{cell} - \dot{Q}_{loss}\right] \tag{5.3}$$

The last two terms on the right hand side of equation (5.3) represent respectively the electric power drawn from a control volume and the surroundings heat losses. The latter is applied only at the boundaries of the stack, thus:

$$\dot{Q}_{loss} = \begin{cases} \lambda_{ins}\,(T_{IC} - T_{env}) & \text{if } l = 0 \vee l = L \\ 0 & \text{if } l \neq 0 \vee l \neq L \end{cases} \tag{5.4}$$

5.1.1 Chemical Model

It is assumed that two reactions take place on the SOFC anode, namely Water Gas Shift (WGS) and Methane Steam Reforming (MSR).

$$\text{MSR}: \quad CH_4 + H_2O \leftrightarrow CO + 3\,H_2 \tag{5.5}$$

$$\text{WGS}: \quad CO + H_2O \leftrightarrow CO_2 + H_2 \tag{5.6}$$

The WGS is assumed to proceed infinitely fast. Consequently, the reaction quotient is equal to the equilibrium constant along the active area. The latter is estimated from the Gibbs free energy change of reaction at standard state.

$$Q_{WGS} = \frac{\alpha_{H_2}\,\alpha_{CO_2}}{\alpha_{H_2O}\,\alpha_{CO}} = K_{WGS} = \exp\left(-\frac{\Delta G^0_{WGS}}{\bar{R}T}\right) \tag{5.7}$$

With

$$\alpha_i = \Phi_i\, y_i\, \frac{p}{p_0} \simeq y_i\, \frac{p}{p_0} \qquad \text{ideal gas behaviour} \tag{5.8}$$

The same does not apply for MSR since methane reaction does not proceed infinitely fast. Therefore, a kinetic model is required. In a later research, Biert [50] compared four different kinetic models to investigate the dependence of the MSR rate on the methane and steam partial pressures. Here only the model used in this research is reported. The latter goes under the name of Langmuir-Hinshelwood kinetic model. In this model, the reaction rate (r_{MSR}) is defined as follow:

$$r_{MSR} = \frac{k\,\bar{K}_{CH_4}\,\bar{K}_{H_2O}\,p_{CH_4}\,\sqrt{p_{H_2O}}}{\left(1 + \bar{K}_{CH_e}\,p_{CH_4} + \bar{K}_{H_2O}\,\sqrt{p_{H_2O}}\right)^2} \cdot \left(1 - \frac{Q_{MSR}}{K_{MSR}}\right) \tag{5.9}$$

Here the numerator represents the kinetic factor, which describes the dependency of the rate determining step on the gas species involved. The denominator represents the adsorption isotherm which accounts for the available active reaction sites. While, the ratio of Q_{MSR} and K_{MSR} represents the deviation from chemical equilibrium thus the driving force of the reaction [50].

5.1.2 Electrochemical Model

The stack power density is estimated by multiplying the average current density (j) with the cell voltage (U_{cell}). It is assumed that the voltage is uniform on the cell plane. The resulting cell voltage corresponding to the total current drawn, is estimated using the bisection algorithm. In particular, the current density distribution is calculated such that the sum of the overpotentials equals the difference between cell voltage and the Nernst voltage (U_{Nerst}):

$$U_{Nernst} - U_{cell} = \eta_{ohm} + \eta_{conc} + \eta_{act,an} + \eta_{act,cat} \tag{5.10}$$

The Nernst potential, in eq.(5.10), is estimated considering that the kinetics of hydrogen oxidation dominate the electrochemical reaction:

$$U_{Nernst} = \frac{\Delta G^0}{2F} + \frac{\bar{R}T_{PEN}}{2F} \ln\left(\frac{\sqrt{\alpha_{O_2}} \cdot \alpha_{H_2}}{\alpha_{H_2O}}\right) \tag{5.11}$$

Where the first term of the right hand-side represents the reversible potential for hydrogen oxidation at standard pressure (p_0) and average PEN temperature [21].

The overpotentials (right hand-side terms of equation (5.10)) represent irreversible losses which occurs in practical fuel cells. These losses, divided in ohmic (η_{ohm}), activation (η_{act}) and concentration (η_{conc}) losses, result in a cell voltage lower than its ideal voltage [14], as shown in Figure 5.1.

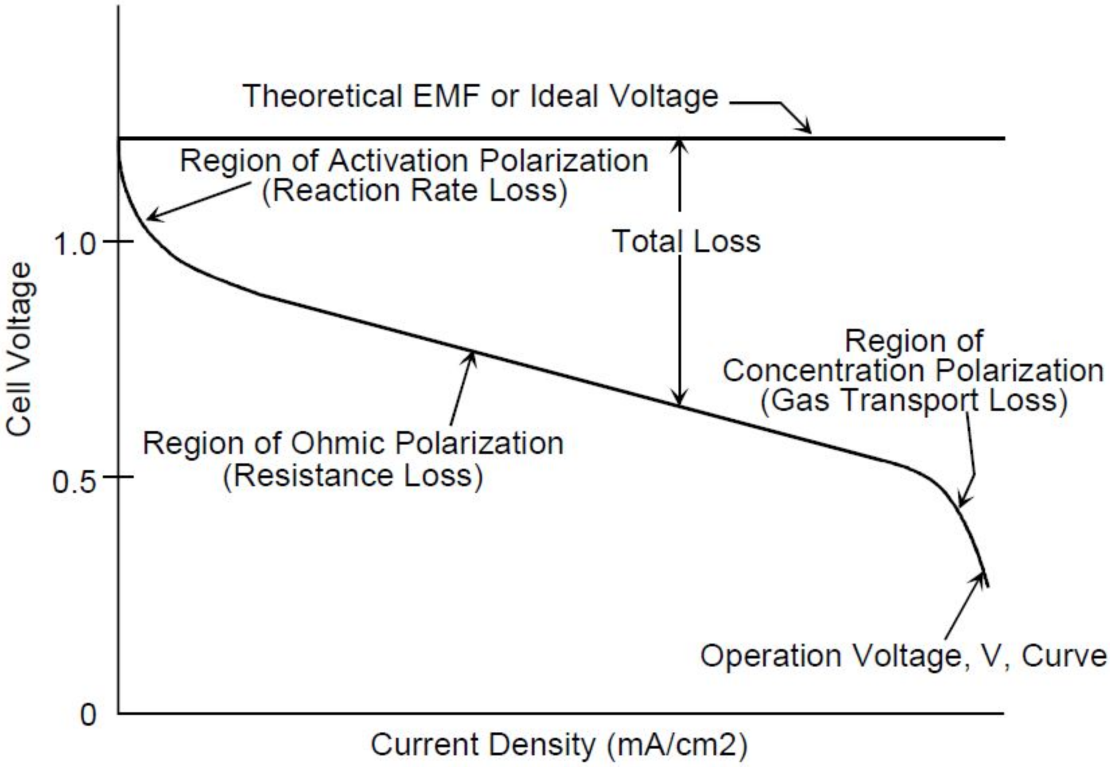

Figure 5.1: Ideal and actual fuel cell current/voltage characteristics. The ideal voltage represents the theoretical electromotive force (EMF). Reproduced from [14].

It is important to understand that, Ohmic losses occur because of resistance to the flow of ions and electrons respectively in the electrolyte and through the electrode materials [14]. These losses are directly proportional to the anode, cathode and electrolyte thickness (τ) and inversely proportional to their electronic or ionic conductivity (σ). Due to their limited dependence on the PEN temperature, σ_{an} and σ_{ca} are estimated as constant values , while σ_{el} is estimated as function of the local PEN temperature (as reported in Table 5.1). Moreover, in order to account for non-ideal electrical contacts in the stack assembly, a contact resistance factor ($R_{contact}$) is considered [21]. The electrolyte and electrode properties value are reported in Table 5.1.

$$\eta_{ohm} = j \cdot \left(\frac{\tau_{an}}{\sigma_{an}} + \frac{\tau_{el}}{\sigma_{el}(T_{PEN})} + \frac{\tau_{ca}}{\sigma_{ca}} + R_{contact}\right) \tag{5.12}$$

Concentration losses occur because of the inability of the surrounding material to maintain the initial concentration of the bulk fluid, thus deviating from the gas concentrations at the triple phase boundary (tbp). These losses usually dominate only for higher current densities [14, 21] and are estimated considering the reactant partial pressure at tpb. :

$$\eta_{conc} = \frac{\bar{R}T}{2F} \ln\left(\frac{p_{H_2O,tpb} \cdot p_{H_2}}{p_{H_2O} \cdot p_{H_2,tpb}}\right) + \frac{\bar{R}T}{4F} \ln\left(\frac{p_{O_2}}{p_{O_2,tpb}}\right) \tag{5.13}$$

Where $p_{i,tpb}$ is estimated considering the bulk flow partial pressures and the effective diffusion coefficient as suggested by van Biert [21].

Finally, the activation losses are directly related to the rate of electrochemical reaction [14] and can be estimated assuming symmetry between the anodic and cathodic reaction:

$$\eta_{act} = \frac{\bar{R}T}{F} \cdot \sinh^{-1}\left(\frac{j}{2j_0}\right) \tag{5.14}$$

Where:

$$j_{0,ca} = \hat{k}_{o,ca} \cdot \alpha_{O_2}^{\hat{\varepsilon}} \exp\left(-\frac{E_{\alpha,ca}}{\bar{R}T}\right) \tag{5.15}$$

$$j_{0,an} = \hat{k}_{o,an} \cdot \alpha_{H_2}^{\hat{\gamma}} \cdot \alpha_{H_2O}^{\hat{\beta}} \exp\left(-\frac{E_{\alpha,an}}{\bar{R}T}\right) \tag{5.16}$$

Here, the values reaction orders $\hat{\varepsilon}$, $\hat{\gamma}$ and $\hat{\beta}$ depend on several factors (e.g. temperature, absolute electric potential difference). A value of 0.25, 0.5 and 0 is chosen respectively [21].

Table 5.1: Parameters assumed in the stack and single cell test setup, based on ESC2 cells obtained from Kerafol/H.C. Starck and the ISM V3.3 from Sunfire/Staxera. Reproduced from [21]

Geometric Properties	**Symbol**	**Units**	**ISM**	**Single Cell**
N. of cells	N_{cell}	[-]	60	1
Cell length	L_{cell}	[m]	0.164	0.1
Active area length	L_{aa}	[m]	0.09	0.09
Cell width	w_{cell}	[m]	0.142	0.09
N. of channels	N_{ch}	[-]	24	22
Channel height	τ_{ch}	[m]	1e-3	2.5e-3
Electrolyte thickness	τ_{el}	[m]	90e-6	90e-6
Anode thickness	τ_{an}	[m]	35e-6	35e-6
Cathode thickness	τ_{ca}	[m]	35e-6	35e-6
Interconnect thickness	τ_{IC}	[m]	500e-6	-
N. of control volumes	N_{cv}	[-]	50+(2x21)	250

Thermal Properties				
PEN density	ρ_{PEN}	[kg m^{-3}]	5900	
PEN heat capacity	$c_{p,PEN}$	[J kg^{-1} K^{-1}]	500	
PEN thermal cond.	λ_{PEN}	[W m^{-1} K^{-1}]	2	
IC density	ρ_{IC}	[kg m^{-3}]	8000	
IC heat capacity	$c_{p,IC}$	[J kg^{-1} K^{-1}]	500	
IC thermal cond.	λ_{IC}	[W m^{-1} K^{-1}]	24	
Ins. thermal cond.	λ_{ins}	[W K^{-1}]	2.91e-3	

Electrolyte and Electrode Properties				
Electrolyte conductivity	σ_{el}	[Ω^{-1} m^{-1}]	20.5e3exp(–9.03e3/T_{PEN})	
Anode conductivity	σ_{an}	[Ω^{-1} m^{-1}]	30e3	
Cathode conductivity	σ_{ca}	[Ω^{-1} m^{-1}]	12.9e3	
Contact resistance	$R_{contact}$	[Ω m^2]	5e-6	5.5e-5
Electrode porosity	ε	[-]	0.3	
Electrode tortuosity factor	l	[-]	6	
Electrode pore radius	$\bar{r}$	[m]	5e-7	

Chapter 6

Control System Model

The controller for the proposed SOFC system configuration has two objectives, namely to efficiently follow the power requirement during load transients and to respect the operating limit set by the manufacturer on the stack core temperature to ensure safe operation. Two main control systems are developed for the proposed SOFC system configuration. This chapter describes in detail the chosen control strategies and shows how they have been implemented in the complete system model.

6.1 PEN Temperature Control

The operating temperature of SOFCs is usually higher than other fuel cells, and as a result, the thermal stress between different components due to different temperature distributions along the anode, cathode, and electrolyte can be critical for the entire fuel cell integrity [15]. Large temperature gradients in the stack might affect the interconnect and the cell properties causing cell degradation, reduction of system efficiency and possible system failure [52]. Therefore, it is importantto maintain the temperature profile of the PEN assembly (representing the core of the cell) as uniform as possible.

A low level control is implemented to make the SOFC stack work at the desired PEN temperature, based on the work done by Marra et al. [15]. A feedback control logic is applied to the cathode air blower, by means of a proportional–integral-derivative (PID) controller (see Figure 6.1). The controller feeds the (excess) air required to meet the desired temperature value of the PEN assembly (T_{TARGET}). If T_{PEN} increases to a value higher than the target value, the air flow is increased to cool the stack. The opposite is true if the PEN temperature reduces to a value below T_{TARGET}. The applied PID controller is discrete and updates the cathode air flow every 700 s and thus the power of the air blower system.

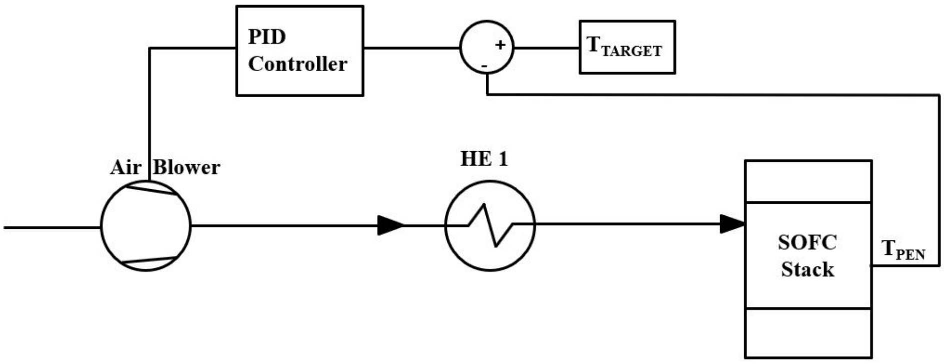

Figure 6.1: Overview of the the PEN temperature control system.

The Ziegler-Nichols frequency response method has been used to tune the PID controller. This method consist of setting the integral and derivative gains (i.e. Ki, Kd) to zero. The proportional gain (i.e. Kp) is increased until it reaches the ultimate gain Ku, representing the value at which the output of the loop starts to oscillate constantly with a period T_u, known as ultimate period [10]. Then the values of Ki and Kd are found as follows:

Table 6.1: PID Control parameters based on Ziegler-Nichols method. Reproduced from [10, 11]

Controller Type	$\mathbf{K_p}$	$\mathbf{K_i}$	$\mathbf{K_d}$	$\mathbf{T_p}$	$\mathbf{T_i}$	$\mathbf{T_d}$
P	0.5 K_u	-	-	T_u	-	-
PI	0.45 K_u	0.54 K_u / T_u	-	1.4 T_u	0.8 T_u	-
PID	0.6 K_u	1.2 K_u/ T_u	3 K_u T_u /40	0.85 T_u	0.5 T_u	0.125 T_u

The values used in the model for the proportional, integral and derivative gains are respectively, Kp = 0.5, Ki = 0.01 and Kd = 0.01.

6.2 Power Demand Control

The SOFC power controller is a feed-forward control system (see Figure 6.2). The controller estimates the current requirement based on the power demand with a look-up table. The look-up table data (see Figure 8.1) has been obtained by running the model for different stack current to estimate the net power produced by the SOFC system.

The effect of stepping and ramping the current is evaluated. By changing the current, the amount of fuel feeding the system changes instantaneously so to keep the system fuel utilization constant and equal to the nominal value, according to relation (8.1).

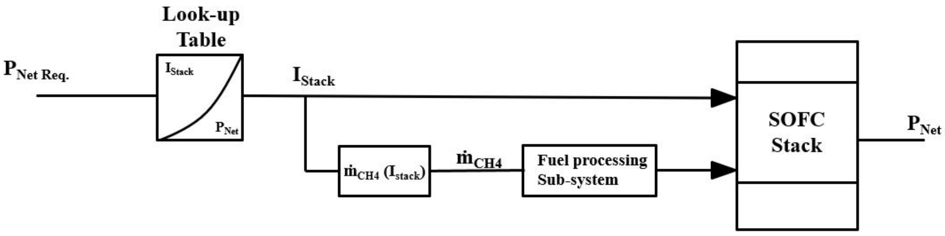

Figure 6.2: Overview of the SOFC power control system.

Chapter 7

Model Verification

The BoP components of the developed model have been verified with steady-state results obtained from the thermodynamic flow-sheet modelling software Cycle-Tempo ®. Each component was individually verified at different operating points. The results obtained are described in this chapter. Verification and validation of the SOFC stack model has already been carried by Biert et al. [21] and is omitted in this chapter.

7.1 Air Blower

Verification of the blowers is obtained through the estimation of the power required for different values of the mass flow. Figure 7.1 shows the comparison of the results provided by Cycle-Tempo (▲) for the air blower with those estimated with the developed model (■), according to eq. (4.1). The considerations are the same for the CPOX and AGR blower with the exceptions of the mass flow species for the latter.

The cathode air flow is increased to simulate the need of the air blower to provide excess air to the stack for cooling purposes. The results show how the developed blower model predicts with excellent accuracy the blower required power.

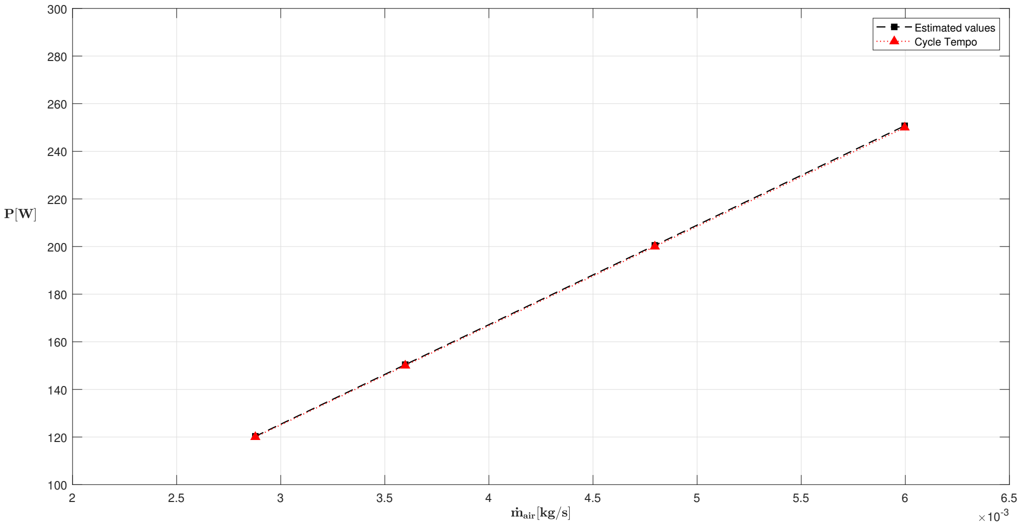

Figure 7.1: Verification of the air blower power estimation. (The reported air flow refers to the amount necessary for the whole stack, not the single cell).

7.2 Heat Exchanger

The air heat exchanger model is verified by varying the amount of cathode air flow entering the HEx (representing the cold fluid) and observing the effect on the outlet hot and cold fluid temperature. The hot fluid mass flow is kept constant for all the values of $\dot{m}_{air}$. Figure 7.2 shows the results obtained with the model (■ ●) compared to the results obtained from Cycle Tempo (▲ ▼). It is possible to observe a small discrepancy between the results, with a bigger magnitude for the cold fluid than for the hot fluid. The temperature difference of the cold fluid between the simulated values and the ones obtained from Cycle Tempo is almost 30 K for all the $\dot{m}_a$ir values. While for the hot fluid, this difference is less than maximum 6 K.

The difference between the data might be attributed to the different approach used to estimate the thermodynamic properties of the gas mixture. While the developed model uses the Shomate equations with coefficient provided by the NIST WebBook [48], Cycle Tempo uses a similar expression but with coefficient provided by NASA [49]. These are slightly different from those provided by the NIST (see Appendix B).

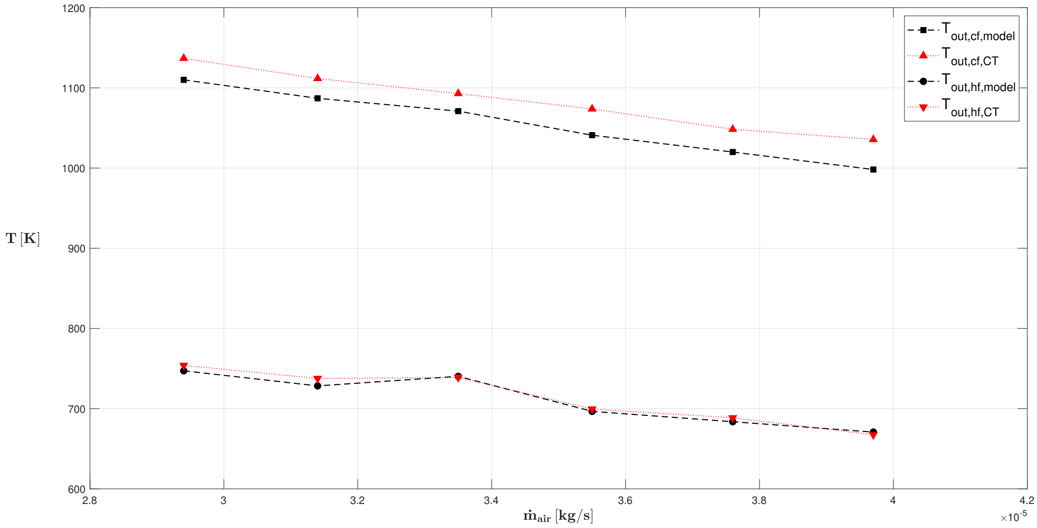

Figure 7.2: Verification of the air heat exchanger outlet temperatures. The reported air flow refers to the amount necessary for single cell operation.

7.3 Mixer

Figure 7.3 shows the verification results of the adiabatic mixer outlet temperature in relation to the fuel mass flow. The same considerations apply for the mixer located upstream the after-burner (see Fig. 3.1). In particular, $\dot{m}_{mix}$ is increased by increasing the amount of methane entering the mixer. The CPOX air flow and the AGR flow are kept constant. The change of the fuel mass flow simulates the need of keeping the system fuel utilization constant in case the stack current changes. As expected, by increasing the mixer mass flow, the outlet temperature decreases since more fuel at lower temperature is introduced in the mixer. By comparing the results provided by Cycle-Tempo (▲) with those estimated by the developed model (■), it is possible to conclude that the developed mixer model predicts with good accuracy the mixer outlet temperature changes caused by the variation of $\dot{m}_{mix}$.

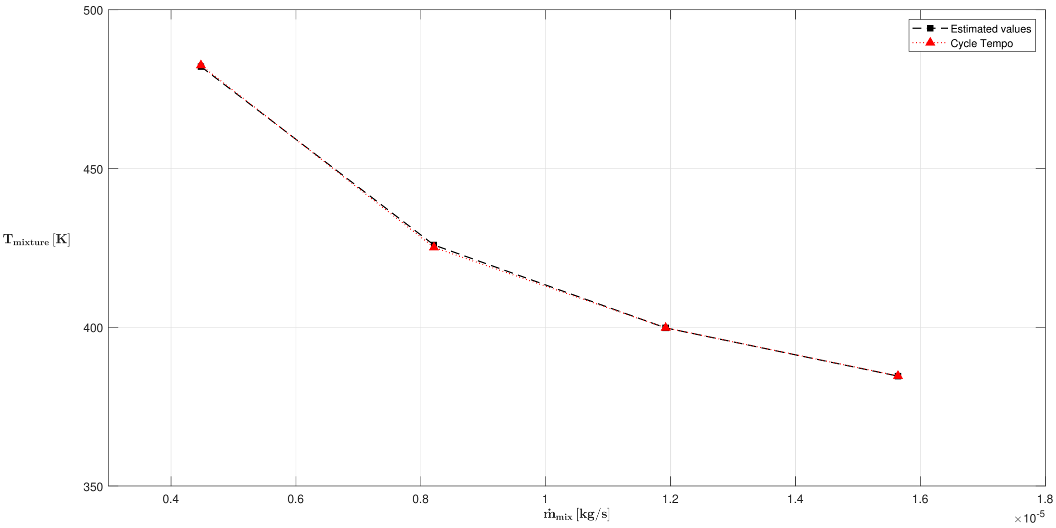

Figure 7.3: Verification of adiabatic mixing process. The displayed results refer to the adiabatic mixer located upstream the CPOX reformer.

7.4 Pre-Reformer

Verification of the CPOX reformer model is done by varying the outlet temperature of the reactor and observing the consequent variation of the outlet molar concentration for operations where the CPOX blower is turned on. As already mentioned in Sec. 4.4.1, the pre-reformer outlet composition is characterised not only by the presence of CO_2 and H_2O, but also H_2 and CO. N_2 is part of the molar composition as air is supplied for the CPOX process.

Figure 7.4 shows how the results obtained (■) are perfectly in accordance with the ones provided by Cycle-Tempo (▲). The variation of the outlet temperature from 950 K to 1275 K has a small effect on the outlet composition.

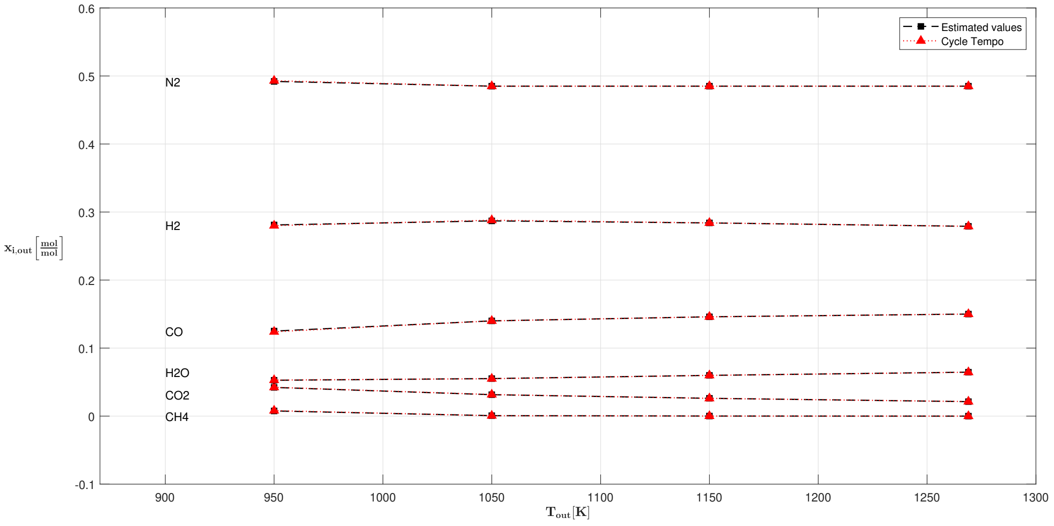

Figure 7.4: Verification of CPOX outlet molar composition. The presence of N_2 in the outlet molar composition is because air (21% O_2 and 79% N_2) is used as oxidant.

7.5 Afterburner

The combustion process occurring in the afterburner located downstream the stack is verified by observing the effect of the cathode exhaust air, on the outlet molar composition. The latter is increased by increasing the cathode air supplied to the system. The situation studied might occurs if more air is needed in the system so to reduce the PEN temperature to the operating value. Since complete combustion of CH_4, CO and H_2 is assumed, the outlet composition consists of N_2, O_2, CO_2 and H_2O. The results obtained are shown in Figure 7.5. A perfect accordance with the Cycle-Tempo data is obtained.

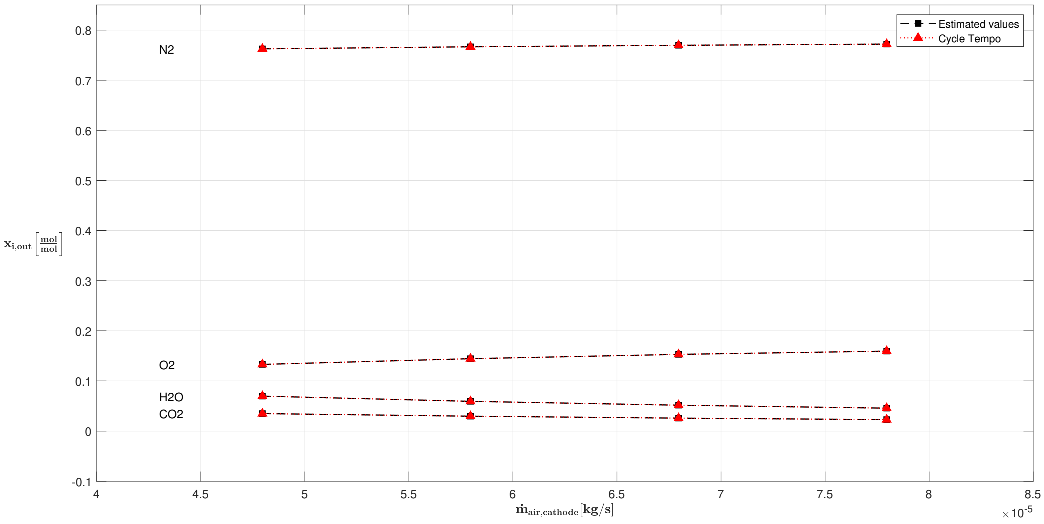

Figure 7.5: Verification of combustor outlet molar composition. The amount of air is increased while the fuel is kept constant.

Chapter 8

Steady-State Results and Discussion

The developed model is able to simulate steady-state operation. The influence of stack current, system fuel utilization and anode recirculating ratio on the system performance has been studied. The results obtained are presented in this chapter.

The BoP components of the modelled system are sized according to the system nominal operation, with characteristics as reported in Table 8.1. During nominal operation, the CPOX air blower is turned off, thanks to the high anode recirculating ratio which ensure that the O/C ratio is kept constant. Oxygen utilization, system and stack global fuel utilization in Table 8.1 are defined as follow:

$$U_{f,sys} = \frac{I}{8 \cdot F \cdot N_{CH_4}} \tag{8.1}$$

$$U_{f,sp,stack} = \frac{I}{2 \cdot F \cdot N_{f,in} \cdot (n_{H_2} + n_{CO} + 4 \cdot n_{CH_4})} \tag{8.2}$$

$$U_{f,g,stack} = \frac{U_{f,sp}}{RR \cdot U_{f,sp} + (1 - RR)} \tag{8.3}$$

$$U_{ox} = \frac{I}{4 \cdot F \cdot N_{O_2}} \tag{8.4}$$

Where F represents the Faraday's constant [sAmol^{-1}], $N_{f,in}$ the fuel total molar flow entering the stack [mol/s], N_{CH_4} the methane molar flow entering the system [mol/s] and n_j the molar fraction of the species j.

Table 8.1: Main system parameters characterising the nominal operation. The O/C ratio is estimated at the inlet of the external CPOX reformer. The highlighted values represent the stack manufacturer recommendation [74].

Parameters	Symbol	Unit	Nominal Value	Range
System Fuel Utilization	$U_{f,sys}$	[-]	0.8	0.7 - 0.9
Stack Global Fuel Utilization	U_{fg}	[-]	0.8	0.7 - 0.9
Anode Recirculating Ratio	RR	[-]	0.7	0 - 0.7
Oxygen to Carbon Ratio	O/C	[-]	2.25	2.25
PEN Temperature	T_{PEN}	[°C]	850	850 - 860
Stack Current	I_{stack}	[A]	27	$\leq$ 30
Stack Voltage	U_{stack}	[V]	37	36 - 80

Table 8.2 shows the results obtained for each subsystem, during nominal operation. The manufacturer operating limits are respected. During nominal operation, the SOFC stack produces 1 kW of electric power corresponding to a stack efficiency of 48%.

However, the cathode air blower as well as the AGR blower require electrical power (drawn from the stack), reducing the available system electric power which translates in a net system efficiency of 38 %.

Table 8.2: Model results for nominal operation.

Air Sub-System Parameters	**Symbol**	**Unit**	**Value**
Total air blower power	P_{air}	[W]	99.56
Air mass flow (single cell)	$\dot{m}_{\text{air}}$	[kg/s]	3.97e-5
Air heat exchanger cold fluid inlet temperature	$T_{\text{cf,in}}$	[K]	331.2
Air heat exchanger cold fluid outlet temperature	$T_{\text{cf,out}}$	[K]	976.4
Air heat exchanger hot fluid inlet temperature	$T_{\text{hf,in}}$	[K]	1241
Air heat exchanger hot fluid outlet temperature	$T_{\text{hf,out}}$	[K]	648.6

Fuel Sub-System Parameters			
Fuel heat exchanger cold fluid inlet temperature	$T_{\text{cf,in}}$	[K]	331.2
Fuel heat exchanger cold fluid outlet temperature	$T_{\text{cf,out}}$	[K]	725
Fuel heat exchanger hot fluid inlet temperature	$T_{\text{hf,in}}$	[K]	1267
Fuel heat exchanger hot fluid outlet temperature	$T_{\text{hf,out}}$	[K]	1241
Adiabatic mixer outlet temperature	T_{mix}	[K]	1085
CPOX reformer outlet temperature	$T_{\text{out,CPOX}}$	[K]	842.7
Methane mass flow (single cell)	$\dot{m}_{\text{CH}_4}$	[kg/s]	7.01e-7

SOFC Stack Parameters				**Op. Limits [74]**
Cathode air inlet temperature	$T_{\text{ca,in}}$	[K]	976.4	≤ 1123
Cathode air outlet temperature	$T_{\text{ca,out}}$	[K]	1084	≤ 1103
Anode fuel inlet temperature	$T_{\text{f,in}}$	[K]	842.7	≤ 1123
Anode fuel outlet temperature	$T_{\text{f,out}}$	[K]	1083	≤ 1123
Anode-Cathode inlet temperature gradient	$\Delta T_{\text{a,c,in}}$	[K]	133.7	≤ 250
Maximum PEN temperature	$T_{\text{PEN,Max}}$	[K]	1123.15	≤ 1133
Single cell voltage	U_{cell}	[V]	0.626	≥ 0.6
Single cell power	P_{cell}	[W]	16.9	
Stack outlet power	P_{stack}	[W]	1015	
Stack current	I_{stack}	[A]	27	≤ 30
Stack global fuel utilization	U_{fg}	[-]	0.8	≤ 0.8
Stack efficiency	η_{stack}	[% LHV]	48	

Other Parameters			
Total AGR blower power	P_{AGR}	[W]	80.71
Anode recirculating ratio	RR	[-]	0.7031
Anode recirculating flow temperature	T_{AGR}	[K]	1165
Adiabatic mixer outlet temperature	T_{mix}	[K]	1084
Afterburner outlet temperature	T_{burner}	[K]	1267
System efficiency	η_{sys}	[% LHV]	38

8.1 Influence of Stack Current

The developed model is able to simulate the system performance for different values of the stack current. When changing the current, the amount of methane feeding the system changes in order to keep the system fuel utilization constant (according to relation (8.1)). Moreover, for all the simulated current values, the CPOX air blower is turned off since O/C ratio, RR and $U_{f,sys}$ are kept constant (see eq. (4.14)). The high anode recirculating ratio ensures that the amount of O_2 required in the pre-reformer is achieved without the need of the CPOX blower. The SOFC stack power curve is obtained by running the model for different values of stack current I_{stack}. The results are shown in Figure 8.1. During nominal operation (i.e. I= 27 A), the SOFC stack is able to deliver more than 1 kW of electric power, and at a stack current (I_{stack}) of 12 A the power reduces to a value below 600 W. The cell voltage, decreases for higher current values (as expected), reaching 0.63 V during nominal operation (see Figure 8.2).

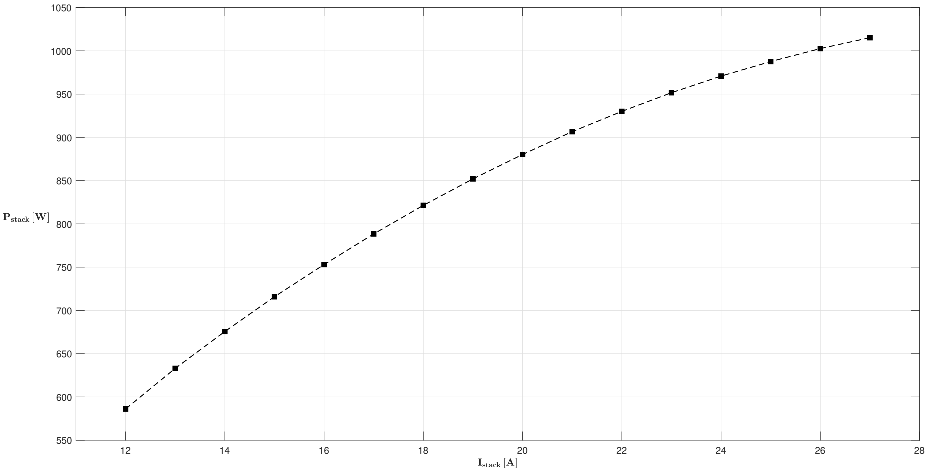

Figure 8.1: Simulated power curve of the SOFC stack ($U_{f,sys}$ = 0.8, RR = 0.7).

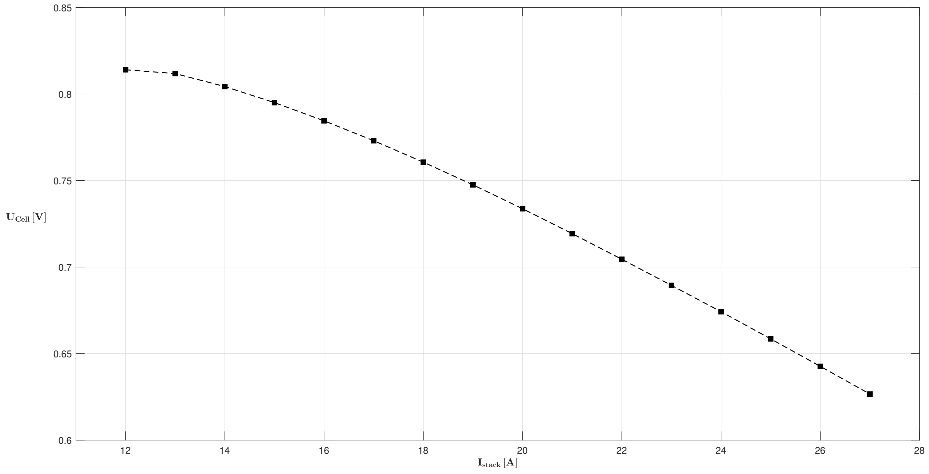

Figure 8.2: Simulated IV curve of the SOFC stack ($U_{f,sys}$ = 0.8, RR = 0.7). The current density has been obtained by dividing the stack current value for the cell active area.

Figure 8.3 shows the combined power and voltage curves for different current density values. The solid lines represent the simulated values obtained with the model. While, the dashed lines represent the values obtained from the data extrapolation considering that no power is produced when no current is drawn from the stack.

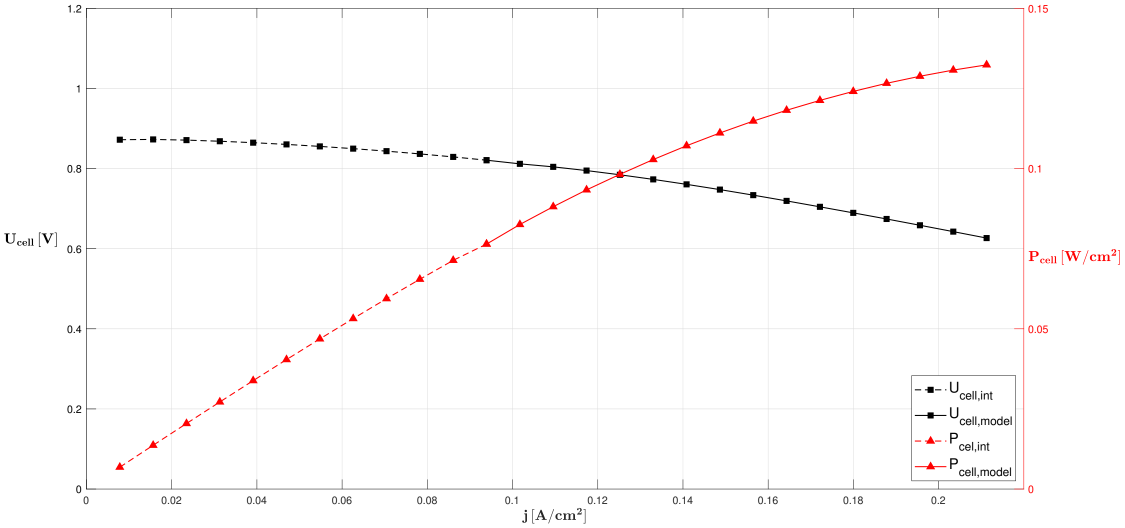

Figure 8.3: Combined I-V and power density curves. The model is not able to simulate the system performance for stack current values below 12 A. A control strategy not solely dependent on the cathode air flow, would allow the model to simulate the system performance for lower I_{stack} values.

For the chosen operating point, the developed model is not able to simulate the system performance for values of stack current below 12 A. The cathode air flow is used to control the PEN temperature. Thus, when reducing the stack current values, the PEN temperature control responds by reducing the cathode air flow (as shown in Figure 8.4)) to keep the maximum PEN temperature equal to 850 °C. However, current values below 12 A result in a reduction of the cathode air flow below the lower limit imposed by the manufacturer. The latter suggests a minimum cathode air flow of 40 Nl/min (corresponding to $1.0\mathrm{e}-5$ kg/s for single cell operation) and an oxygen utilization below 60 % [74].

Figure 8.4 shows the influence of the stack current on the methane and cathode air mass flow. The amount of methane increases for higher current values in order to keep the system fuel utilization constant. The increase of the cathode air is required to cool down the stack and keep the temperature of the PEN assembly constant (at 1123.15 K [74]). If the PEN temperature control would not have been implemented, then the PEN temperature would increase above the maximum limit negatively affecting the stack performance and lifetime. Moreover, the cell voltage would decrease for lower current values with consequently even lower value of the produced power.

In Figure 8.4, it is also possible to see how for I_{stack} values around 12-13 A, $\dot{m}_{air}$ reaches a value below the lower limit imposed by the manufacturer ($1\mathrm{e}-5\,\mathrm{kg/s}$ for single cell operation). Figure 8.5, shows that these I_{stack} values correspond to the highest values of oxygen utilization, 47% and 67% for I_{stack} equal to 13 and 12 A respectively (the manufacturer suggests $U_{ox} \leq 60\%$).

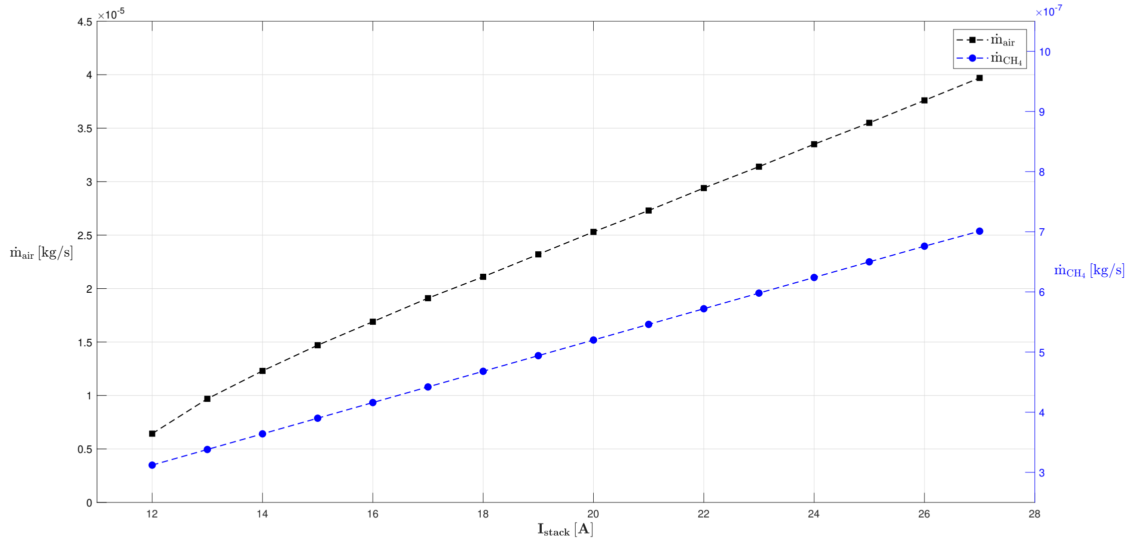

Figure 8.4: Methane and cathode air mass flow for different values of the stack current. ($U_{f,sys}$ = 0.8, RR = 0.7)

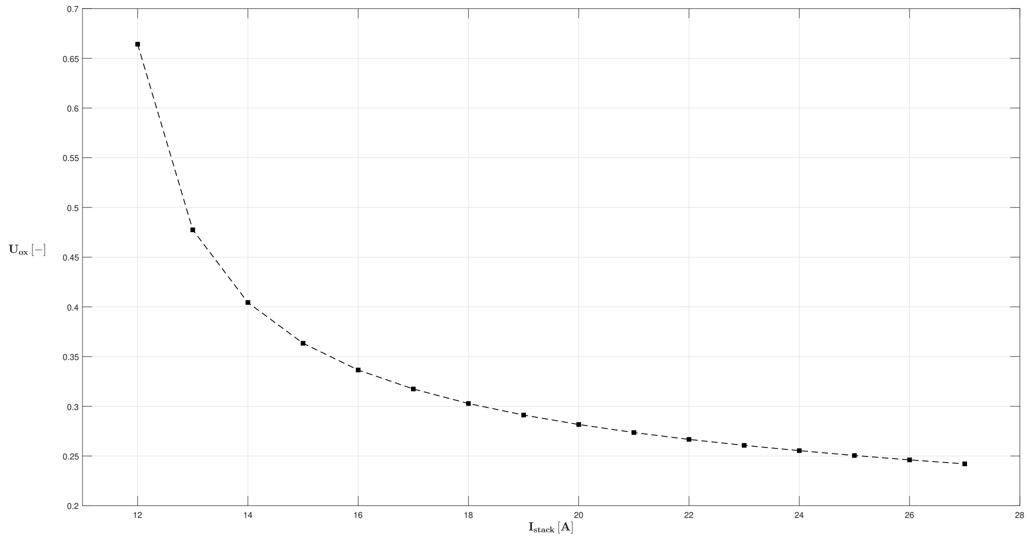

Figure 8.5: Oxygen utilization values for different I_{stack}. ($U_{f,sys}$ = 0.8, RR = 0.7)

The power requirement of the ancillary devices is shown in Figure 8.6. Since the CPOX air blower is not needed thanks to the selected anode recirculating ratio, only the anode recirculating blower and the cathode blower are active. During nominal operation, the required AGR blower and the cathode air blower power represents respectively 8% and 10% of the total electric power produced by the stack (see Figure 8.7). The values reduces to 6% and 3% respectively for I_{stack} = 12 A, since less air and fuel is needed for lower stack currents, as shown in Figure 8.4.

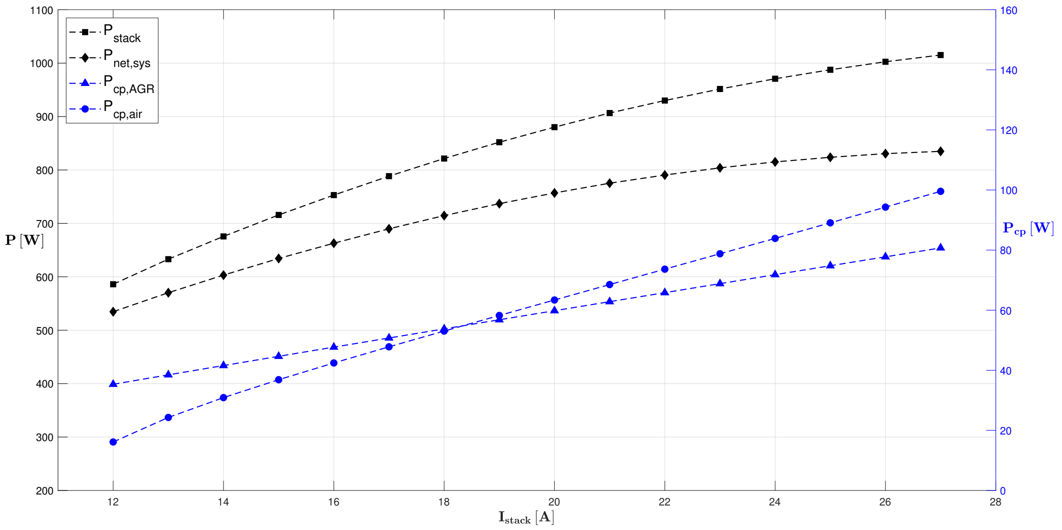

Figure 8.6: P-I curves for the system ancillary devices. ($U_{f,sys}$ = 0.8, RR = 0.7).

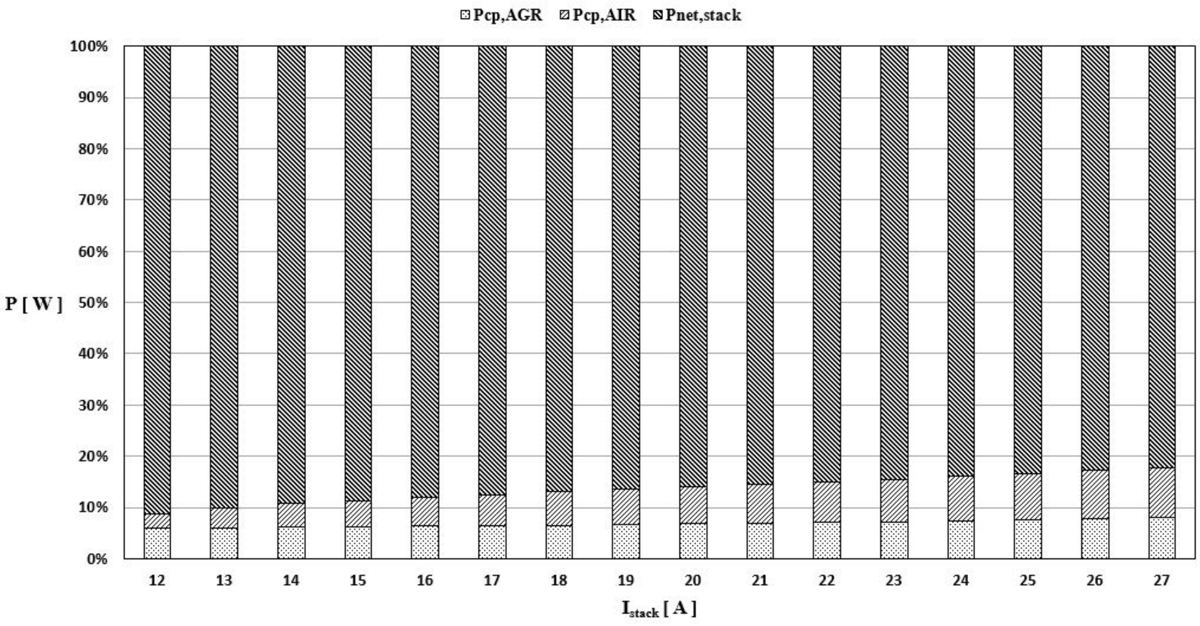

Figure 8.7: Percentage of the power requested by the ancillary devices for different I_{stack} ($U_{f,sys}$ = 0.8, RR = 0.7)

Figure 8.8 shows the variation of the fuel and oxidant flow temperature with the stack current. $T_{a,in}$ represents the outlet temperature of the air exiting HE1. This is the air temperature at the stack inlet (see Fig. 3.1). $T_{f,in}$ represents the fuel temperature at the CPOX reformer outlet thus the stack inlet. And $T_{f,HEx,out}$ represents the outlet temperature of the methane flow exiting HE2 thus prior the CPOX reformer. The increase of $T_{a,in}$ and $T_{f,HEx,out}$ for lower value of stack current is a result of the decrease of the air and fuel flow that occurs for lower I_{stack}, since both heat exchangers (HE1 and HE2) are sized for nominal operation (where the flows reaches the highest simulated values).

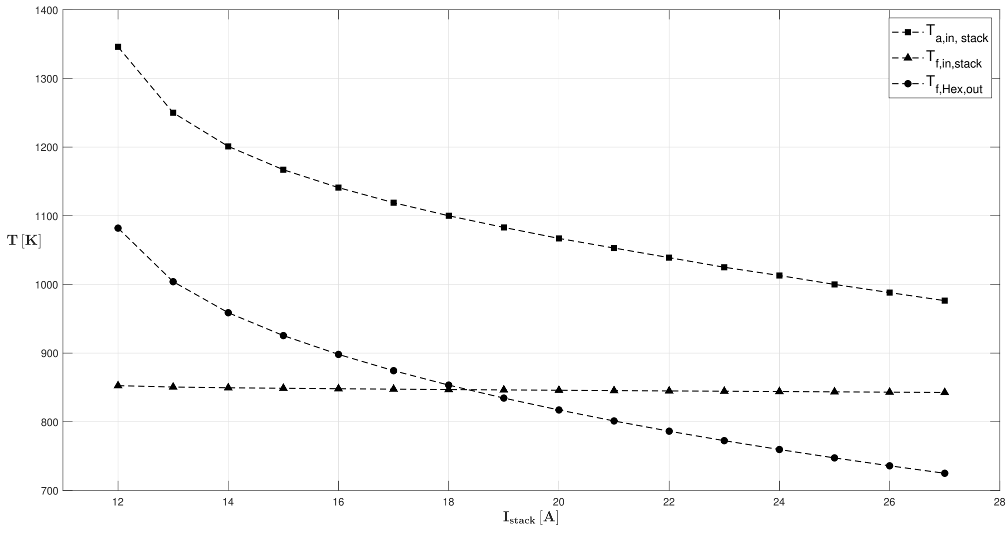

Figure 8.8: Influence of the stack current on the air and fuel stack inlet temperature ($U_{f,sys}$ = 0.8, RR = 0.7).

Figure 8.9 and 8.10 show the effect of the stack current change on the afterburner outlet temperature and molar composition. A significant drop of $T_{out,burner}$ from 1510 K to 1330 K may be observed for I_{stack} values between 12 A and 16 A, after which the change in the the outlet temperature reduces, reaching a value of 1267 K for I_{stack} = 27 A.

The N_2 and O_2 change remarkably for different stack current values, while H_2O and CO_2 remains almost constant. The change in the first two species is a result of the change in the cathode air flow. Since the CPOX blower is turned off, the presence of N_2 and O_2 in the afterburner outlet composition is attributed only to the cathode air flow.

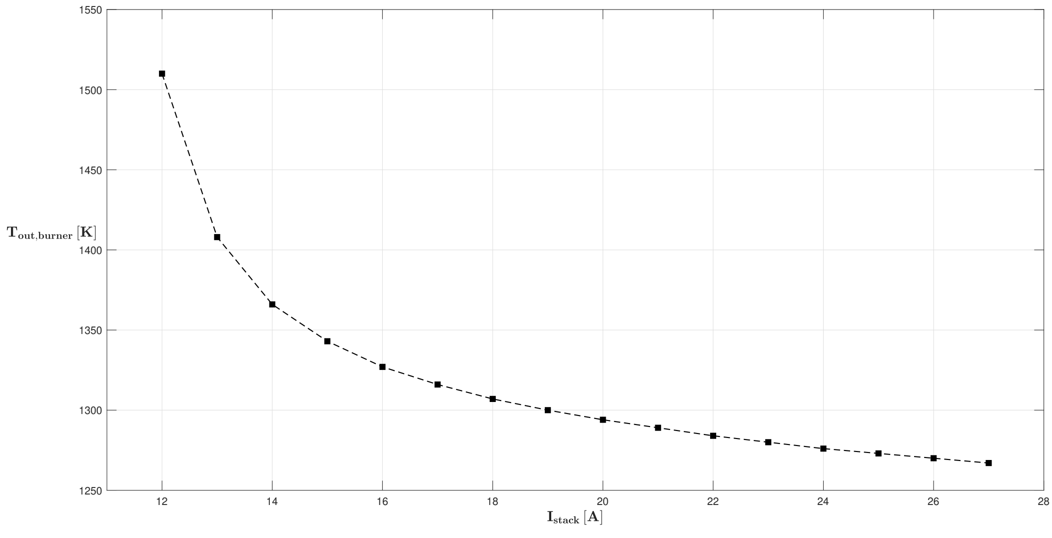

Figure 8.9: Influence of the stack current on the outlet temperature of the afterburner ($U_{f,sys}$ = 0.8, RR = 0.7).

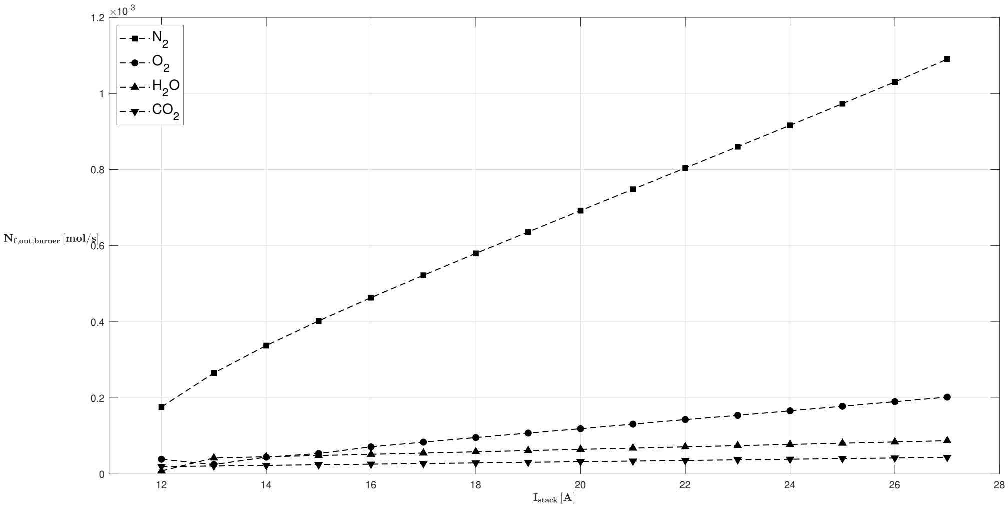

Figure 8.10: Influence of stack current on the molar flow at the afterburner outlet ($U_{f,sys} = 0.8$, RR = 0.7).

Figure 8.11 shows the effect of changing I_{stack} on the stack inlet and outlet molar composition, .

It is important to specify that the absence of N_2 in the inlet and outlet composition is a result of the the CPOX air blower being turned off, since the oxygen provided by the AGR blower is sufficient to ensure that the (partial) external reforming process takes place.

Figure 8.11 displays that, for all the I_{stack} values, the H_2 concentration at the inlet is higher than that at the outlet. The opposite is true for H_2O. This demonstrates that in the stack, hydrogen is oxidized with the oxygen coming from the cathode side, producing H_2O (and power). Moreover, at the stack outlet there is no CH_4, showing that the methane entering the stack is reformed internally, consuming H_2O and producing CO and H_2, according to the MSR reaction (5.5). The presence of CO_2 in the inlet composition is a result of the fact that part of the outlet composition (containing CO_2 because of the WGS reaction (5.6)), is reintroduced in the system through the AGR blower. A decrease of 50-60/% in the inlet and outlet composition of all species is observed for a stack current of 12 A.

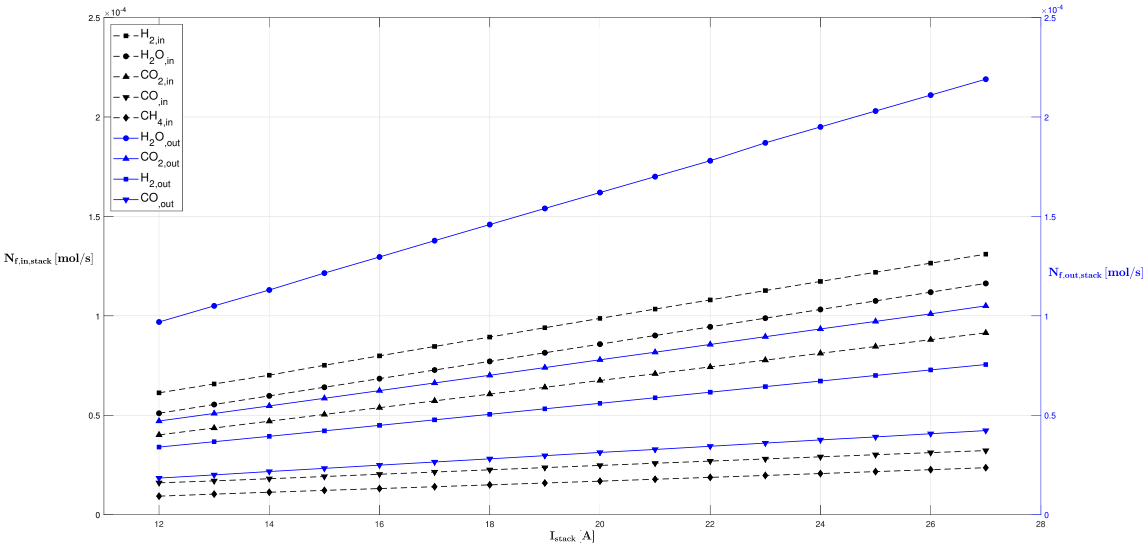

Figure 8.11: Influence of stack current on the fuel molar flow at the stack inlet and outlet ($U_{f,sys} = 0.8$, RR = 0.7).

The influence of the stack current on the system (η_{sys}) and stack (η_{stack}) efficiency is shown in Figure 8.12. These are estimated considering the net electric power produced by the system $P_{\text{net,sys}}$ and the electric power produced solely by the stack P_{stack}:

$$\eta_{\text{sys}} = \frac{P_{\text{net,sys}}}{LHV_{CH_4} \cdot N_{CH_4}} = \frac{P_{\text{stack}} - P_{\text{anc}}}{LHV_{CH_4} \cdot N_{CH_4}} \tag{8.5}$$

$$\eta_{\text{stack}} = \frac{P_{\text{stack}}}{LHV_{CH_4} \cdot N_{CH_4}} \tag{8.6}$$

Where $P_{\text{net,sys}}$ is obtained by subtracting the power required for the ancillary devices from P_{stack}.The term N_{CH_4} represents the methane flow that is electrochemically oxidised in the fuel cell [mol/s] and LHV represents the methane lower heating value [J/mol]. The highest efficiency is obtained for the lower value of the stack current, corresponding to the higher cell voltage. While the highest system efficiency is obtained when $I_{\text{stack}} = 12\,A$, corresponding to the operation where the power requirement from the ancillary devices is the lowest. A stack and system efficiency of 63 % and 55 % respectively is obtained when the stack current value is 12 A.

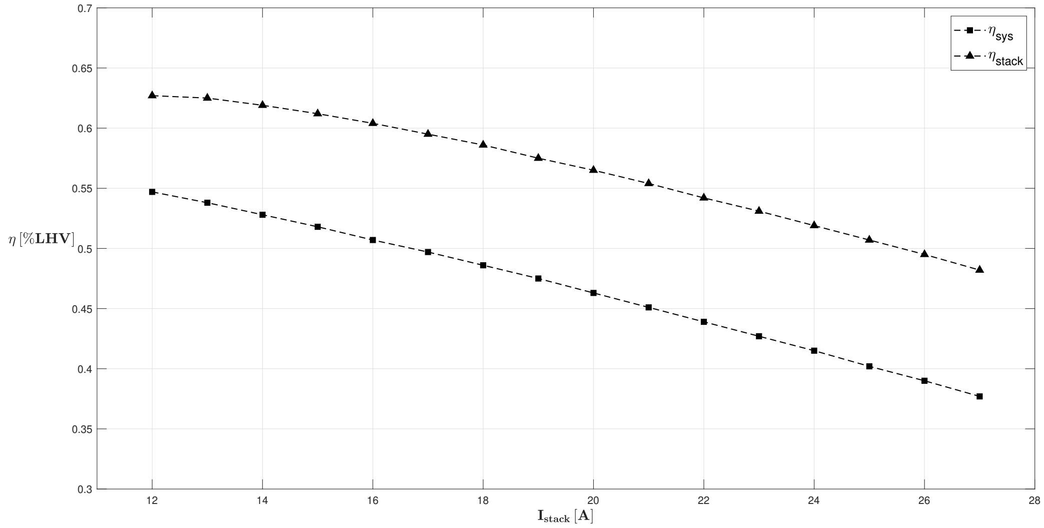

Figure 8.12: System and stack efficiency for different I values ($U_{f,sys} = 0.8$, RR = 0.7).

8.2 Influence of System Fuel Utilization

The influence of the system fuel utilization on the SOFC system performance is studied by varying the value of $U_{f,sys}$ from 0.7 to 0.9. The anode recirculating ratio changes with the system fuel utilization (from 0.8 to 0.6 c.a.) to keep the O/C ratio constant and equal to the set value and to ensure that no CPOX air is needed (i.e. the CPOX air blower is turned off). The stack current is also kept constant at 27 A by changing the amount of methane feeding the system. Finally, the air control on the PEN temperature is active thus the PEN temperature is kept constant at its nominal value.

Figure 8.14 shows the stack power curve for different values of $U_{f,sys}$ as well as the power required from the ancillary devices (i.e. cathode and AGR blower). The decrease of the stack power for higher fuel utilization is a result of the drop of the cell voltage (see Figure 8.13) which reaches a value below the lower limit suggested by the manufacture (i.e. 0.6 V) for values of $U_{f,sys}$ higher than 0.85. However, when working at lower stack current (i.e. 15 A), higher cell voltage values are achievable for the same $U_{f,sys}$. The cell voltage reduces from 0.82 V to 0.76 V at $I_{stack} = 15\,A$ by increasing the system fuel utilization from 0.7 to 0.9. This is well above the lower cell voltage limit.

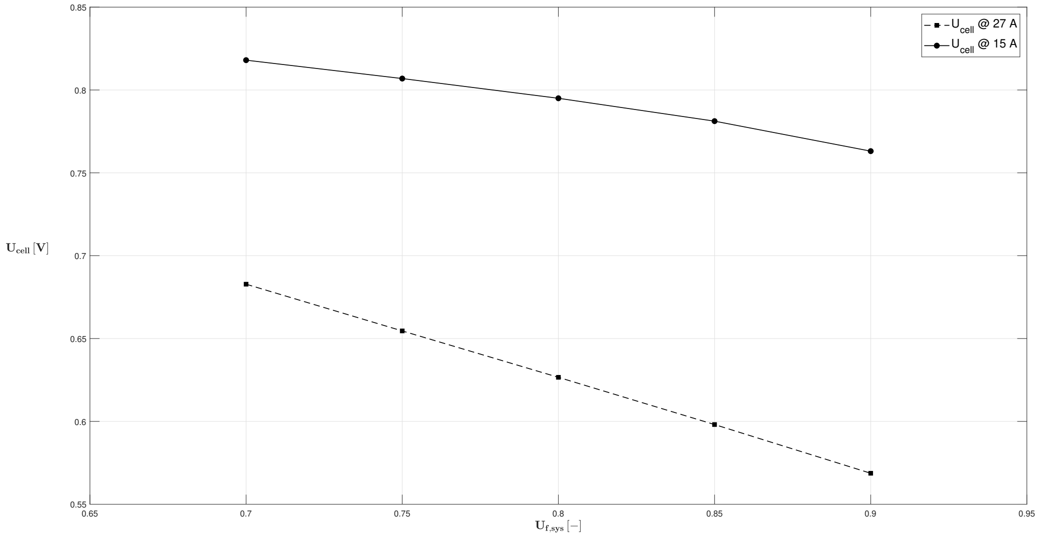

Figure 8.13: SOFC stack voltage for different $U_{f,sys}$

As shown in Figure 8.14, the power required by the cathode air blower does not change significantly, demonstrating a relatively small influence of $U_{f,sys}$ on the PEN temperature. On the other hand, when increasing the system fuel utilization, the AGR blower power significantly decreases, going from 160 W for $U_{f,sys}$= 0.7 to 50 W for a value of $U_{f,sys}$ =0.9. This is mainly due to the necessity of decreasing the anode recirculating ratio for higher $U_{f,sys}$ to keep the O/C ratio constant and to ensure that the CPOX air blower stays turned off. Figure D.1 in Appendix D shows the corresponding power curves for $I_{stack} = 15\,A$.

Figure 8.15 shows the power percentage required by the ancillaries of the total stack power. The maximum power requirement is obtained for the lower value of $U_{f,sys}$, with a total requirement of 25% the total power. This is a result of the higher power needed by the AGR blower for lower $U_{f,sys}$. The amount of power required by the cathode air blower remains mostly constant, as already shown in Figure 8.14. The net power produce by the stack increases from 76% to 82%, when $U_{f,sys}$ is increased from 0.7 to 0.9.

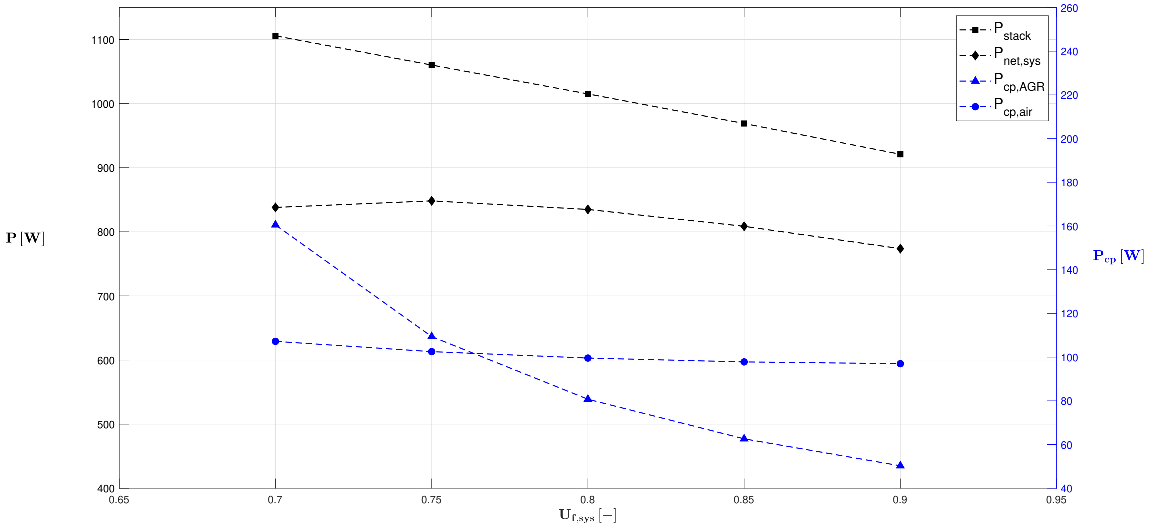

Figure 8.14: Influence of system fuel utilization on the components power requirement @ I_{stack} = 27A.

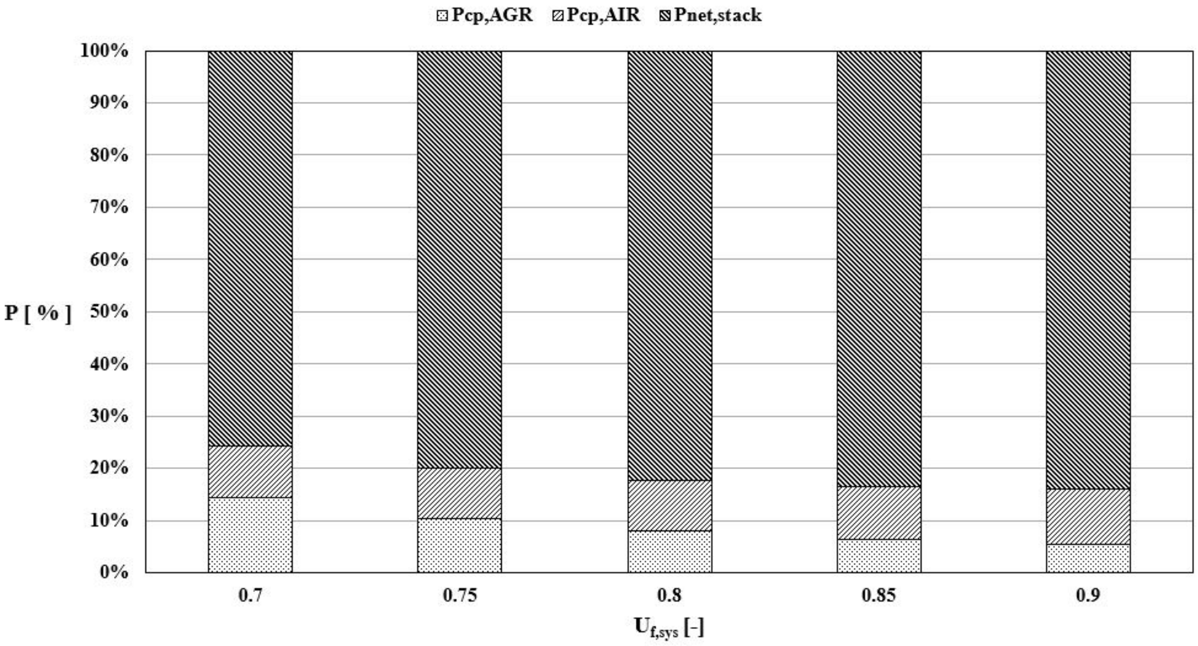

Figure 8.15: Percentage of the power requested by the ancillary devices for different $U_{f,sys}$ @ I_{stack} = 27A.

Figure 8.16 shows the effect of $U_{f,sys}$ on the methane and air mass flow. As seen in the power curves, the amount of cathode air does not change significantly, with a reduction of almost 9% for $U_{f,sys} = 0.9$ (compared to $U_{f,sys} = 0.7$).The $\dot{m}_{CH_4}$ decreases considerably reaching a value 22% lower for $U_{f,sys} = 0.9$ than for $U_{f,sys} = 0.7$. This reduction is a result of the need of keeping the stack current constant at 27 A. Similar reductions in the mass flows are obtained for I_{stack} = 15 A, as shown in Figure D.2.

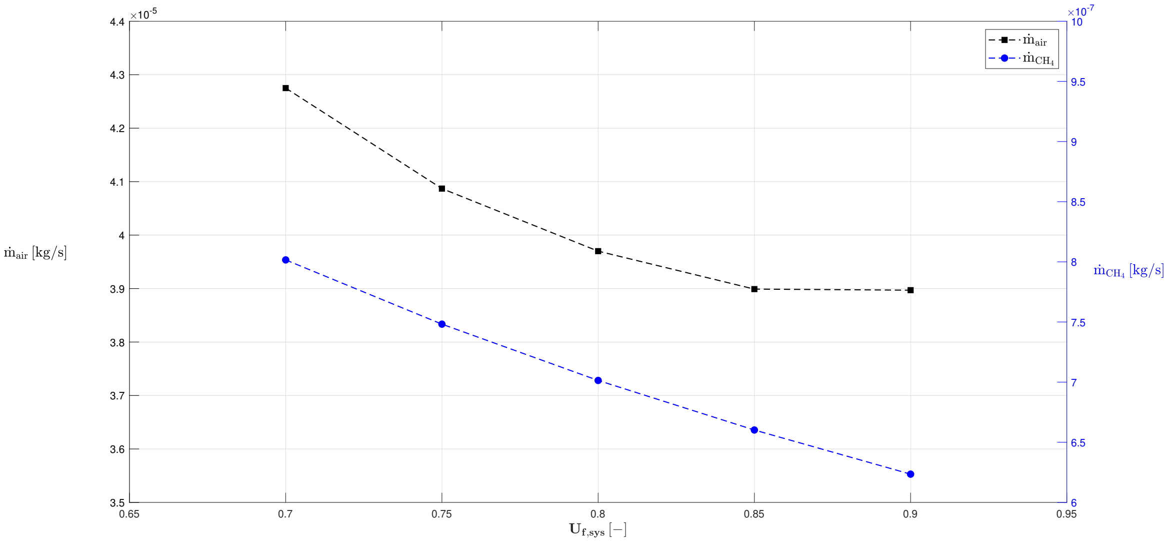

Figure 8.16: Methane and cathode air mass flow for different values of $U_{f,sys}$ @ I_{stack} = 27A. The flows refer to single cell operation.

The influence of U_{f_sys} on the temperature of the fuel and air entering the stack and the heating medium leaving the heat exchangers is shown in Figure 8.17. A relatively small reduction of 10% and 12% respectively, for $T_{f,in}$ and $T_{a,in}$ occurs when increasing $U_{f,sys}$ from 0.7 to 0.9. $T_{f,Hex,out}$ does not change significantly with the system fuel utilization. Since the reduction of the cathode air flow is relatively small, the drop in the air temperature cannot be attributed to the heat exchanger design as for the case of different I_{stack}. It is a result of the significant reduction of the afterburner outlet temperature (as shown in Figure 8.18), representing the hot fluid in the air heat exchanger (see Figure 3.1). The burner temperature drastically reduces for higher system fuel utilization values, reaching a temperature difference of almost 200 K between the case with $U_{f,sys}$ = 0.7 and that with $U_{f,sys}$ = 0.9. This is related to the lower amount of fuel available at the afterburner inlet, as shown in Figure 8.16 and 8.21. No significant change in the afterburner outlet composition is observed, as shown in Figure 8.19.

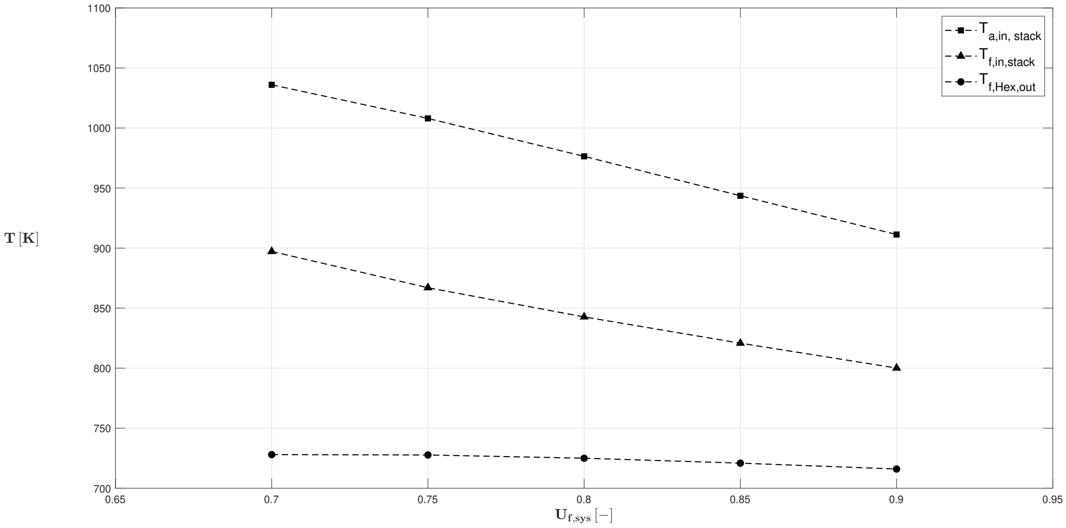

Figure 8.17: Influence of the system fuel utilization on the air and fuel stack inlet temperature @ I_{stack} = 27A.

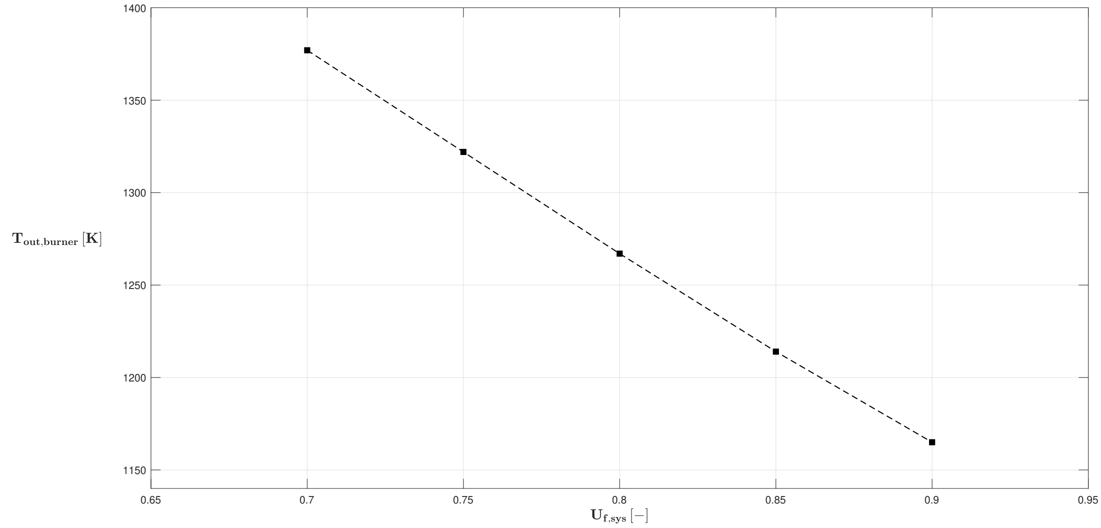

Figure 8.18: Influence of the system fuel utilization on the outlet temperature of the afterburner @ I_{stack} = 27A.

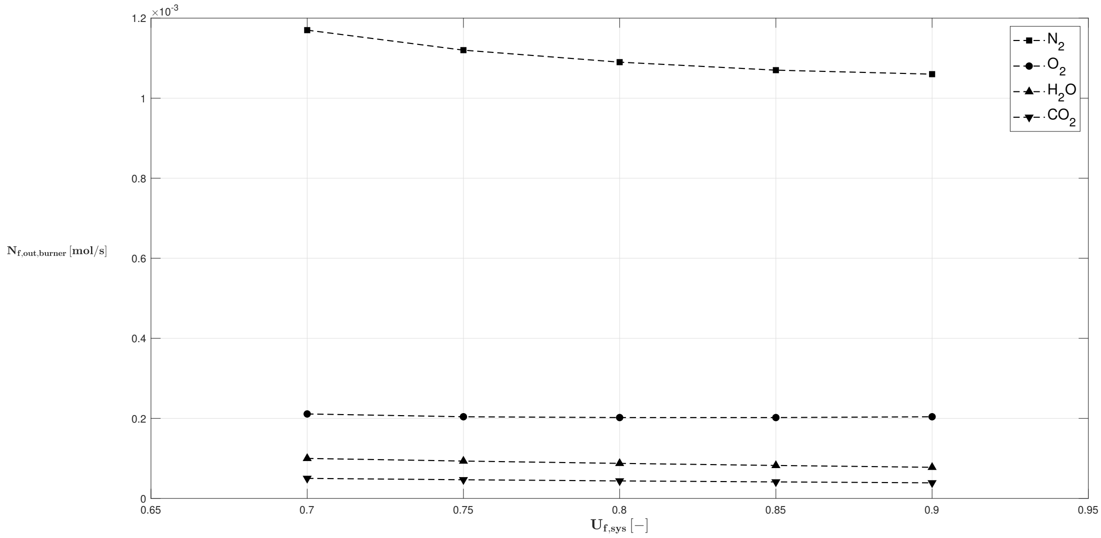

Figure 8.19: Influence of system fuel utilization on the molar flow at the afterburner outlet @ I_{stack} = 27A.

Figures 8.20 and 8.21 show the influence of $U_{f,sys}$ on the stack inlet and outlet fuel composition. The differences between inlet and outlet are the same as for the case with different stack currents.

The hydrogen content at the CPOX reformer outlet (i.e. stack inlet) decreases significantly with the fuel utilization with a total reduction of 75 % for $U_{f,sys}$ = 0.9. The same occurs for CO with a total reduction of more than 85% when the system fuel utilization is 0.9. While for CO_2 and H_2O, the increase of $U_{f,sys}$ to 0.9, produces a reduction to half the value for $U_{f,sys}$ = 0.7. The methane flow increases for higher system fuel utilization.

Increasing $U_{f,sys}$ results in a significant decrease of CO_2 and CO in the stack outlet composition, with a total reduction of 86% for both species when $U_{f,sys}$ is 0.9. H_2O and H_2 reduces by 40% for $U_{f,sys}$ = 0.9. Similar reductions can be observed for I_{stack} = 15 A, as shown in Figures D.6 and D.7 .

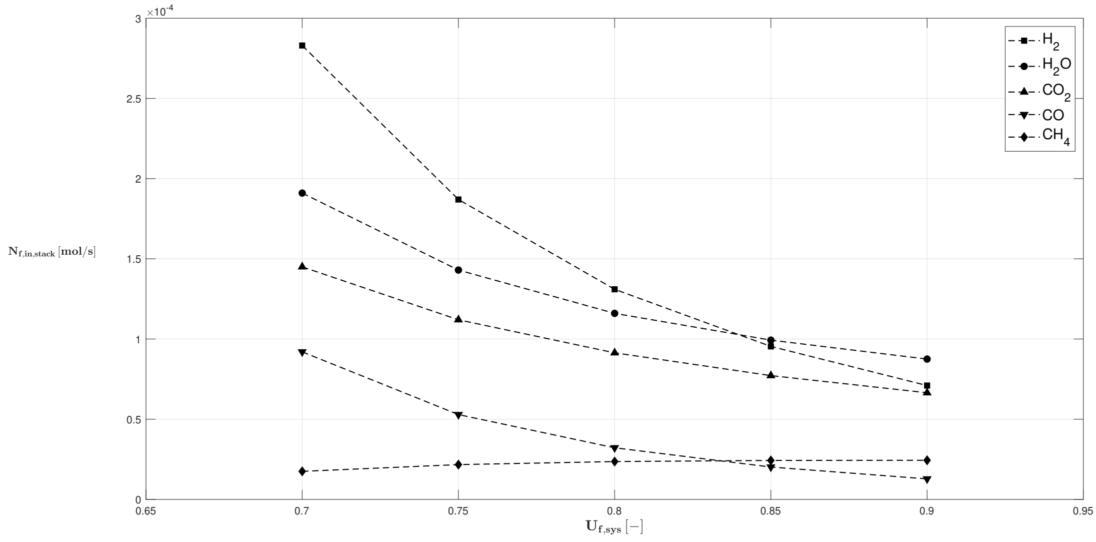

Figure 8.20: Influence of system fuel utilization on the fuel molar flow at the stack inlet @ I_{stack} = 27A.

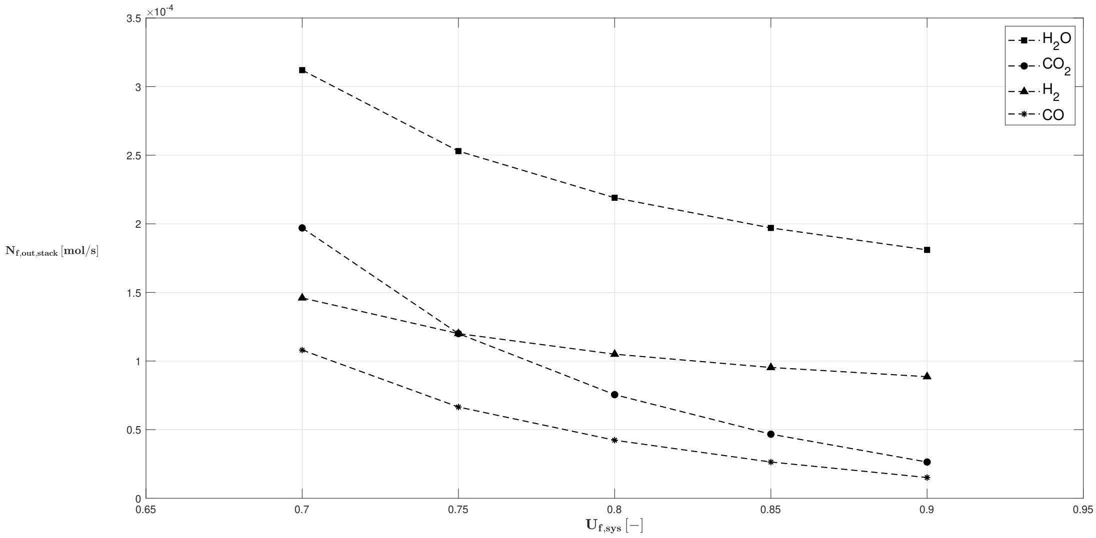

Figure 8.21: Influence of system fuel utilization on the fuel molar flow at the stack outlet @ I_{stack} = 27A.

The influence of $U_{f,sys}$ on the stack and system efficiency is shown in Figure 8.22. At $I_{stack} = 27\,A$, the highest system and stack efficiency is achieved for the highest $U_{f,sys}$. For $U_{f,sys} = 0.9$, $\eta_{|sys} = 0.39$ (representing an increase of 20% compared to $U_{f,sys} = 0.7$) and $\eta_{|stack} = 0.49$. However at $I_{stack} = 27A$, the cell voltage drops below the manufacture lower limit for $U_{f,sys}$ higher than 0.85.

At $I_{stack} = 15\,A$, both stack and system efficiency increases considerably. $\eta_{|stack}$ increases from 0.55 to 0.66 by increasing $U_{f,sys}$. While the $\eta_{|sys}$ reaches a value of 0.58 for $U_{f,sys} = 0.9$.

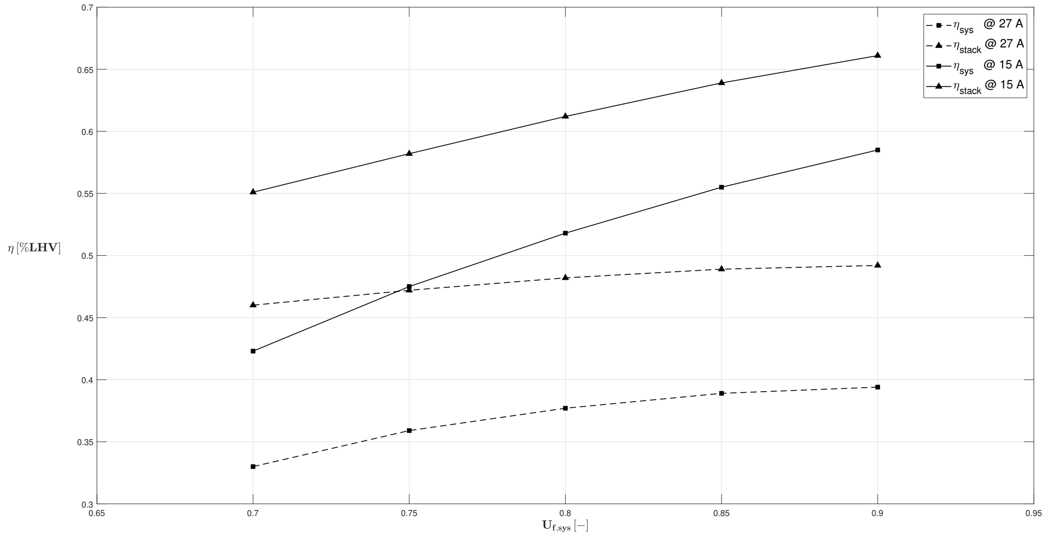

Figure 8.22: System and stack efficiency for different $U_{f,sys}$ values.

8.3 Influence of Anode Recirculating Ratio

The influence of the anode recirculating ratio on the system performance has been studied. The model outputs were evaluated for constant $U_{f,sys}$,O/C ratio and stack current, equals to their respective nominal values. Consequently, by changing the RR, the fraction of CPOX air needed changes, according to relation (4.14). The PEN temperature control is active, thus the maximum PEN temperature will remain constant and equal to its nominal value.

Figure 8.24 shows the power curves of the stack as well as the ancillary devices as function of RR for $I_{stack} = 27\,A$. Since the stack current is kept constant, the power produced by the stack is strictly related to the cell voltage U_{Cell} (see Figure 8.23) . The U_{Cell} decreases slightly by increasing RR from 0 to 0.6, after which it is possible to see a relatively sharp increase of the cell voltage. However, the change in the U_{Cell} is limited in the range of 0.62-0.64 V. When working at lower current (i.e. 15 A), the values of the cell voltage are considerably higher. At $I_{stack} = 15\,A$, U_{Cell} increases from 0.76 V to 0.79 V by increasing RR.

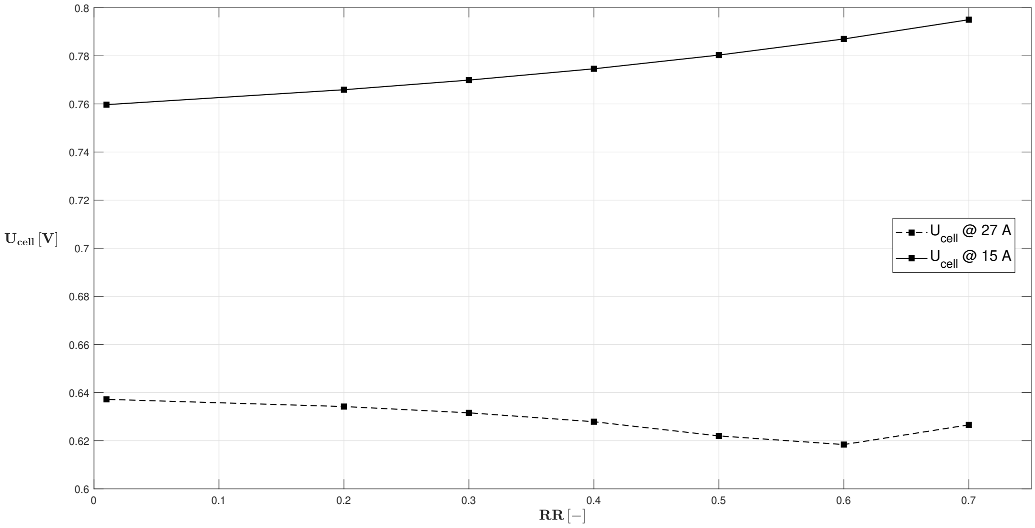

Figure 8.23: SOFC stack voltage for different RR

Figure 8.24 shows the relation between the AGR blower and the CPOX blower. RR = 0 and RR = 0.7 represents the two extreme cases. For RR = 0, the AGR blower is turned off while the CPOX blower requires the maximum power. The opposite is true for RR = 0.7. The power required by the cathode air blower, decreases when increasing the anode recirculating ratio, since less cathode air is needed for cooling purposes, as shown in Figure 8.26.

Figure 8.25 shows the power percentage required for the ancillaries as a percentage out of the total stack power for different values of RR. The $P_{net,stack}$ remains constant and equal to 75%, for value of RR between 0 and 0.3. It increases for higher value of RR, reaching a maximum of 82% at RR = 0.7. Figure 8.25 also shows that the cathode air blower has the highest power demand of the three ancillary devices. The CPOX air blower consumes the least amount of power.

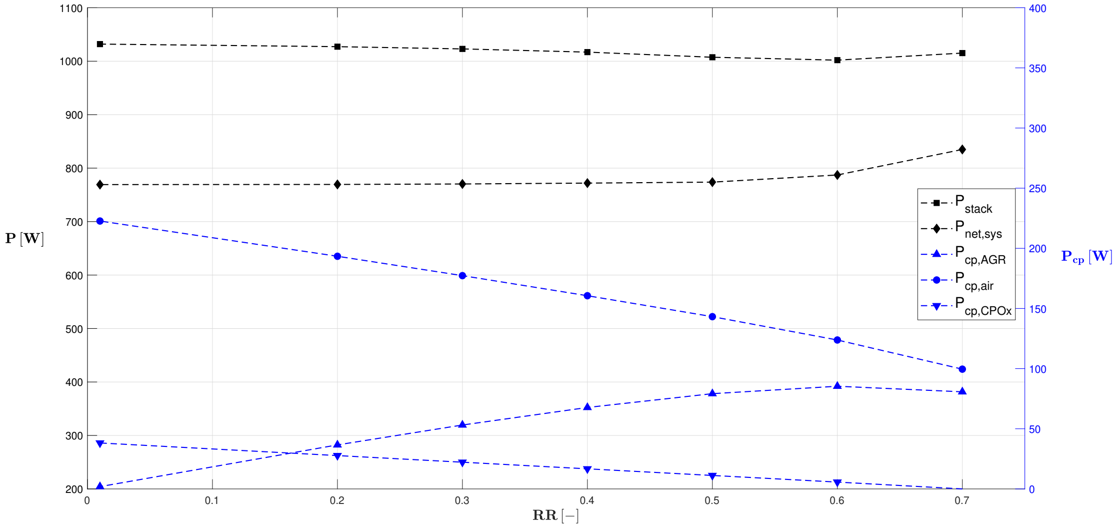

Figure 8.24: Influence of anode recirculating ratio on the components power requirement ($U_{f,sys=0.8}$, $I_{stack} = 27\,A$). The respective figure for $I_{stack} = 15\,A$ is reported in Appendix E.

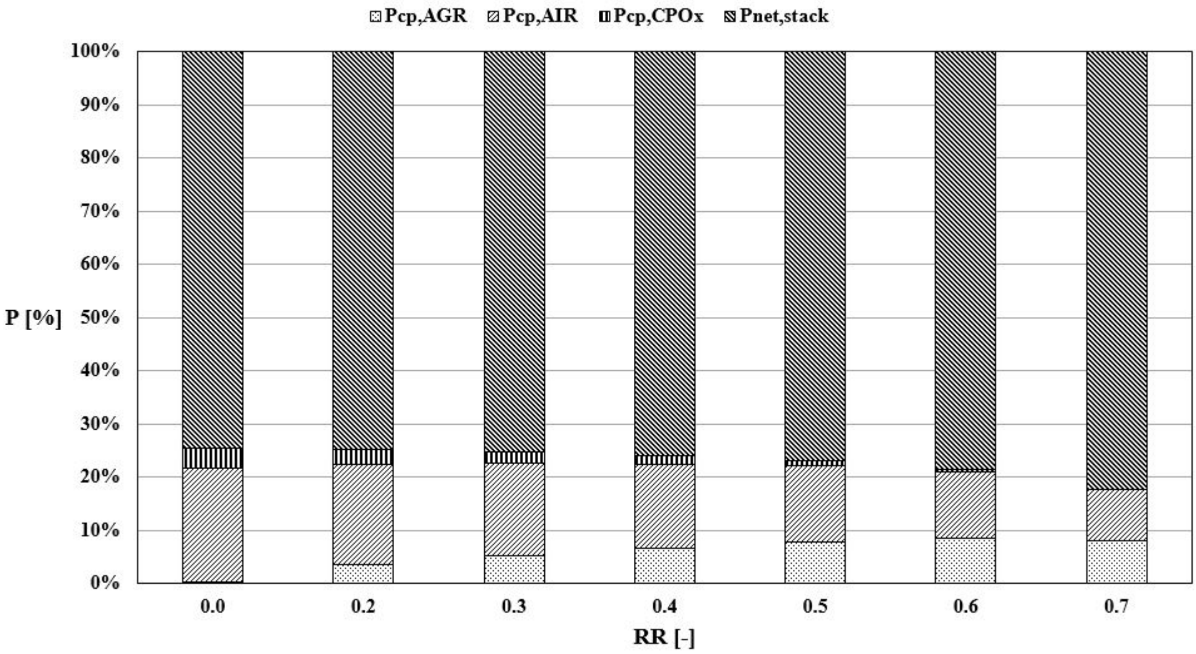

Figure 8.25: Percentage of the power requested by the ancillary devices for different RR. ($U_{f,sys=0.8}$, $I_{stack} = 27\,A$).

Figure 8.26 shows that the amount of cathode air decreases by increasing the RR. The PEN temperature decreases when the recirculating ratio increases, requiring less air to cool down the stack.

The CPOX air need to be increased to keep the O/C ratio constant when RR is reduced. The amount of CH_4 increases when the RR is decreased as more fuel is needed to keep the system fuel utilization constant.

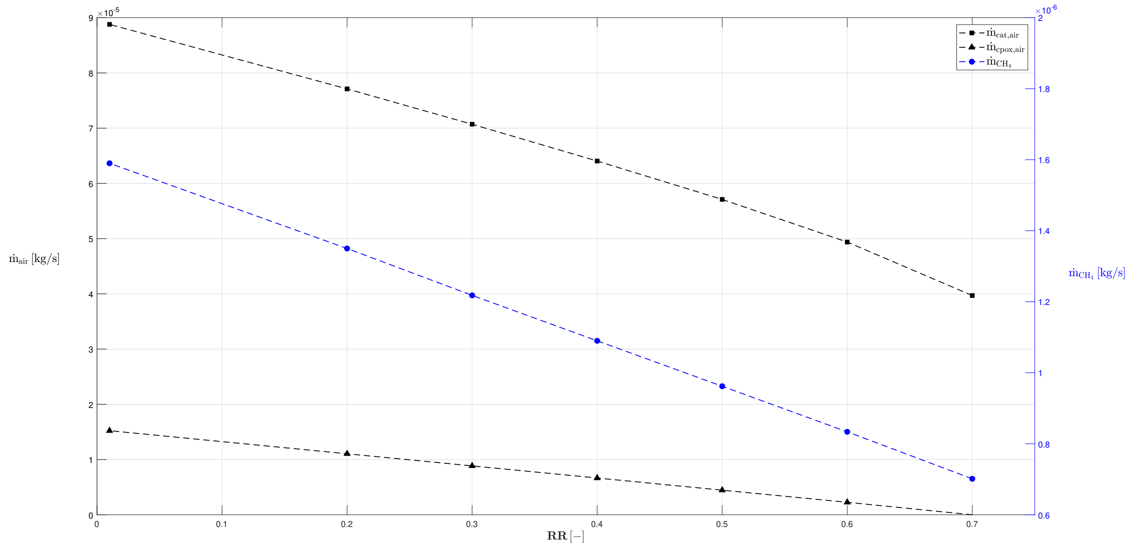

Figure 8.26: Anode,cathode and CPOX mass flow for different values of RR. The flows refer to single cell operation ($U_{f,sys=0.8}, I_{stack} = 27\,A$). The respective figure for $I_{stack} = 15\,A$ is reported in Appendix E.

Figure 8.27 shows the effect of RR on the air and fuel flow temperatures. The temperature $T_{f,in}$ reduces significantly with the RR, from 1750 K to 843 K. This is a result of the change of the CPOX reformer inlet composition (characterised by only CH_4, O_2 and N_2 for RR = 0). The composition is highly dependent on both CPOX air and recirculated flow. The outlet temperature of the adiabatic mixer increases significantly by increasing the recirculation ratio, from 380 K (at RR = 0) to almost 1100 K (at RR = 0.7). This significant increase is a result of the higher RR, translating in higher amount of hot fluid recirculating in the system.

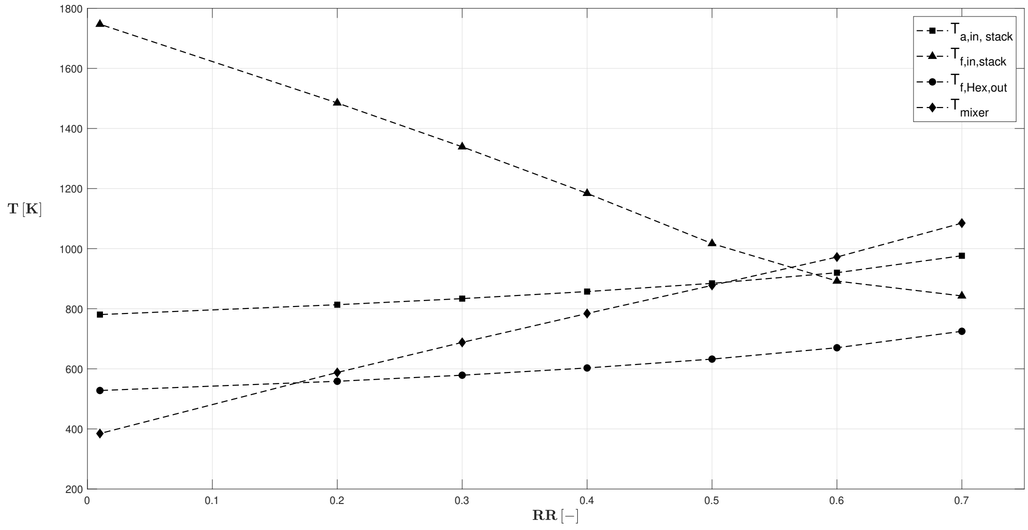

Figure 8.27: Influence of the anode recirculating ratio on the air and fuel stack inlet temperature ($U_{f,sys=0.8}, I_{stack} = 27\,A$). The respective figure for $I_{stack} = 15\,A$ is reported in Appendix E.

Figures 8.28 and 8.29 show the influence of RR on the stack inlet and outlet fuel composition. Compared to the other cases (i.e. different $U_{f,sys}$ and I_{stack}), an additional species is present in the stack inlet and outlet composition, namely N_2. The latter does not react in the SOFC stack, as can be observed by comparing both figures, as the N_2 composition at the inlet and at the outlet remains the same. Regrading the other species, no significant changes occur at the stack inlet except for the amount of CO_2 which increases by 75% for RR = 0.7 and CO which reduces by 60% for RR = 0.7.

The stack outlet composition, of H_2 and CO increase with 70% for RR = 0.7.

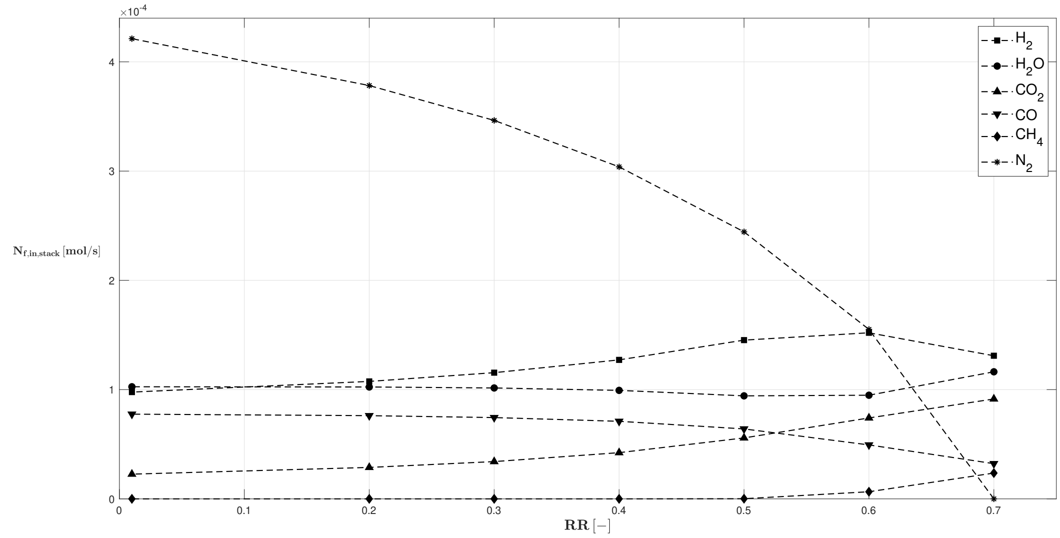

Figure 8.28: Influence of anode recirculating ratio on the fuel molar flow at the stack inlet ($U_{f,sys=0.8}$, I_{stack} = 27 A). The respective figure for I_{stack} = 15 A is reported in Appendix E.

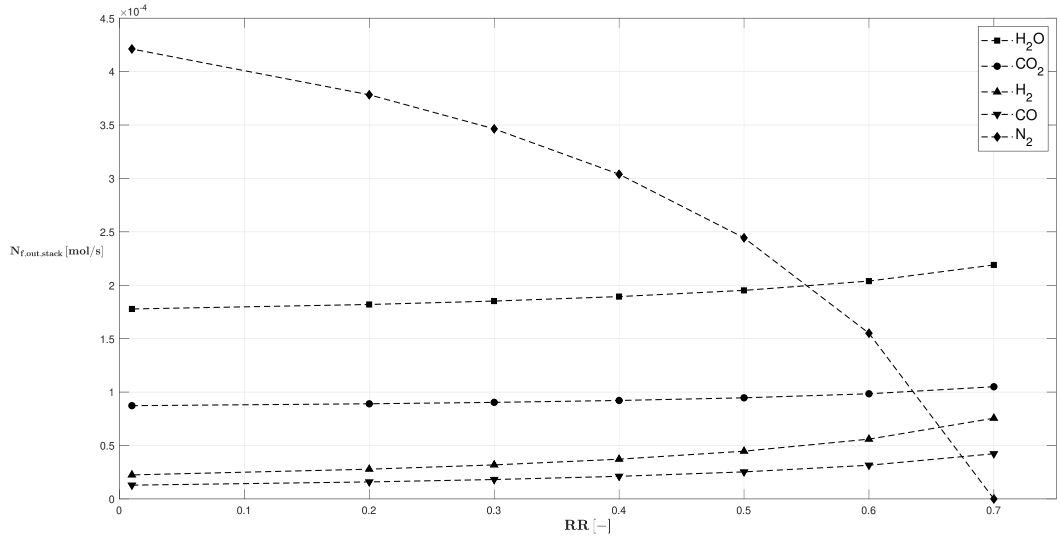

Figure 8.29: Influence of anode recirculating ratio on the fuel molar flow at the stack outlet ($U_{f,sys=0.8}$, I_{stack} = 27 A). The respective figure for I_{stack} = 15 A is reported in Appendix E.

The outlet composition of the afterburner is dominated by N_2 and O_2, which decrease for higher RR as less CPOX air is introduced in the system. H_2O and CO_2, reduce by 56% at RR = 0.7.

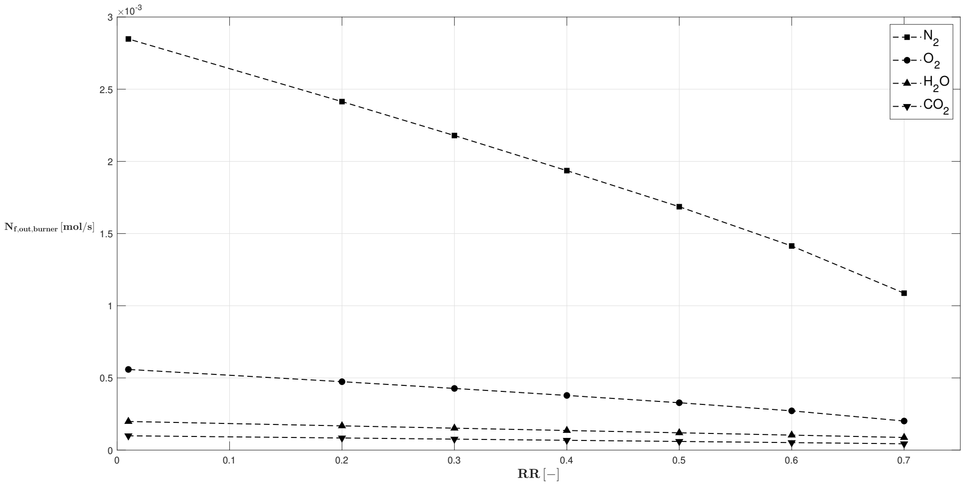

Figure 8.30: Influence of anode recirculating ratio on the molar flow at the afterburner outlet ($U_{f,sys=0.8}$, I_{stack} = 27 A). The respective figure for I_{stack} = 15 A is reported in Appendix E.

The effect of RR on the system and stack efficiency is shown in Figure 8.31. The highest stack efficiency is achieved when the AGR blower is turned off, with a value of $\eta_{stack} = 0.49$. For higher anode recirculating ratios, η_{stack} slightly decreases to 0.48 at the nominal operational point (i.e. RR=0.7).

The situation is reversed for the system efficiency, with the highest value of η_{sys} when the CPOX air blower is turned off, i.e. nominal operation. Then the system efficiency reduces from 38% to 34% when RR is decreased from 0.7 to 0.

At I_{stack} = 15 A, both stack and system efficiency values are significantly higher. The stack efficiency reaches its maximum when the CPOX blower is turned off, with a value of $\eta_{stack} = 0.61$. The system efficiency (at 15 A) is 0.52 for RR = 0.7 and reduced to 0.42 when the AGR blower is turned off (RR = 0).

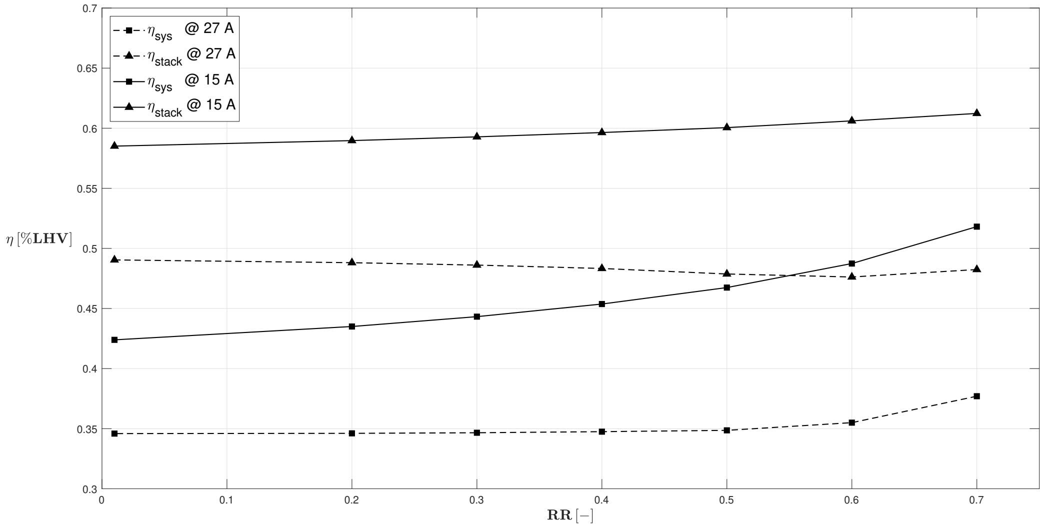

Figure 8.31: System and stack efficiency for different RR values.

Chapter 9

Load Transients Results and Discussion

The developed model is able to simulate the system response to load changes. These are simulated by varying the current in the SOFC stack according to the new power requirement, as explained in Section 6.2. During load transients, the system fuel utilization as well as the O/C ratio and the RR are kept constant by changing the methane flow entering the system. Table 9.1 summarises the simulation scenarios.

Table 9.1: Load transients simulation scenarios

Simulation	$\mathbf{T_{Target}}$ **[K]**	$\mathbf{P_{Cell,Target}}$ **[W]**	$\mathbf{I_{Stack,Target}}$ **[V]**	**Current ramp [A/min]**
Simulation 1	1123.15	16.92 → 15.86 → 16.92	27 → 23 → 27	Step
Simulation 2	1123.15	16.92 → 15.86 → 16.92	27 → 23 → 27	0.25
Simulation 3	1123.15	16.92 → 15.86 → 16.92	27 → 23 → 27	0.16
Simulation 4	1123.15	16.92 → 15.86 → 16.92	27 → 23 → 27	0.05

9.1 Step/Ramp comparison - Feed-back Control

Figures 9.1, 9.2,9.3 and 9.4 show the results obtained when the current is changed from the nominal value (27 A) to 23 A and then back to 27 A. When the current is changed, the amount of methane entering the system changes to keep the system fuel utilization constant (see relation (8.1)).

Figure 9.1 shows how the stack PEN temperature is affected by the current change. Simulation 1 and 2 are compared in the following figures. In Simulation 1, the current is stepped to the new values (solid line), while in Simulation 2, the current is ramped (dashed line). The stack manufacturer suggests a current ramp not faster than 2 A/min in order to preserve the stack integrity [74]. A current ramp of 0.25 A/min has been chosen in accordance to D'Andrea et al. [75] which demonstrated that current ramp rates higher than 0.30 A/min lead to excessive stack overheating.

Figure 9.1 shows that the cathode air control system slowly succeeds in restoring the PEN temperature, after the step change. After 8000 s (2 hrs c.a.) the model stabilises and the PEN temperature returns to it's nominal value. During the first step (down), the PEN temperature rapidly decreases to 1097 K, corresponding to a temperature gradient of 26 K. The situation reverses when the current is stepped back to its nominal value. The temperature rapidly exceeds the maximum limit imposed by the manufacturer (1133 K) by 18 K. Ramping the load change results in a reduction of the temperature over and undershoot with 10 K. The maximum temperature reached in this case is 1141 K, exceeding the manufacture limit by 8 K. The speed of the system response to the load transient is not significantly affected when the current is ramped.

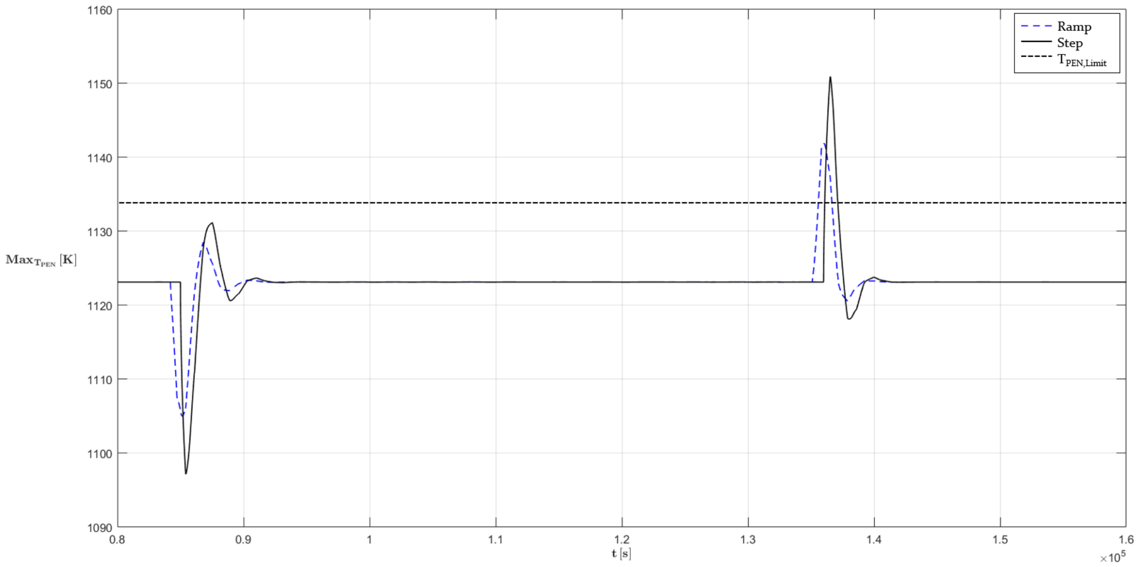

Figure 9.1: Simulated PEN temperature during load transients.

Figures 9.2 and 9.3 show the change of P_{Cell} and U_{Cell} during Simulation 1 and 2. When the step change is applied, the power produced by the cell, rapidly decreases to a value lower than the target, causing an undershoot of almost 2.5 W. The target is reached after 8000 s.

The situation reverses when the current is stepped back to its nominal value, where an overshoot of the same magnitude is observed. The system response improves when the current is ramped instead. The power undershoot and overshoot reduce but the speed of the system response does not change significantly. For the cell voltage, the results are similar to the cell power. Stepping the current produces a relatively large overshoot and undershoot, of which magnitude reduces if the current is ramped. Figure 9.4 shows how the cathode air blower adjusts the air flow in order to restore the PEN temperature during load transients. The small steps in the air flow values are a result of the discretized PID controller used in the air loop control system. Thus, every 700 s the model gets an update of the current situation and reacts accordingly. Changing the type of controller to continuous might produce a better system response, but would increase the computational time substantially and impractically.

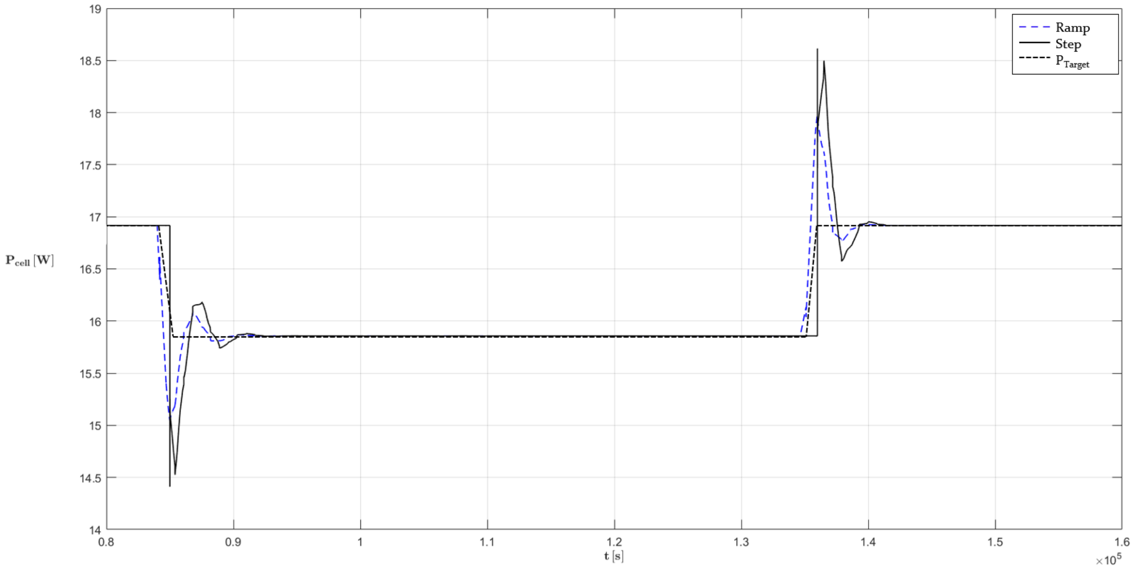

Figure 9.2: Simulated power produced by a single cell during load transients.

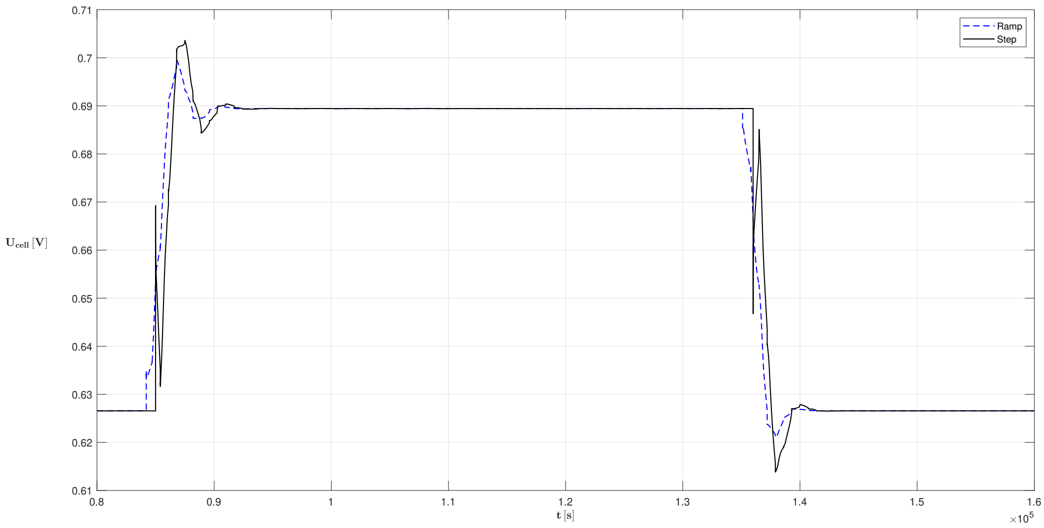

Figure 9.3: Simulated cell voltage during system load transients.

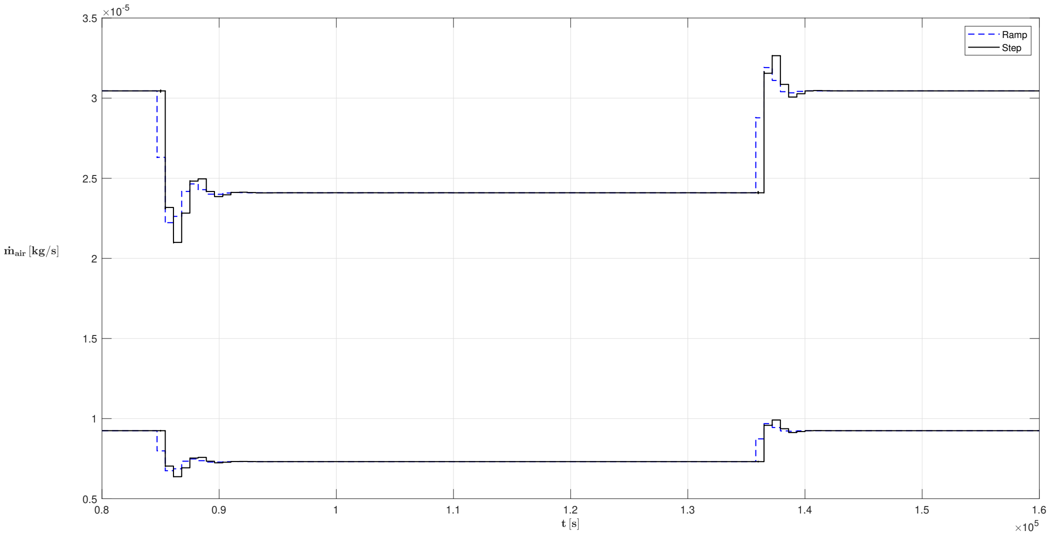

Figure 9.4: Air flow at the stack inlet during load transients.

9.2 Step/Ramp comparison - Feed-forward Control

The system response to dynamic loads changes when feed-forward control strategy is used, rather than feed-back control. The PID controller has been substituted with a look-up table with data provided by the steady state results (see Sec.8.1). By doing so, when the load change occurs, the system is fed directly with the right amount of air necessary to keep the maximum T_{PEN} below the limit imposed (see Figure 9.8). Figures 9.5, 9.6, 9.7 and 9.8 show the results obtained when a step and a ramp (with ramp values of 0.05 A/min) change occurs. By comparing Figure 9.5 with Figure 9.1 it is possible to see how, during a step change, the overshoot and undershoot reduces when feed-forward control is used. In particular, a maximum PEN temperature of 1137 K is reached for feed-forward control compared to 1151 K for feed-back control. The same occurs for the undershoot, with a temperature of 1110 K for feed-forward control and 1097 K for feed-back control. The magnitude of the temperature overshoot and undershoot reduces if a ramp change is applied instead.

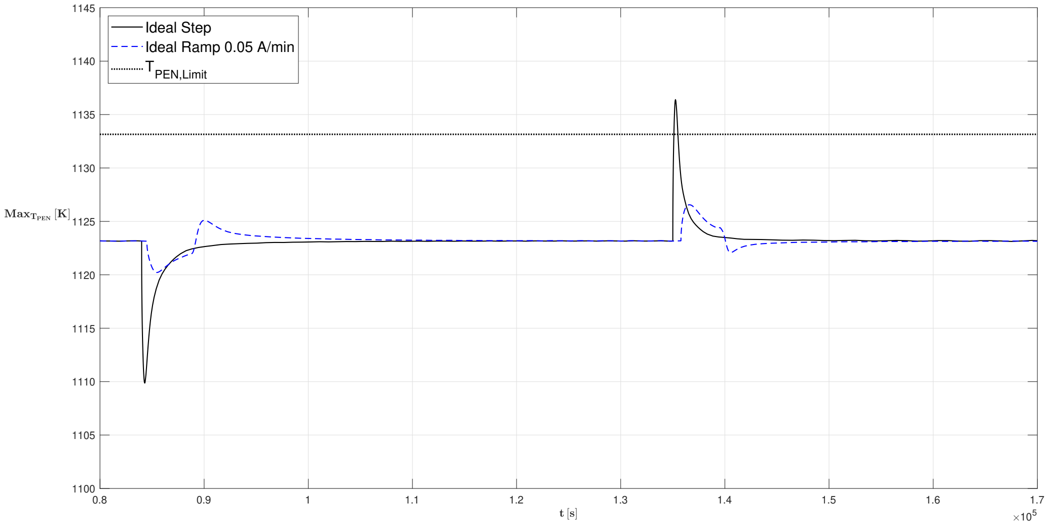

Figure 9.5: Simulated PEN temperature during load transients with feed-forward control.

Regarding P_{Cell} and U_{Cell}, a more uniform change occurs when feed-forward control is used but the speed of the system response does not change significantly. Moreover, the magnitude of the highest undershoot and overshoot of the cell power during a step change, is the same for feed-back and feed-forward control. On the other hand, U_{cell} overshoot and undershoot reduces considerably during a step change with feed-forward control.

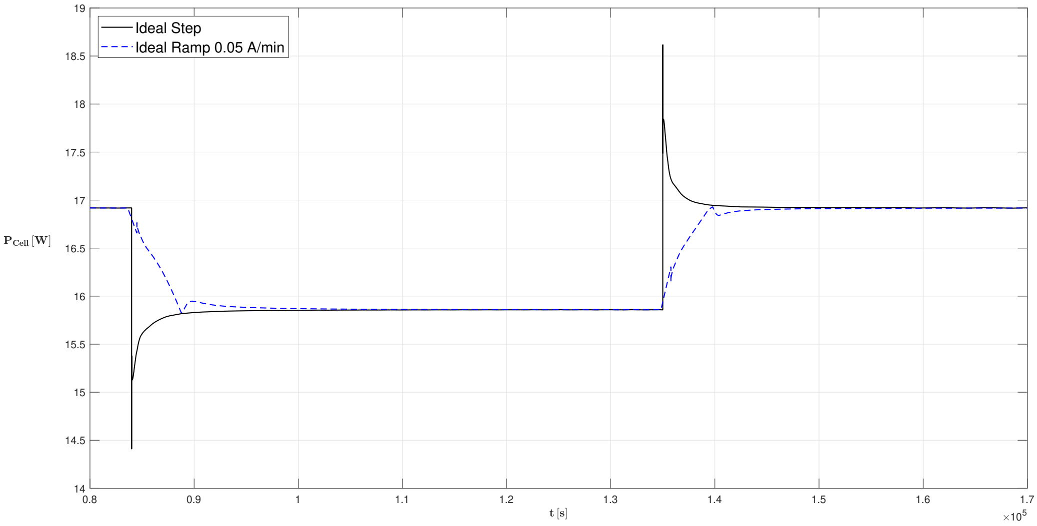

Figure 9.6: Simulated power produced by a single cell during load transients with feed-forward control.

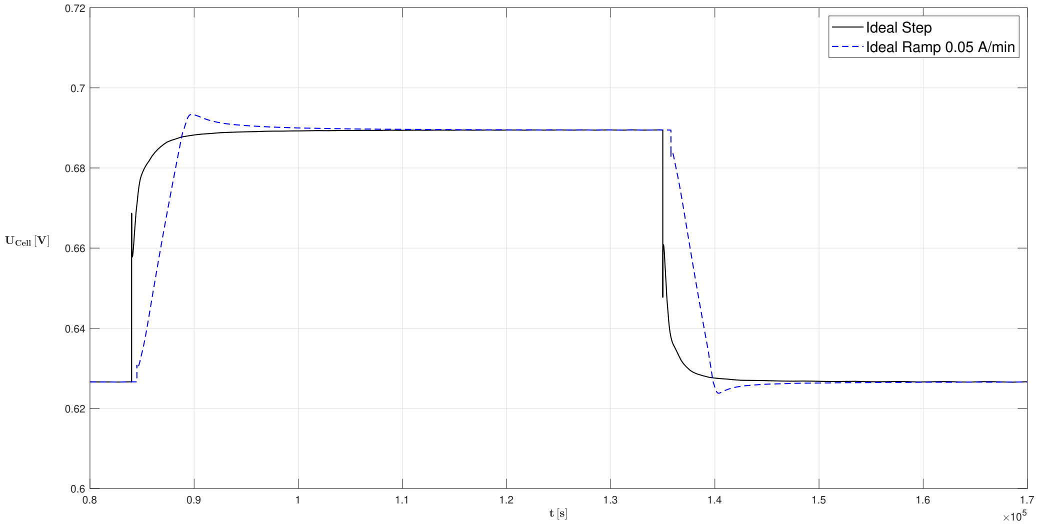

Figure 9.7: Simulated cell voltage during load transients with feed-forward control.

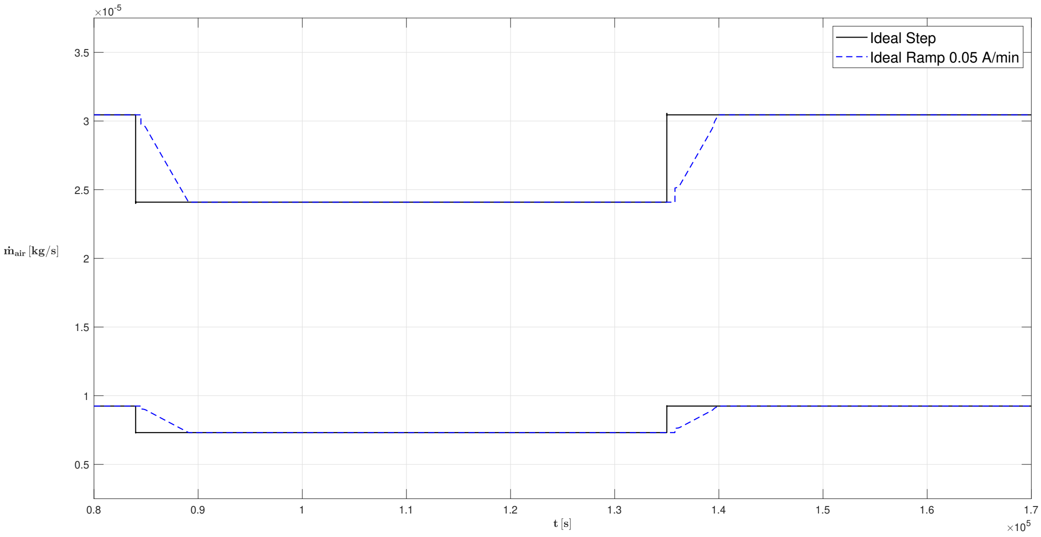

Figure 9.8: Air flow at the stack inlet during load transients with feed-forward control.

9.3 Influence of different ramp values - Feed-back Control

The effect of different current ramps on the system response to load transients may be observed by comparing the results from Simulations scenarios 2, 3 and 4 with a current ramp of 0.25, 0.16 and 0.05 A/min respectively. The results obtained are shown in the figures below.

Figures 9.9, shows the effect of the different ramps on the PEN operating temperature. The control system succeeds to restore the PEN temperature to its nominal value after almost 2 hrs for all simulations. However, for current ramp value of 0.25 and 0.16 A/min, during the ramp change from 23 to 27 A, the PEN temperature exceeds the upper limit imposed by the manufacture by respectively 8 and 5 K, representing a critical condition for the stack performance. By decreasing the current ramp to 0.05 A/min, a thermal safe operation is ensured with values of PEN temperature lower than the limit imposed. The speed of the system response does not change considerably for all the ramp values.

The effect of the different ramp values on the cell power and voltage is shown in Figures 9.10 and 9.11. As for the PEN temperature, also for $\mathrm{P_{Cell}}$ and $\mathrm{U_{Cell}}$, the undershoots and overshoots are reduced significantly when the current ramp is 0.05 A/min, with a more uniform system response to the imposed load changes.

Figures 9.12, shows how the cathode air flow is changed by the controller so to ensure a thermal safe operation. The undershoot and overshoot observed for the 0.25 A/min case is reduced to almost zero with current ramp of 0.05 A/min.

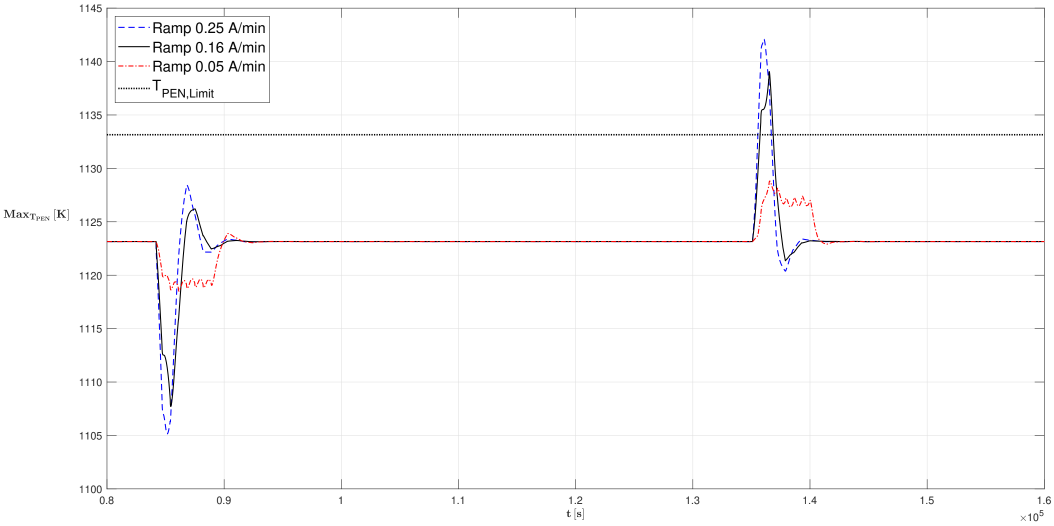

Figure 9.9: Simulated PEN temperature during load transients for different current ramp.

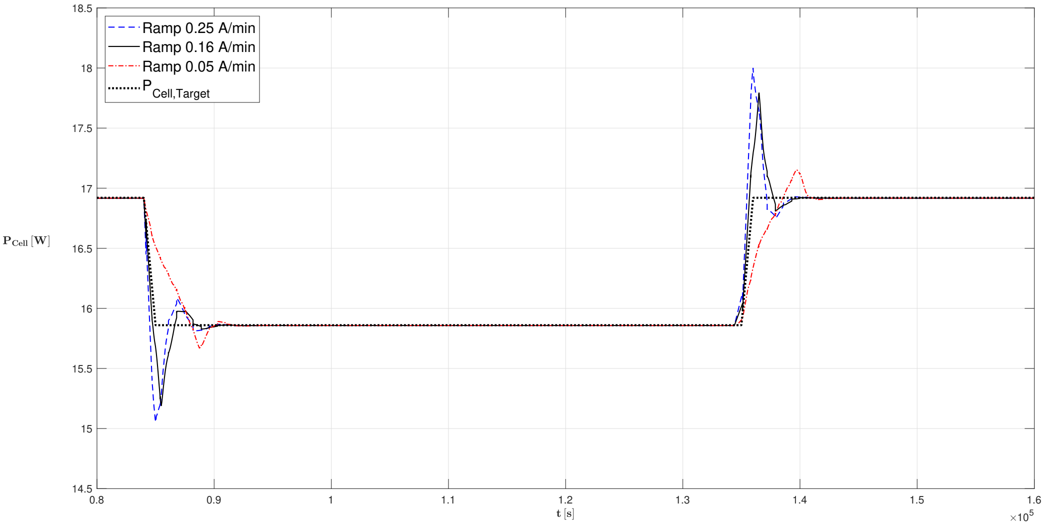

Figure 9.10: Simulated cell power during load transients for different current ramp.

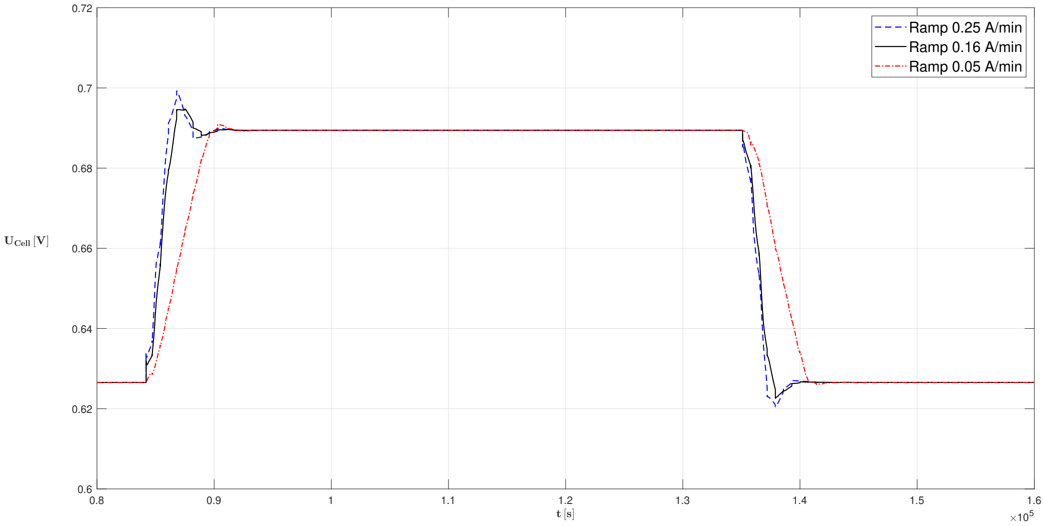

Figure 9.11: Simulated cell voltage during load transients for different current ramp.

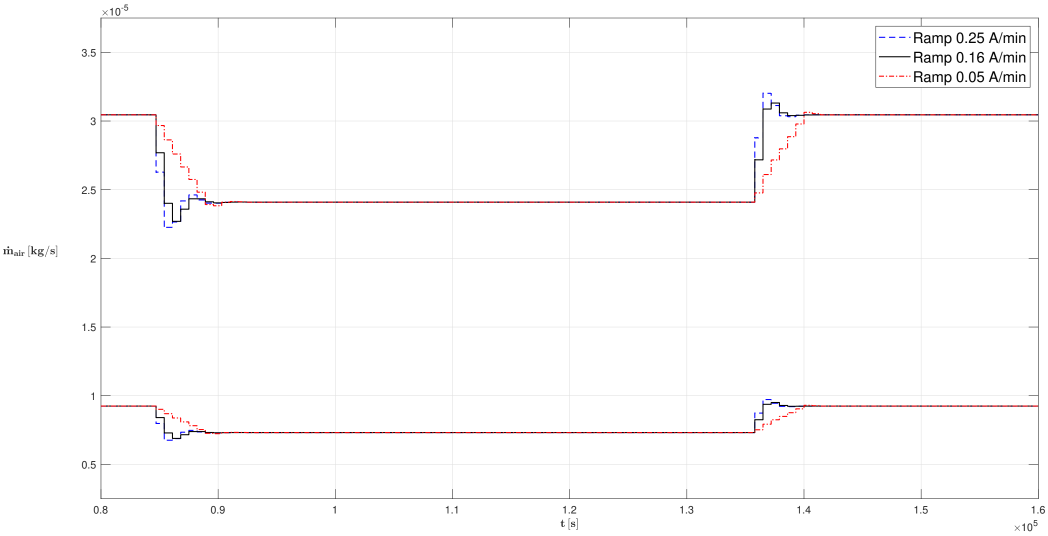

Figure 9.12: Simulated cathode air flow during load transients for different current ramp.

9.4 Influence of different ramp values - Feed-forward control

Figures 9.13, 9.14, 9.15 and 9.16 show the results obtained for different ramp values when feed-forward control is applied instead.

It is interesting to notice how the feed-forward control allows higher ramp values than feed-back control. Specifically, when feed-back control is applied, only a ramp value of 0.05 A/min was able to ensure thermal safe operation. While for feed-forward control, both 0.05 A/min and 0.16 A/min ensure that the maximum PEN temperature limit is not exceeded. Unfortunately, as for feed-back control, also for feed-forward control a ramp value of 0.25 A/min produces a temperature overshoot which exceeds the limit imposed by the manufacturer. This is mainly related to the inertia of the air flow heating process which produces a temperature overshoot and undershoot of the air entering the stack (see Figure F.5).

However, when comparing Figures 9.13 and 9.9, it is possible to see how the temperature overshoot and undershoot, for a ramp values of 0.25 A/min, reduces for feed-forward control, with a maximum PEN temperature of 1141 K and 1135 K respectively for feed-back and feed-forward control.

Regarding P_{Cell} and U_{Cell}, the considerations for feed-forward control are the same as for feed-back control. Specifically, by reducing the ramp value, the magnitude of the power overshoot and undershoot reduces, but the speed of the system response does not change considerably.

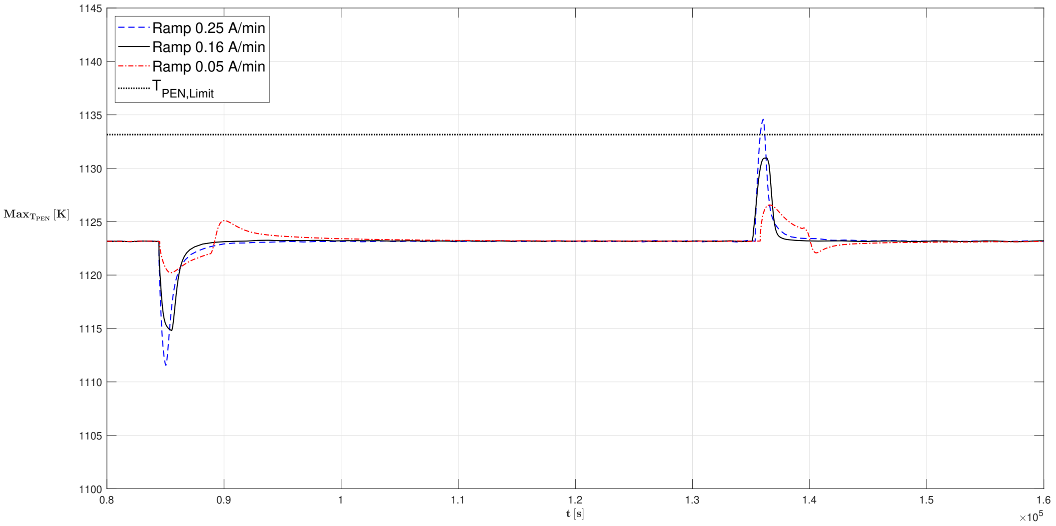

Figure 9.13: Simulated PEN temperature during load transients for different current ramp with feed-forward control.

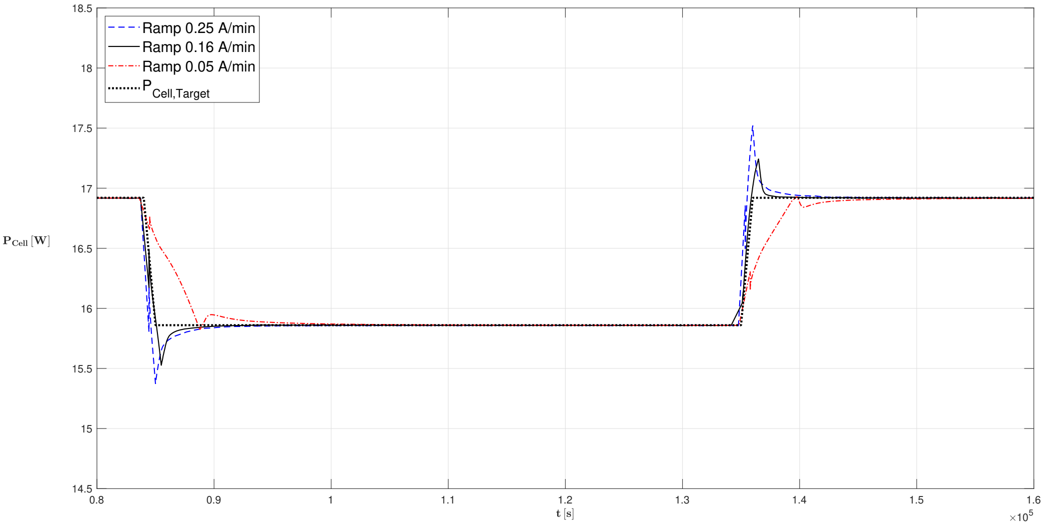

Figure 9.14: Simulated cell power during load transients for different current ramp with feed-forward control.

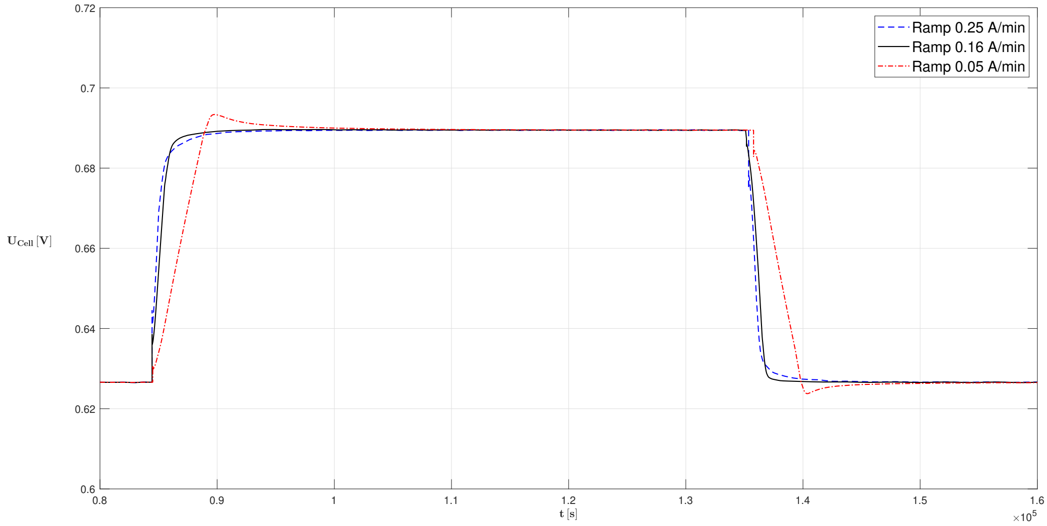

Figure 9.15: Simulated cell voltage during load transients for different current ramp with feed-forward control.

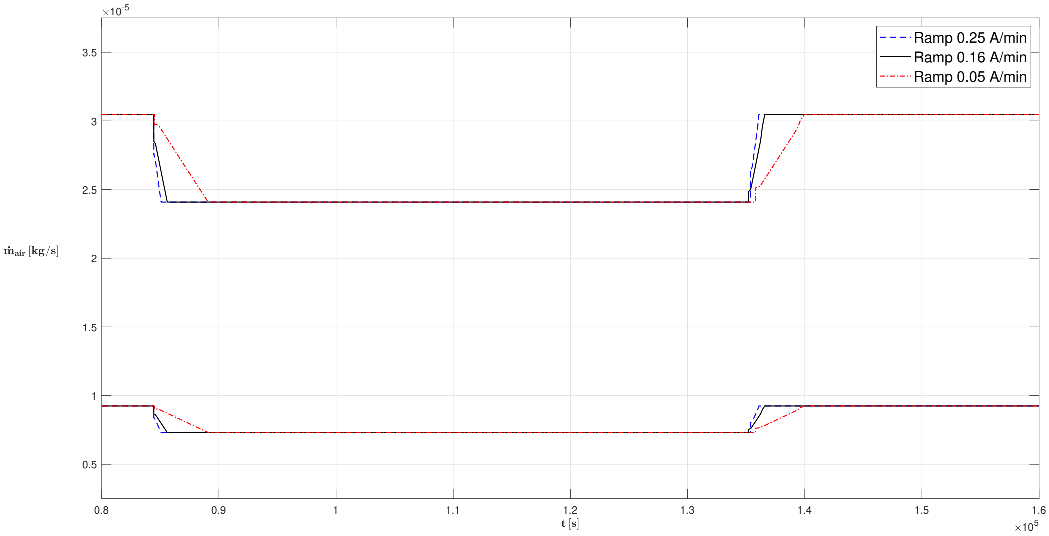

Figure 9.16: Simulated cathode air flow during load transients for different current ramp with feed-forward control.

Chapter 10

Conclusions and Recommendations

10.1 Conclusions

The conducted study represents a relevant step forward to better understand the influence of the Balance of Plant (BoP) components on a complete SOFC power generation system for maritime applications. For the chosen SOFC system configuration, these components consist of 3 blowers, two heat exchangers, a mixer, an external pre-reformer and an afterburner. In this study, each of these components has been modelled dynamically following a 0-D model approach. The correct implementation of the differential algebraic equations describing the physical phenomena occurring in each components, has been verified at steady-state conditions by using the software Cycle- Tempo.

The developed model is able to simulate the time variation of all the BoP component characteristics as well as their influence on the SOFC stack performance. Specifically, the influence of stack current, anode recirculating ratio and fuel utilization have been studied. It was shown how during nominal operation, there is no need of oxygen external supply through the catalytic partial oxidation (CPOx) air blower, since the high anode recirculating ratio of the AGR blower was sufficient to provide the right amount of oxidant for the pre-reforming process.

10.1.1 Influence of stack current

The system performance was considerably affected by changing the stack current. The other parameters, such as the oxygen carbon ratio (O/C), the anode recirculation ratio (RR) and the system fuel utilization ($U_{f,sys}$) were kept constant at their nominal values. The following conclusions are drawn:

- It is possible to achieve a stack efficiency of 63% and a system efficiency of 55 % when the stack electric current is 12 A;
- A stack electric current lower than 12 A, reduces the cathode air mass flow to values below the minimum imposed by the manufacturer;
- The power required by the ancillary devices, reduces by reducing the stack current resulting in an increase of the system efficiency;
- The main flows operating temperatures are significantly influenced by the heat exchanger design, which in this study has been based on the system's nominal operation. Lower currents increase the operating flows temperatures;
- The CO_2 emissions of the complete system are not significantly affected by the stack current;
- Controlling the PEN temperature solely with the cathode air flow, limits the system operation to stack electric currents above 12 A.

10.1.2 Influence of system fuel utilization

The system fuel utilization was changed between 0.7 and 0.9. The anode recirculating ratio and the methane flow entering the system, vary accordingly to keep the oxygen to carbon ratio and the stack current constant at their nominal values. The system fuel utilization affect the stack performance in the following manners:

- For a system fuel utilization of more than 85%, the cell voltage drops below the lower limit imposed by the manufacturer, at nominal current (27 A);
- The temperature of the air and fuel entering the stack are negligibly affected by the change of the system fuel utilization;
- In the afterburner, a temperature decrease of 200 K is observed when increasing the system fuel utilization from 70% to 90%;
- No relevant changes in the system CO_2 emissions are observed for different system fuel utilization;
- The highest system and stack efficiencies are reached for a system fuel utilization of 90% with 49% and 39% respectively;
- When working at 15 A, the increase of the system fuel utilization does not result in a cell voltage drop below the lower limit imposed by the manufacturer;
- A system and stack efficiency respectively of 58% and 66% are achieved for a system fuel utilization of 90% when working at stack current of 15 A.

10.1.3 Influence of anode recirculating ratio

The anode recirculating ratio is varied between 0 and 0.7. System fuel utilization, oxygen to carbon ratio and stack current are kept constant at their respective nominal values. The effect of anode recirculating ratio on the system performance is summarised as follows:

- The reduction of the cell voltage caused by increasing the anode recirculation ratio is less than 0.02 V;
- The biggest contribution of the parasitic losses is by the cathode air blower;
- The change in the pre-reformer inlet composition due to the usage of anode gas recirculating and catalytic partial oxidation blowers, affects the fuel mass flow temperature significantly;
- A CO_2 reduction of 56% is achieved with an anode recirculating ratio of 70% (compared to 0%);
- The stack efficiency is slightly reduced for higher anode recirculating ratio, with the highest efficiency of 49% for zero recirculation;
- The system efficiency is slightly increased when the anode recirculating ratio is increased, with a maximum of 38% for 70% recirculation;
- Both stack and system efficiency are increased when working at lower current (15 A), reaching their maximum values for 70% recirculation with 61% and 52% respectively.

10.1.4 Load Transients

Four different simulation scenarios were run to evaluate the response of the system to a load change. The effect of stepping the current and ramping it with different ramp values has been studied. Moreover, the difference between feed-back and feed-forward control has been shown. The following conclusions are drawn:

- Stepping the current results in stack overheating. The PEN temperature exceeds the higher limit imposed by the manufacturer, thus thermal safe operation of the stack is not ensured;
- Ramping the current significantly reduce the temperature peaks and gradients, but does not affect the speed of the response;
- A feed-forward control strategy significantly reduces the PEN temperature undershoot and overshoot during a step change;
- When feed-back control is applied, only a current ramp of 0.05 A/min ensures safe operation;
- When feed-forward control is applied, both current ramps of 0.05 A/min and 0.16 A/min ensure safe operation;
- A ramp value of 0.25 A/min results in a temperature overshoot above the upper limit imposed by the manufacturer, both for feed-forward and feed-back control strategy.
- With the current temperature control method, the system is able to respond to the load change within 2 hours;

The overall objective of this research was to: *Gain insight in the performance of the BoP components and the influence on the SOFC power generation system for maritime applications.*

To be able to answer the main research question of ”*How do the BoP components affect the SOFC system efficiency and load following capabilities ?*”, the following sub-question wer answered:

Which components affect the SOFC system performance the most during the specified operations?

Amongst all the Balance of Plant components studied and presented in this research, the cathode air blower, the CPOx blower, the AGR blower and the air heat exchanger represent the components that affect the system performance the most.

What is the effect of these components on the SOFC system efficiency and load following capabilities?

The presented results have shown how, the power required by the cathode air blower represents the highest contribution of the parasitic losses, among the ancillary devices. While, the AGR blower and the CPOx blower are strictly related to each other. Specifically, for high recirculating ratio, the CPOx blower can be turned off and the cathode air blower requires the least amount of power, thus the system efficiency reaches its highest value. For lower recirculating ratio, the amount of power required by the cathode air blower and the CPOx blower increases. This results in lower system efficiency, especially when working at high current.

The heat exchanger design is of significant importance for the system operations since it is related to the flow operating temperatures and thus the stack temperature. In particular, the inertia of the air heat exchange process plays an important role in the system response capabilities, since, in this research, the air flow is the only responsible for the thermal safe operation of the stack.

Which control strategy can ensure a relatively fast system response?

Feed-back and feed-forward control are studied and compared in this research. It has been shown how a ramp load change produces a lower PEN temperature overshoot when compared to a step change. Moreover, results have shown how, with both control strategies, the system responded to a load change of 4 A, within 2 hours. However, when feed-forward control is used, higher current ramps and lower PEN temperature overshoots are achievable.

10.2 Recommendations

The developed model represents a solid base for future development and research in modelling SOFC power generation systems for maritime applications. Based on the made assumptions and the produced results, different recommendations are here reported for future investigations:

Model Validation The chosen SOFC system configuration represents one of the possible configurations available in the market. Validating the model requires first to find an experimental set-up or an existing system with a similar configuration to the one proposed in this research. Then assess how well the model predicts the system's operations. For the developed model, validation is not possible in this research although it would be extremely useful to confirm the obtained results.

Adiabatic Process Assumption All the processes modelled in this research are considered adiabatic, meaning that, for each component, the heat transferred to the surroundings has been neglected. This assumption simplifies the equations describing the thermal phenomena occurring in the system, but the heat exchange processes occurring among the hot components (i.e. the stack, the heat exchangers, the post-burner and the pre-reformer) are not considered. However, quantifying the contribution of each hot components to the heat exchange process is challenging and would require more research.

System Optimization The developed model is able to simulate the system performance for different stack currents, system fuel utilization factor and anode recirculating ratios. The model may be used to find the optimal operating point of the complete system by varying these parameters, but also the BoP components size and for the different types of fuel. The fuel processing subsystem is implemented in such a way that any combination of CH_4, CO_2, CO, H_2, H_2O, N_2 and O_2 can be used. Different fuels, such as ammonia and methanol can be used in the model, but modifications of the implemented equations as well as the BoP components configuration is required (e.g. cracking of the ammonia occurs at the SOFC anode thus no pre-reformer is needed).

Start-up Operations Depending on the operational profile, the power generation system on board a vessel could require frequently start-ups and shutdowns. Usually, SOFC systems operate continuously since start-up times are relatively long. There are several strategies which could allow the system to increase the response speed during these operations and modelling them would help to understand which one is the most suitable depending on the operations. The developed model in this research represents a solid base to simulate start-up and shutdown operations, but important considerations must be taken into account. The SOFC stack model implemented has been validated for specific high temperature operating conditions. Consequently, in order to simulate start-up operations, modifications in the stack model equations are necessary and the model might require validation of the new operating conditions. Additionally, a different configuration of the BoP components might be used during start-ups, e.g. a combination of CPOX blower and AGR blower might be considered as strategy to reduce start-up times.

Load Transients The change of the power demand on board of a ship is highly dependent on the ship's type and its operational profile. Some vessels, such as dredgers, require a power generation system capable of rapidly respond to an instantaneous load change. Usually, when fuel cells are used on board, hybridisation with storage components (i.e. batteries and super-capacitors) is adopted to meet the load changes. In this research, the limitation of a SOFC system during load transients, has been demonstrated. The chosen control strategy can be further improved, aiming at enhancing the transient abilities of the system.

Control Strategy In this research, it has been shown how a feed-forward PEN temperature control strategy represents a better choice, for load transients, compared to feed-back control. With feed-forward control, higher current ramp values can be achieved and the system overshoot may be reduced considerably. However, the speed of the system response does not change if feed-forward control is implemented. It would be interesting to evaluate a different control strategy which would allow a faster response without resulting in stack overheating. One strategy could be to start ramping or even stepping the cathode air flow before ramping the current. In this way, it would be theoretically possible to use higher ramp values with the possible effect of a faster system response. To ensure thermal safe operation, another option would be to work at lower temperatures (e.g. lower air inlet temperature achieved by bypassing the pre-heater) so that when the load change occurs, the maximum PEN temperature remains below the higher limit.

Control Parameters The results obtained showed also that a control system depending solely on the cathode air flow has limits. Specifically, the cathode air is used not only as oxidant for the electrochemical reaction occurring in the SOFC stack, but also as the only cooling flow for the PEN temperature control system. This represents a limit of the control developed, since by reducing the electric current, the cathode air flow reduces so to keep the maximum PEN temperature equal to 850 $^\circ$ C. However, it was shown how for electric current values below 12 A, the cathode air flow reduces to an amount not sufficient to ensure that the electrochemical reaction occurs. Therefore, it would be interesting to develop a control strategy which does not rely solely on the cathode air flow. The fuel flow and the AGR flow might be considered as alternative.

Bibliography

[1] International Maritime Organization, *"Third IMO GHG Study 2014"*, IMO 2015.

[2] *"World Energy Outlook 2018 "*, International Energy Agency (IEA) 2018.

[3] *"Amendments to the annex of the protocol of 1997 to amend the international convention for the prevention of pollution from ships, 1973, as modified by the protocol of 1978 relating thereto: Inclusion of regulations on energy efficiency for ships in MARPOL"* Annex VI, Resolution MEPC.304(72), IMO 2018.

[4] *"Maritime forecast to 2050: Energy transition outlook"* DNV GL 2018.

[5] International Maritime Organization, *"Adoption of the inital strategy on reduction of GHG emissions from ships and existing IMO activity related to reducing GHG emissions in the shipping sector"*, Annex 11, Resolution MEPC.304(72) IMO 2015.

[6] DNV-GL, *"Assessment of selected alternative fuels and technologies"*, June 2019.

[7] DNV-GL, *"Comparison of Alternative Marine Fuels"*, Report No.2019-0567, Rev.3 2019.

[8] United Nations Conference on Trade and Development, *"Review of Maritime Transport 2019"*, United Nations 2019.

[9] P. Uva, *"Dynamic Modelling of Solid Oxide Fuel Cell System. Integration of 1-D SOFC Dynamic Model with the Balance of Plant components: Literature Study"*, Delft University of Technology, 2020.

[10] K.J. Astrom, T. Hagglund, *"PID Controllers- Theory, Design and Tuning (2nd Edition)."*, Instrument Society of America, 1995.

[11] J.G. Ziegler, N.B. Nichols, *"Optimum Settings for Automatic Controllers."*, Journal of Dynamic System Measurement and Control , pp. 759-765, 1942.

[12] A.L. Dicks, D.A.J. Rand *"Fuel Cell Systems Explained"*, John Wiley & Sons Ltd, 2018.

[13] N.P. Brandon, E.Ruiz-Trejo, P. Boldrin *"Solid Oxide Fuel Cell Lifetime and Reliability"*, Imperial College London 2017.

[14] National Energy Technology Laboratory, *"Fuel Cell Handbook"*, EG & G Services Parson Inc., 2000.

[15] D. Marra, C. Pianese, P. Polverino, M. Sorrentino, *"Models for Solid Oxide Fuel Cell Systems"*, Springer-Verlag, 2016.

[16] T. Namioka, T. Naruse, R. Yamane, *"Behaviour and mechanisms of Ni/ScSz cermet anode deterioration by trace tar in wood gas in a solid oxide fuel cell"*, International Journal of Hydrogen Energy, Vol.36, pp. 5581-5588, 2011.

[17] P. Colonna, H. van Putte, *Dynamic modeling of steam power cycles. Part I- Modeling paradigm and validation*, Applied Thermal Engineering, Vol.27, pp. 467-480, 2007.

[18] J. Milewski *"A Mathematical Model of SOFC: A Proposal"*, FUEL CELLS 12 Vol.5, pp.709-721 2012.

[19] J.Li, Z. Bai, E. Croiset, *"A two-dimensional modeling of solid oxide fuel cell button cells with detailed electrochemistry mechanism"*, Journal of Power Sources, Vol.333, pp. 164-172, 2016.

[20] K.J.Kattke, R.J. Braun, A.M. Colclasure, G. Goldin, *"High-fidelity stack and system modeling for tubular solid oxide fuel cell system design and thermal management"*, Journal of Power Sources, Vol.196, pp. 3790-3802, 2011.

[21] L.van Biert, M. Godjevac, K. Visser, P.V. Aravind *"Dynamic modelling of a direct internal reforming solid oxide fuel cell stack based on single cell experiments"*, Applied Energy, Vol.250, pp. 976-990, 2019.

[22] M. Azzopardi, *"Dynamic Model Implementation for a Multi-Purpose 1-D Planar SOFC: Gaining Insight Behaviour into an Intermediate Temperature SOFC"*, Delft University of Technology, 2017. `https://repository.tudelft.nl/islandora/object/uuid%3A2a4683ac-f345-464c-97ce-b11bc3631ed2?collection=education`

[23] H. Xi, J. Sun, V. Tsourapas, *"A control oriented low order dynamic model for planar SOFC using minimum Gibbs free energy method"*, Journal of Power Sources, Vol.165, pp. 253-266, 2007.

[24] K.H.Lee, R.K. Strand *"A system level simulation of SOFC systems for building applications"*, Third National Conference of IBPSA-USa, pp. 29-36, 2008.

[25] M.Murshed, B. Huang, K. Nandakumar, *"Control relevant modeling of planar solid oxide fuel cell system"*, Journal of Power Sources, Vol.163, pp. 830-845, 2007.

[26] L. Barelli, G. Bidini, F. Gallorini, P.A. Ottaviano, *"Design optimization of a SOFC-based CHP system through dynamic analysis"*, Journal of Hydrogen Energy, Vol.38, pp. 354-369, 2013.

[27] K. Sedghisigarchi, A. Feliachi, *"Dynamic and Transient Analysis of Power Distribution System With Fuel Cells- Part 1: Fuel-Cell Dynamic Model"*, IEEE Transactions on energy conversion, Vol.19, pp. 423-428, 2004.

[28] K. Nanaeda, F. Mueller, J. Brouwer, S. Samuelsen, *"Dynamic modeling and evaluation of solid oxide fuel cell- combined heat and power system operating strategies"*, Journal of Power Sources, Vol.195, pp. 3176-3185, 2010.

[29] S.A. Hajimolana, M. Soroush, *"Dynamics and Control of a Tubular Solid Oxide Fuel Cell"*, Ind. Eng. Chem. Res., Vol.48, pp. 6112-6125, 2009.

[30] A. Sorce, A. Greco, L. Magistri, P. Costamagna, *"FDI oriented modeling of an experimental SOFC system, model validation and simulation of faulty states"*, Applied Energy, Vol.136, pp. 894-908, 2014.

[31] M. Sorrentino, C. Pianese, *"Grey-Box Modeling of SOFC Unit for Design, Control and Diagnostics Applications"*, Session B03- HT Fuel Cell System and Balance of Plant 1, 2009.

[32] R. Bove, S. Ubertini, *"Modeling solid oxide fuel cell operation: Approaches, techniques and results"*, Journal of Power Sources, Vol.159, pp. 543-559, 2006.

[33] N.D. Tuyen, G. Fujita, *"Modelling a SOFC Power Unit Using Natural Gas Fed Directly"*, Shibaura Institute of Technology, Japan, 2012.

[34] S.H. Chan, O.L. Ding *"Simulation of a solid oxide fuel cell power system fed by methane"*, International Journal of Hydrogen Energy, Vol.30, pp. 167-179, 2005.

[35] N. Lu, Q. Li, X. Sun, M.A. Khaleel, *"The modeling of a standalone solid-oxide fuel cell auxiliary power unit"*, Journal of Power Sources, Vol.161, pp. 938-948, 2006.

[36] L. Magistri, F. Trasino, P. Costamagna, *"Transient Analysis of Solid Oxide Fuel Cell Hybrids- Part 1: Fuel Cell Models"*, ASME, Vol.128, pp. 288-293, 2006.

[37] D. Andersson, E. Aberg, J. Eborn, J. Yuang, B. Sundén, *"Dynamic modeling of a solid oxide fuel cell system in Modelica"*, Proceeding 8th Modelica Conference Germany, 2011.

[38] P.P.Oprychpaulina, S.M.Hosseini, Z.Jaworski, *Model development of integrated CPOx reformer and SOFC stack system*, Polish Journal of Chemical Technology, Vol.18, pp. 41-46, 2016.

[39] S. Farhad, F. Hamdullahpur, Y. Yoo , *"Performance evaluation of different configurations of biogas-fuelled SOFC micro-CHP systems for residential applications"*, Journal of Hydrogen Energy, Vol.35, pp. 3758-3768, 2010.

[40] N. Hotz, S. M. Senn, D. Poulikakos , *"Exergy analysis of a solid oxide fuel cell micro-powerplant"*, Journal of Power Sources, Vol.158, pp. 333-347, 2006.

[41] K. Sedghisigarchi, A. Feliachi, *"Dynamic and Transient Analysis of Power Distribution System With Fuel Cells- Part 2: Control and Stability Enhancement"*, IEEE Transactions on energy conversion, Vol.19, pp. 429-434, 2004.

[42] D.F. Cheddie, N.D.H. Munroe *"A dynamic 1D model of a solid oxide fuel cell for real time simulation"*, Journal of Power Sources, Vol.171, pp. 634-643, 2007.

[43] M. Sorrentino, C. Pianese, Y.G. Guezennec, *"A hierarchical modeling approach to the simulation and control of planar solid oxide fuel cells"*, Journal of Power Sources, Vol.180, pp. 380-392, 2008.

[44] Y.W.Kang, J. Li, G.Y. Cao, H.Y. Tu, J.Li, J. Yang, *"A reduced 1D dynamic model of planar direct internal reforming solid oxide fuel cell for system research"*, Journal of Power Sources, Vol.188, pp. 170-176, 2009.

[45] L. Zhang, X. Li, J. Jiang, S. Li, J. Yang, *"Dynamic modeling and analysis of a 5 kW solid oxide fuel cell system from the perspectives of cooperative control of thermal safety and high efficiency"*, Journal of Hydrogen Energy, Vol.40, pp. 456-476, 2015.

[46] S.M. Shaikh, M.A.Shaik, *"Importance of modelling and simulation: a vital Systems Engineering technique"*, International Journal of Advances in Science Engineering and Technology, Vol.5 pp. 121-124 2017.

[47] C.H. Shomate, *"A method for evaluating and correlating thermodynamic data"*, Journal of Physical Chemistry, Vol.58, pp. 368-372, 1954.

[48] W.G.Mallar, *"National Insitute of Standard Technology and Technology Chemistry WebBook"* 2020.

[49] B.J. McBride, S. Gordon, M.A. Reno, *"Coefficients for Calculating Thermodynamic and Transport Properties of Individual Species"* NASA Technical Memorandum 4513, 1993.

[50] L. van Biert *Solide oxide fuel cells for ships: System integration concepts with reforming and thermal cycles* PhD dissert. Delft University of Technology, 2020.

[51] R. O'Hayre, S.W. Cha, W.G. Colella, F.B. Prinz *"Fuel Cell Fundamentals"*, John Wiley & Sons Ltd, 2016.

[52] A. Nakajo, Z.Wuillemin, J.van Herle, D. Favrat, *"Simulation of thermal stresses in anode-supported solide oxide fuel cell stacks. Part I: Probability of failure of the cells"*, Journal of Power Sources, Vol.193, pp. 203-215, 2009.

[53] C. Ratnasamy, J. P. Wagner, S. Spivey, E. Weston, *"Removal of sulfur compounds from natural gas for fuel cell application using a sequential bed system"*, Catalysis Today, Vol.198, pp. 233-238, 2012.

[54] H. Cui, S.Q. Turn, M. A. Reese, *"Removal of sulfur compounds from utility pipelined synthetic natural gas using modified activated carbons"*, Catalysis Today, Vol.139, pp. 274-279, 2009.

[55] O. van Rheinberg, K. Lucka, H. Kohne, T. Schade, J. T. Andersson, *"Selective removal of sulphur in liquid fuels for fuel cell applications"*, Fuel, Vol.87, pp. 2988-2996, 2008.

[56] A. Filippi *"Development and experimental validation of CPOx reforming dynamic model for fault detection and isolation in SOFC systems"*, PhD diss. Dipartimento di Ingegneria Meccanica, 2014.

[57] J. Zhu, D. Zhang, K.D. King, *"Reforming of* CH_4 *by partial oxidation: thermodynamic and kinetic analyses"*, Fuel, Vol.80, pp. 899-905, 2000.

[58] P. Koukkari, R. Pajarre, *"A Gibbs energy minimization method for constrained and partial equilibria"*, Pure and Applied Chemistry, Vol.83, pp. 1243-1254, 2011.

[59] R.H. Perry, D.W. Green, *"Perry's Chemical Engineers Handbook"*, 8th Edition, McGraw-Hill, 2008.

[60] G. Veser, J: Frauhammer, U. Friedle, *"Syngas formation by direct oxidation of methane: Reaction mechanisms and new reactor concepts"*, Catalysis Today, Vol.61, pp. 55-64, 2000.

[61] F. Basile, G. Fornassari, F. Trifirò, A. Vaccari, *"Partial oxidation of methane: Effect of reaction parameters and catalyst composition on the thermal profile and heat distribution"*, Catalysis Today, Vol.64, pp. 21-30, 2001.

[62] O.E. Ataer, A. Jleri, Y. Gogus, *"Transient behaviour of finned-tube cross-flow heat exchangers"*, International Journal of Refrigeration, Vol. 18, pp. 153-160, 1995.

[63] O.M.E.S. Khayal, *"Fundamentals of heat exchangers"*, International Journal of Research in Computer Application and Robotics, Vol. 6, pp.1-11, 2018.

[64] N. Lu, Q. Li, X. Sun, M.A. Khaleel, *"The modeling of a standalone solid-oxide fuel cell auxiliary power unit"*, Journal of Power Sources, Vol. 161, pp. 938-948, 2006.

[65] J.B. Heywood, *"Internal combustion engine fundamentals"*, Mc Graw Hill, 1988.

[66] P. Lisbona, A. Corradetti, R. Bove, P. Lunghi, *"Analysis of a solid oxide fuel cell system for combined heat and power applications under non-nominal conditions"*, Electrochimica Acta, Vol.53, pp. 1920-1930, 2007.

[67] A.O. Omosun, A. Bauen, N.P. Brandon, C.S. Adjiman, D. Hart, *"Modelling system efficiencies and cost of two biomass-fuelled SOFC systems"*, Journal of Power Sources, Vol.131, pp. 96-106, 2004.

[68] P. Kazempor, V. Dorer, F. Ommi, *"Evaluation of hydrogen and methane-fuelled solid oxide fuel cell systems for residential applications: System design alternative and parameter study"*, Journal of Hydrogen Energy, Vol.34, pp. 8630-8644, 2009.

[69] B.Conti, B. Bosio, S.J. McPhail, F. Santoni, D. Pumiglia, E. Arato, *"A 2-D model for Intermediate Temperature Solid Oxide Fuel Cells Preliminary Validated on Local Values"*, Catalyst, 9, 36, 2019.

[70] B.Ghorbani, K. Vijayaraghavan, *"3-D and simplified pseudo-2D modeling of single cell of a high temperature solide oxide fuel cell to be used for online control strategies"*, International Journal of Hydrogen Energy, Vol.43, pp. 9733-9748, 2018.

[71] A. Amiri, P. Vijay, M.O. Tadé, K. Ahmed, G.D. Ingram, V. Pareek, R. Utikar, *"Planar SOFC system modelling and simulation including a 3-D stack module"*, International Journal of Hydrogen Energy, Vol.41, pp. 2919-2930, 2016.

[72] B.Conti, B. Bosio, S.J. McPhail, F. Santoni, D. Pumiglia, E. Arato, *"Three-Dimensional CFD Modeling of Transport Phenomena in a Cross-Flow Anode-Supported Planar SOFC"*, Energies, Vol.7, pp.80-98, 2014.

[73] Y. Huangfu, F. Gao, A. Abbas-Turki, D. Bouquain, A. Miraoui *"Transient dynamic and modeling parameter sensitivity analysis of 1D solid oxide fuel cell model"*, Energy Conversion and Management, Vol.71, pp.172-185, 2013.

[74] Staxera, *Technical Documentation Integrated Stack Module (ISM V3.3 with ESC2 cells)* 2010.

[75] G. D'Andrea, M. Gandiglio, A. Lanzini, M- Santarelli *"Dynamic model with experimental validation of a biogas-fed SOFC plant"*, Energy Conversion and Management, Vol.135, pp.21-34, 2017.

Appendices

Appendix A

Derivation of relation (4.13) and (4.14)

The two relations derive from a carbon balance on the SOFC stack. For the proposed system configuration, it is possible to distinguish three different flows:

- $N_{C,SOFC}$ representing the flow of carbon that is electrochemically oxidized in the stack;
- $N_{C,CPOX}$ representing the flow of carbon that is oxidized in the CPOx reformer;
- $N_{C,RR}$ representing the flow of carbon that is recirculated in the system

It is then possible to define the flow of carbon in and out the stack as follow:

$$N_{C,IN} = N_{C,SOFC} + N_{C,CPOX} + N_{C,RR} \tag{A.1}$$

$$N_{C,OUT} = N_{C,SOFC} + N_{C,CPOX} \tag{A.2}$$

The amount of carbon recirculated is related to $N_{C,OUT}$ as follow:

$$N_{C,RR} = RR \cdot N_{C,OUT} \Longrightarrow RR = \frac{N_{C,RR}}{N_{C,OUT}} = \frac{N_{C,RR}}{N_{C,IN}} = \frac{N_{C,RR}}{N_{C,SOFC} + N_{C,CPOX} + N_{C,RR}} \tag{A.3}$$

Now it is possible to assume $N_{C,IN} = 1$ thus according to (A.3), $N_{C,RR} = RR$.
The flow of the oxygen out of the stack can be defined as follow:

$$N_{O,OUT} = N_{O,IN} = N_{O,CPOX} + N_{O,SOFC} \tag{A.4}$$

The CPOX oxygen flow is obtained considering that partial oxidation must take place, thus:

$$N_{O,CPOX} = 4 \cdot N_{C,CPOX} \tag{A.5}$$

While the oxygen flow from the electrochemical reaction occurring in the SOFC is determined considering the system fuel utilization:

$$N_{O,SOFC} = 4 \cdot U_{f,sys} \cdot N_{C,SOFC} \tag{A.6}$$

It is now possible to estimate the oxygen flow of the recirculated flow:

$$N_{O,RR} = RR \cdot \frac{4 \cdot U_{f,sys} \cdot N_{C,SOFC} + 4 \cdot N_{C,CPOX}}{N_{C,SOFC} + N_{C,CPOX}} \tag{A.7}$$

Consequently, the O/C ratio can be defined as follow:

$$O/C = \frac{N_{O,IN}}{N_{C,IN}} = N_{O,IN} = N_{O,CPOX} + N_{O,RR} \tag{A.8}$$

Now considering that for the assumption made, $N_{C,SOFC} + N_{C,CPOX} = 1 - RR$, and substituting (A.5) and (A.7) in (A.8):

$$O/C = 4 \cdot \left(N_{C,CPOX} + \frac{RR}{1-RR} \cdot (U_{f,sys} \cdot N_{C,SOFC} + N_{C,CPOX}) \right) \tag{A.9}$$

The above expression, relates $N_{C,CPOX}$ and $N_{C,SOFC}$. It is possible to consider individual fractions such that:

$$f_{C,SOFC} + f_{C,CPOX} = 1 \tag{A.10}$$

Where

$$f_{C,CPOX} = \frac{N_{C,CPOX}}{(N_{C,CPOX} + N_{C,SOFC})} \Longrightarrow N_{C,CPOX} = \frac{f_{C,CPOX}}{1 - f_{C,CPOX}} \cdot N_{C,SOFC} \tag{A.11}$$

Now by substituting in (A.11), $N_{C,SOFC} = 1 - RR - N_{C,CPOX}$ and considering relation (A.9):

$$f_{C,CPOX} = \frac{\frac{O/C}{4} - U_{f,sys} \cdot RR}{1 - RR \cdot U_{f,sys}} \tag{A.12}$$

(A.11) and (A.12) represent respectively relation (4.13) and (4.14) considering that $f_{C,CPOX} = f_{CH_4,CPOX}$.

Appendix B

NASA vs NIST thermodynamic properties estimation

The divergence in the data obtained for the heat exchanger model, might be attributed to the different approach used to simulate the thermodynamic properties of the gas mixture. Specifically, the model developed uses the Shomate equations with coefficient provided by the NIST WebBook [48], while Cycle Tempo uses a similar expression but with coefficient provided by NASA [49], which slightly differs from the ones provided by the NIST. The two approaches are here described.

The NASA empirical equations used to estimate heat capacity C_p°, enthalpy H° and entropy S° are as follow:

$$\frac{C_p^\circ(T)}{R} = a_1 + a_2 \cdot T + a_3 \cdot T^2 + a_4 \cdot T^3 + a_5 \cdot T^4 \tag{B.1}$$

$$\frac{H^\circ(T)}{R \cdot T} = a_1 + a_2 \cdot \frac{T}{2} + a_3 \cdot \frac{T^2}{3} + a_4 \cdot \frac{T^3}{4} + a_5 \cdot \frac{T^4}{5} + \frac{b_1}{T} \tag{B.2}$$

$$\frac{S^\circ(T)}{R} = a_1 \ln T + a_2 \cdot T + a_3 \cdot + a_4 \cdot \frac{T^3}{3} + a_5 \cdot \frac{T^4}{4} + b_2 \tag{B.3}$$

Where $C_p^\circ(T)$ and $S^\circ(T)$ represents respectively the heat capacity at constant pressure and the entropy at temperature T for standard state; while $H^\circ(T) = [H^\circ(T) - H^\circ(298.15)] + H^\circ(298.15)$ with $H^\circ(298.15)$ being the assigned enthalpy at 298.15 K for standard state. The term R represents the molar gas constant (8.31451 J/mol K).

The Shomate equations used to estimate heat capacity, enthalpy and entropy are:

$$C_p^\circ = A + B \cdot t + C \cdot t^2 + D \cdot t^3 + \frac{E}{t^2} \tag{B.4}$$

$$H^\circ - H^\circ_{298.15} = A \cdot t + B \cdot \frac{t^2}{2} + C \cdot \frac{t^3}{3} + D \cdot \frac{t^4}{4} - \frac{E}{t} + F - H \tag{B.5}$$

$$S^\circ = A \ln t + B \cdot t + C \cdot \frac{t^2}{2} + D \cdot \frac{t^3}{3} - \frac{E}{2 \cdot t^2} + G \tag{B.6}$$

Here C_p° represents the heat capacity at standard state, H° the standard enthalpy, S° the standard entropy and $t = T(K)/1000$.

Table B.1 shows an example of the heat capacity values obtained by using NASA and NIST coefficients, for some of the species involved in the system.

Table B.1: Example of heat capacity estimation using NASA and NIST coefficients

Temperature [K]	**Species** [-]	$\mathbf{C_{p,NASA}}$ [J/kg K]	$\mathbf{C_{p,NIST}}$ [J/kg K]	Δ [%]
700	N_2	1097.3	1098.2	0.083
	O_2	1030.4	1030.8	0.038
800	N_2	1121.9	1122.4	0.043
	O_2	1054.5	1054.4	0.013
900	N_2	1146.2	1146.0	0.013
	O_2	1074.1	1073.8	0.027
1000	N_2	1167.5	1167.7	0.019
	O_2	1090.0	1089.8	0.016
450	CH_4	2706.6	2712.2	0.206
500	CH_4	2886.5	2900.7	0.489
550	CH_4	3068.8	3089.9	0.683
600	CH_4	3250.3	3272.4	0.674

Appendix C

Additional Plots for Steady State Operation

Figures C.1, C.2 and C.3 show the stack inlet and outlet composition for different I_{stack}, $U_{f,sys}$ and RR respectively. For all the three figures it is possible to see how the H_2 concentration at the inlet is higher than that at the outlet. The opposite is true for H_2O. This demonstrates that in the stack, hydrogen is oxidized with the oxygen coming from the cathode side, producing H_2O (and power). Moreover, at the stack outlet there is no CH_4, showing that the methane entering the stack is reformed internally, consuming H_2O and producing CO and H_2, according to the MSR reaction. The presence of CO_2 in the inlet composition is justified by the fact that part of the outlet composition (containing CO_2 because of the WGS reaction), is reintroduced in the system through the AGR blower. Additionally, in Figure C.3 it is interesting to notice how N_2 concentration at the inlet and outlet, for all the RR values, remains the same since N_2 does not react in any of the reactions occurring inside the stack.

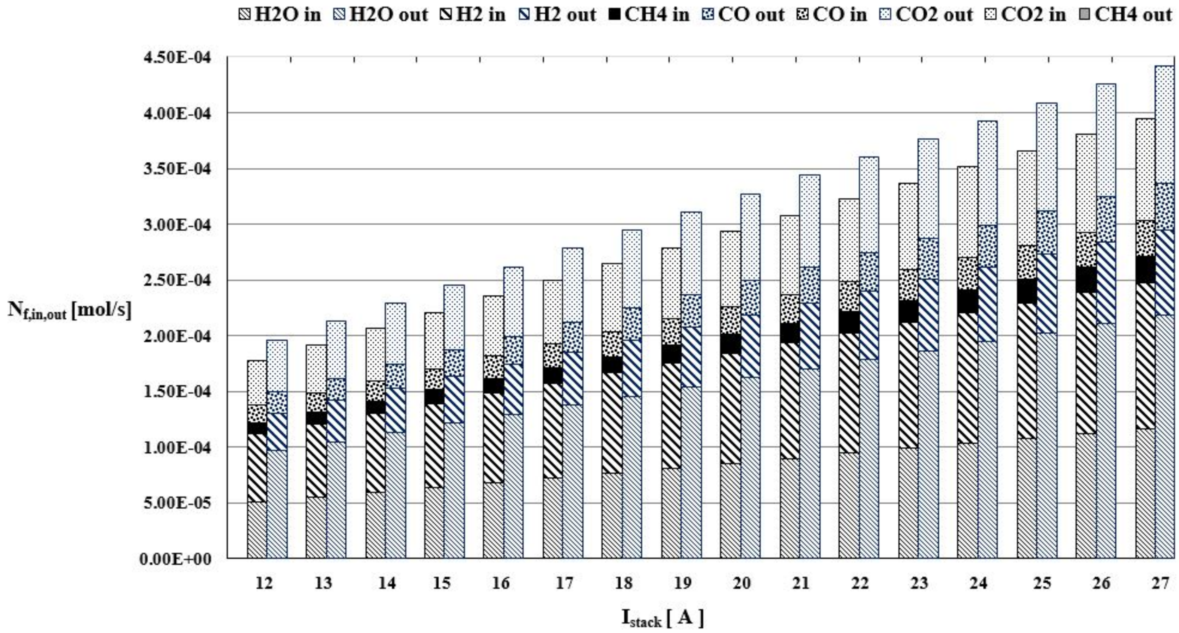

Figure C.1: Influence of stack current on the fuel molar flow at the stack inlet and outlet ($U_{f,sys}$ = 0.8, RR = 0.7).

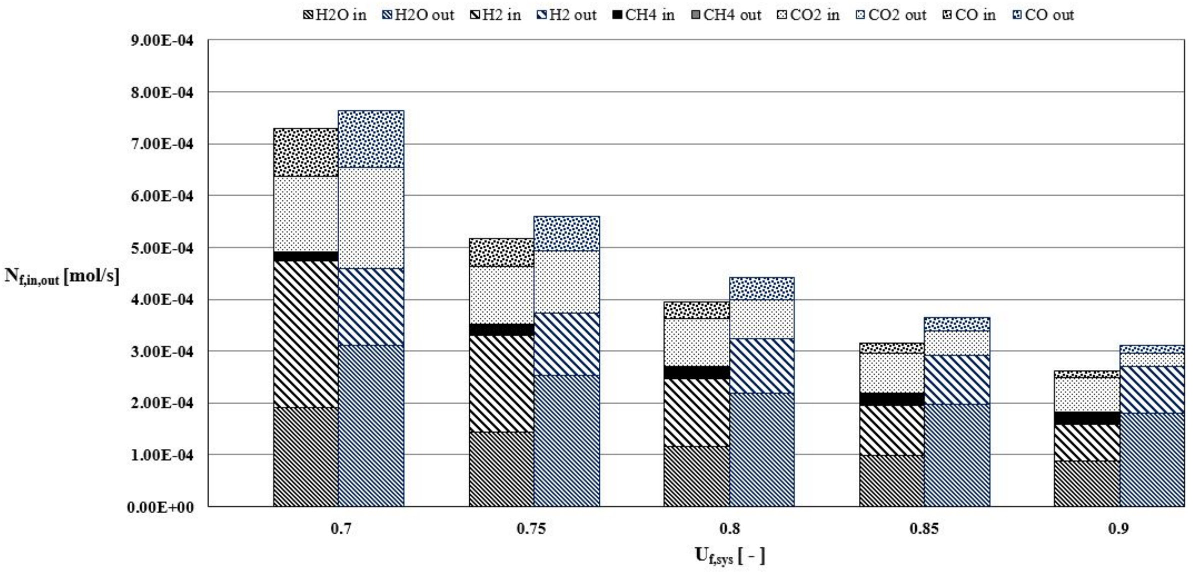

Figure C.2: Influence of the system fuel utilization on the fuel molar flow at the stack inlet and outlet @ I_{stack} = 27A. $U_{f,sys}$ is changed from 0.7 to 0.9 and RR and $\dot{m}_{CH_4}$, vary accordingly so to keep the O/C and I_{stack} constant

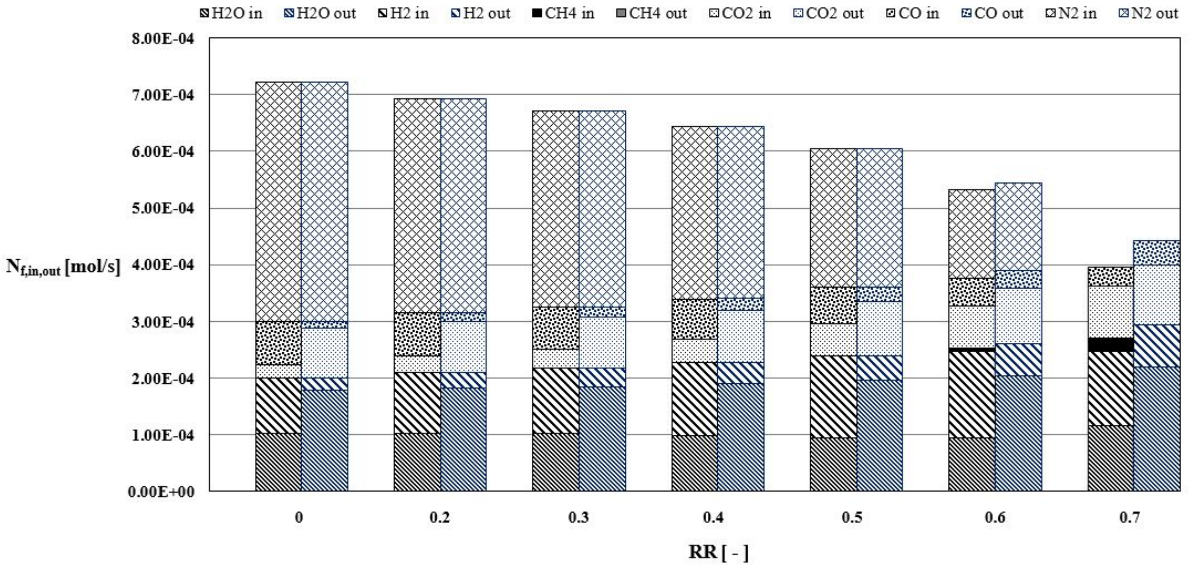

Figure C.3: Influence of recirculating ratio on the fuel molar flow at the stack inlet and outlet. RR changes from 0 to 0.7. $U_{f,sys}$, O/C and stack current are kept constant (I_{stack} = 27 A).

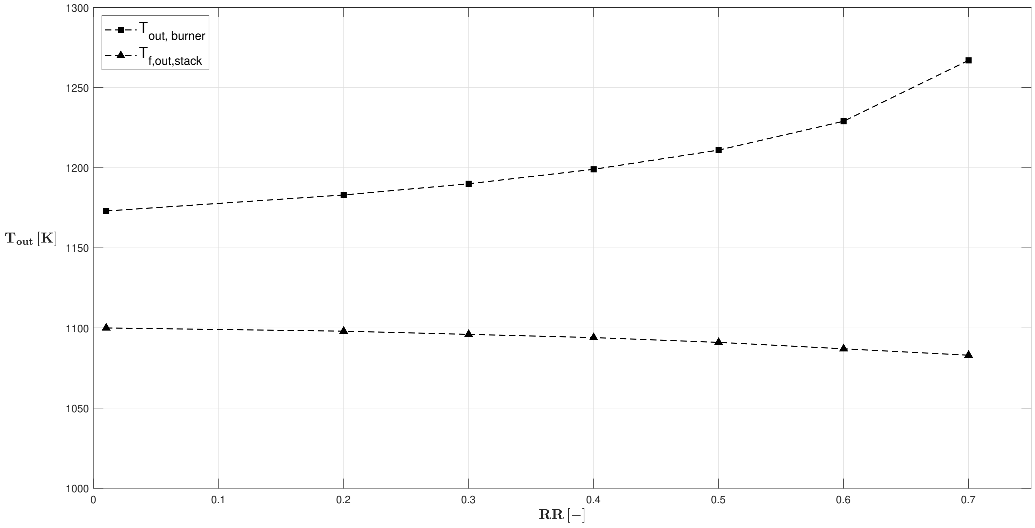

Figure C.4: Influence of the anode recirculating ratio on the stack and afterburner outlet temperature ($U_{f,sys} = 0.8$, $I_{stack} = 27\,A$). An increase of almost 100 K is observed for the afterburner outlet temperature, when RR is the highest.$T_{f,out,stack}$ does not change significantly.

Appendix D

Influence of $U_{f,sys}$ for I=15 A

The figures below show the effect of $U_{f,sys}$ on the BoP components when I_{stack} = 15 A. In particular, $U_{f,sys}$ is changed from 0.7 to 0.9 and RR and $\dot{m}_{CH_4}$, vary accordingly so to keep the O/C and I_{stack} constant.

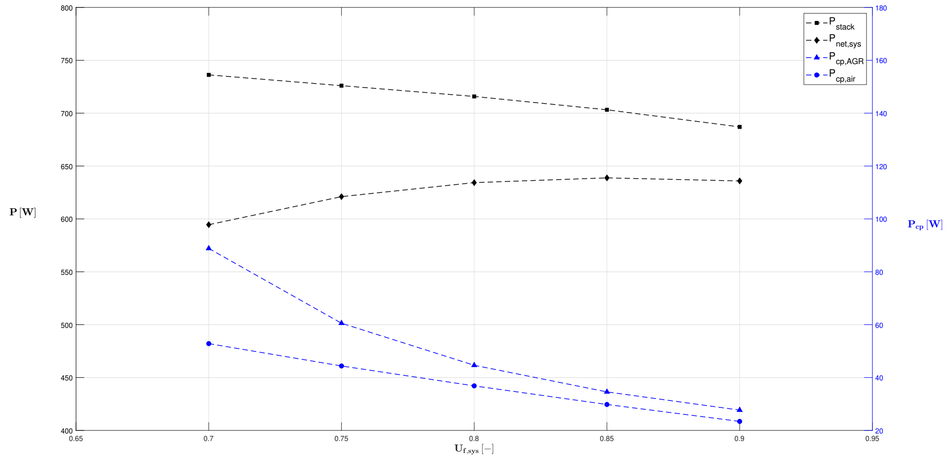

Figure D.1: Influence of system fuel utilization on the components power requirement for I_{stack} = 15 A.

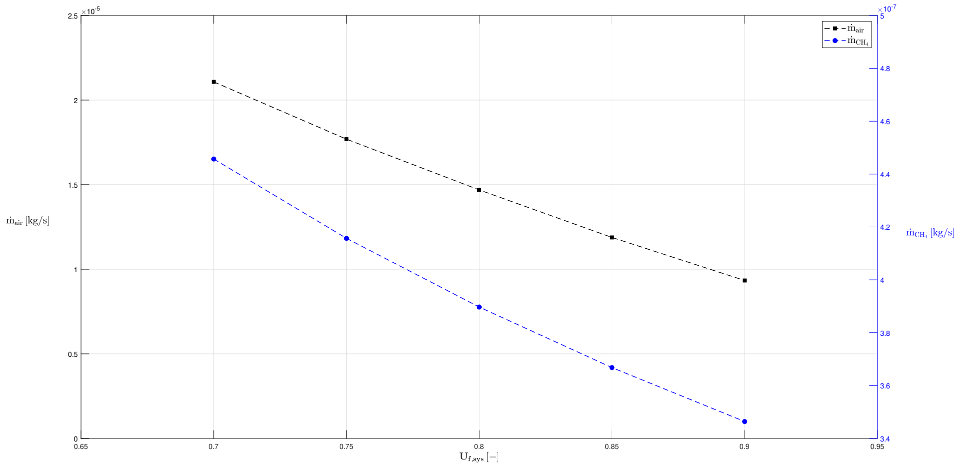

Figure D.2: Methane and cathode air mass flow for different values of $U_{f,sys}$ for I_{stack} = 15 A. The flows refer to single cell operation.

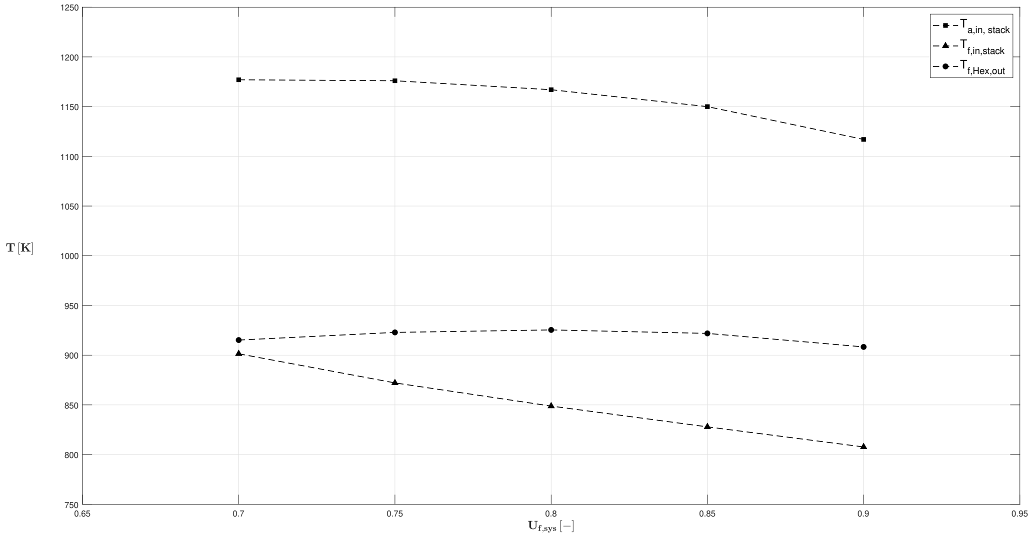

Figure D.3: Influence of the system fuel utilization on the air and fuel stack inlet temperature for I_{stack} = 15 A. $U_{f,sys}$ is changed from 0.7 to 0.9. RR and the $\dot{m}_{CH_4}$, vary accordingly so to keep the O/C and I_{stack} constant.

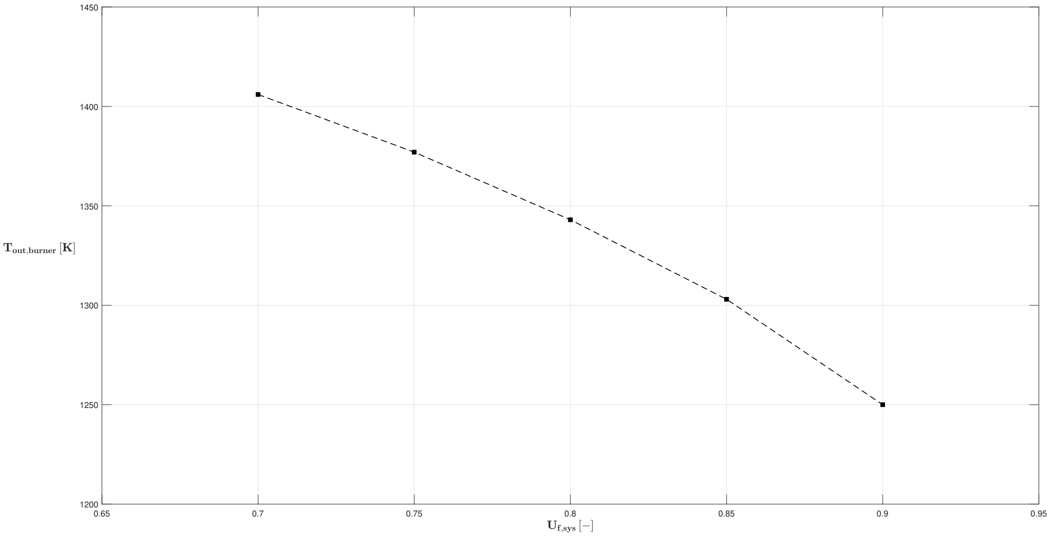

Figure D.4: Influence of the system fuel utilization on the outlet temperature of the afterburner for I_{stack} = 15 A.

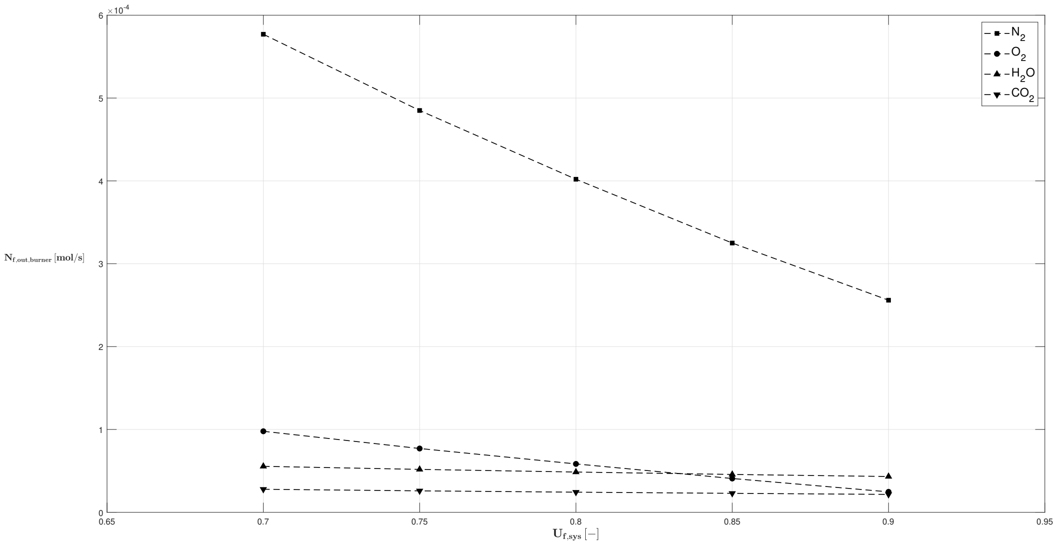

Figure D.5: Influence of system fuel utilization on the molar flow at the afterburner outlet for I_{stack} = 15 A.

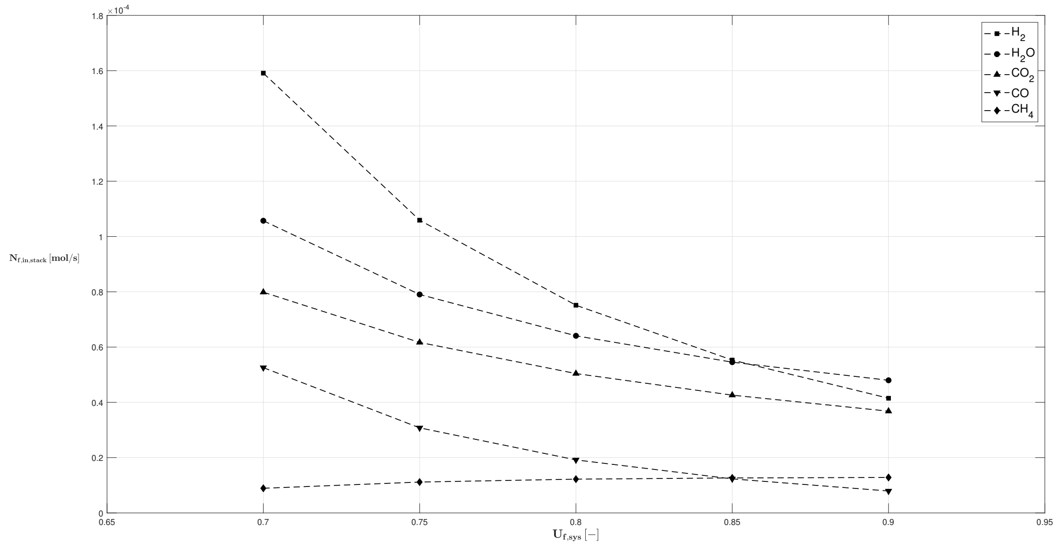

Figure D.6: Influence of system fuel utilization on the fuel molar flow at the stack inlet for I_{stack} = 15 A.

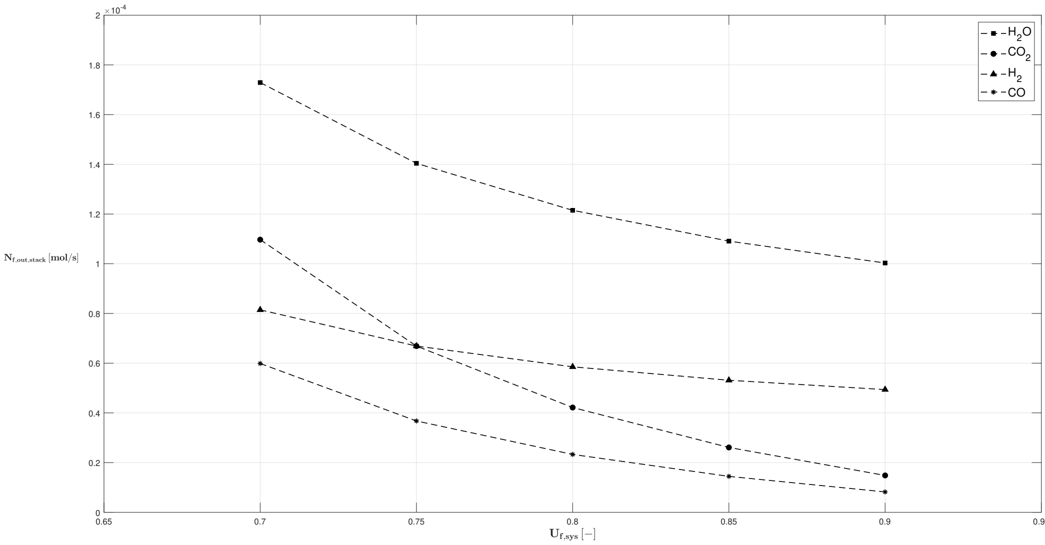

Figure D.7: Influence of system fuel utilization on the fuel molar flow at the stack outlet for I_{stack} = 15 A.

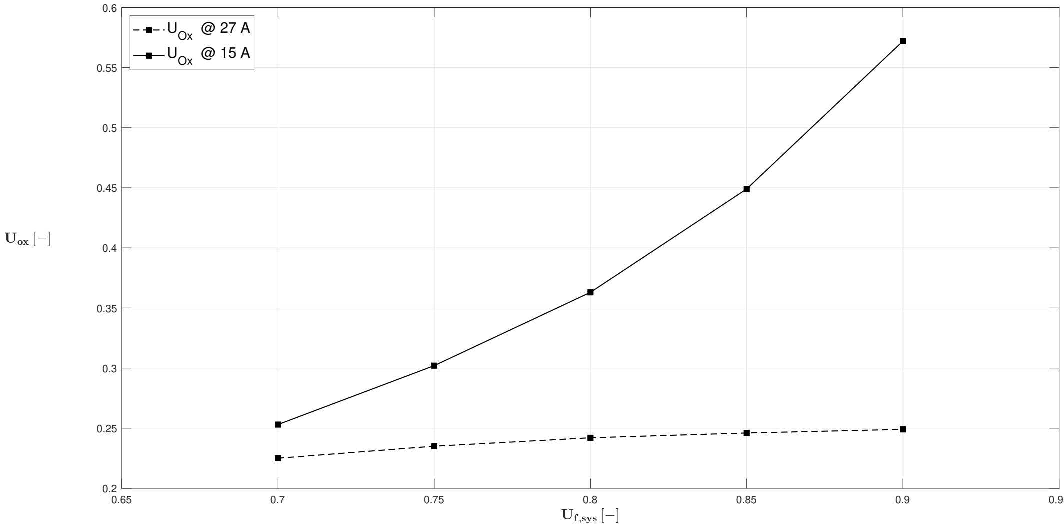

Figure D.8: Influence of system fuel utilization on the oxygen utilization. The comparison between I_{stack} = 15 A and I_{stack} = 27 A is shown.

Appendix E

Influence of RR for I=15 A

The figures below show the effect of RR on the BoP components characteristics. In particular, RR is changed from 0 to 0.7. $U_{f,sys}$, O/C and stack current are kept constant (I_{stack} = 15 A, $U_{f,sys}$ = 0.8).

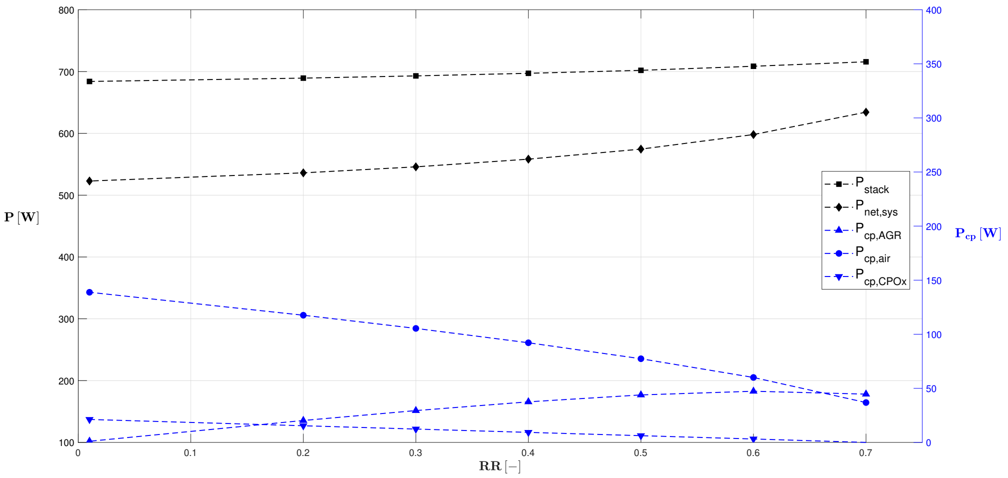

Figure E.1: Influence of recirculating ratio on the components power requirement for I_{stack} = 15 A.

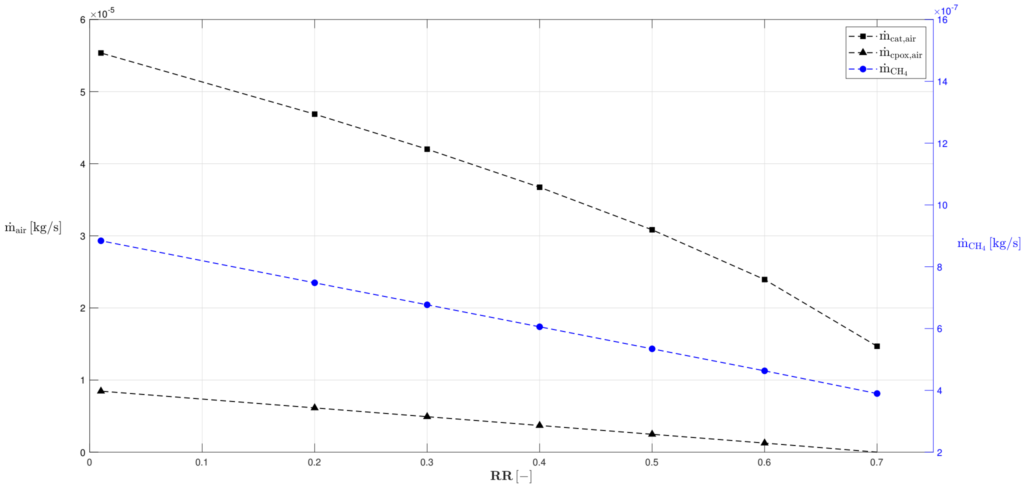

Figure E.2: Anode, cathode and CPOx mass flow for different RR @I_{stack} = 15 A. The flows refer to single cell operation.

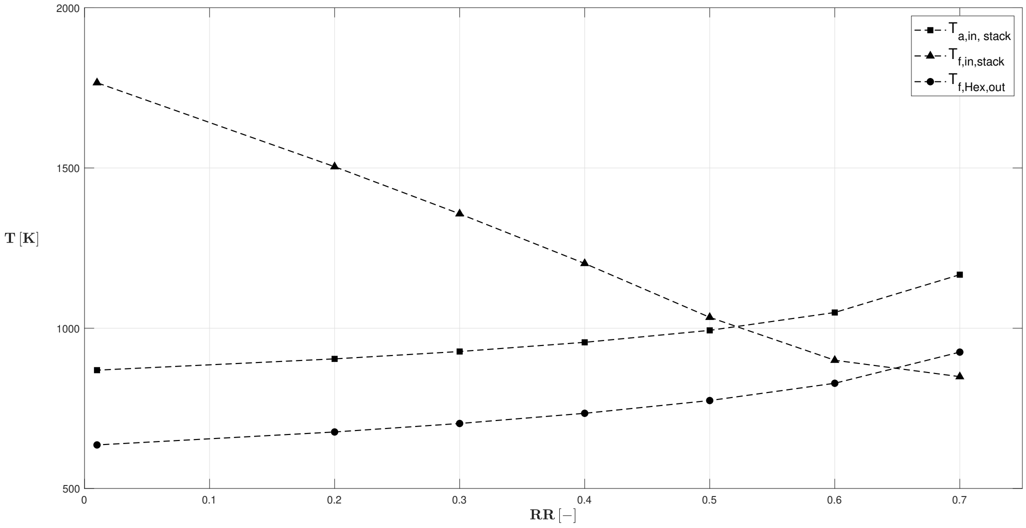

Figure E.3: Influence of the recirculating ratio on the air and fuel stack inlet temperature for I_{stack} = 15 A.

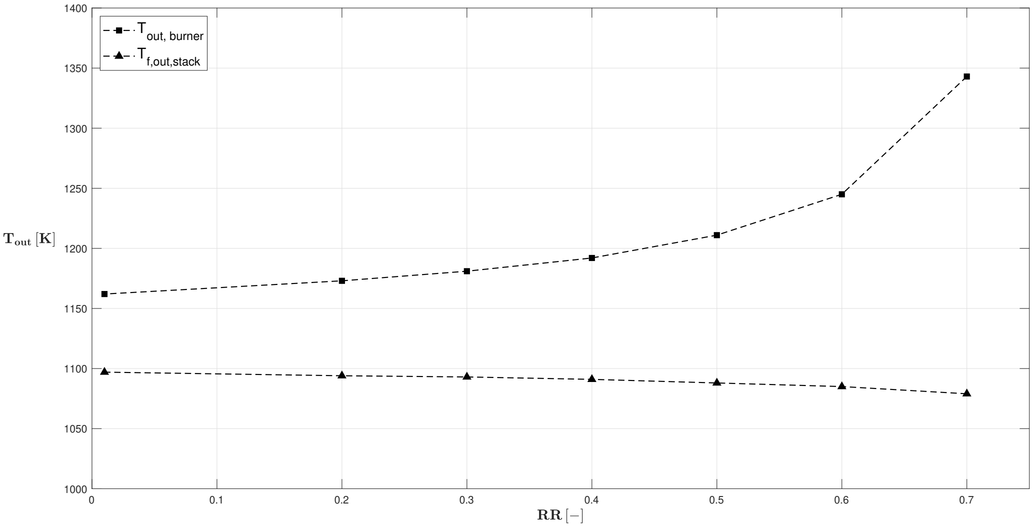

Figure E.4: Influence of the recirculating ratio on the outlet temperature of the afterburner and the stack for I_{stack} = 15 A.

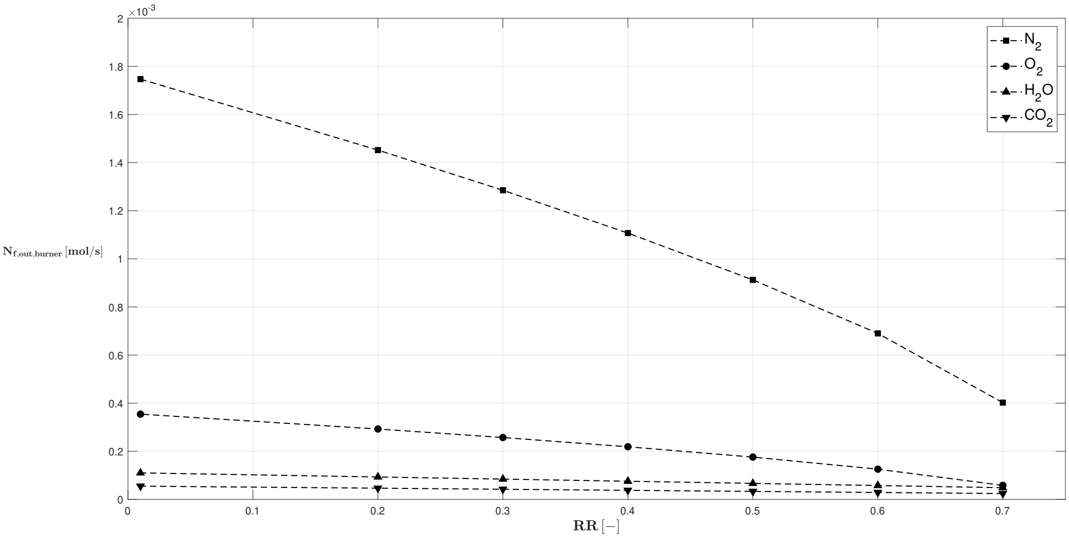

Figure E.5: Influence of recirculating ratio on the molar flow at the afterburner outlet for I_{stack} = 15 A.

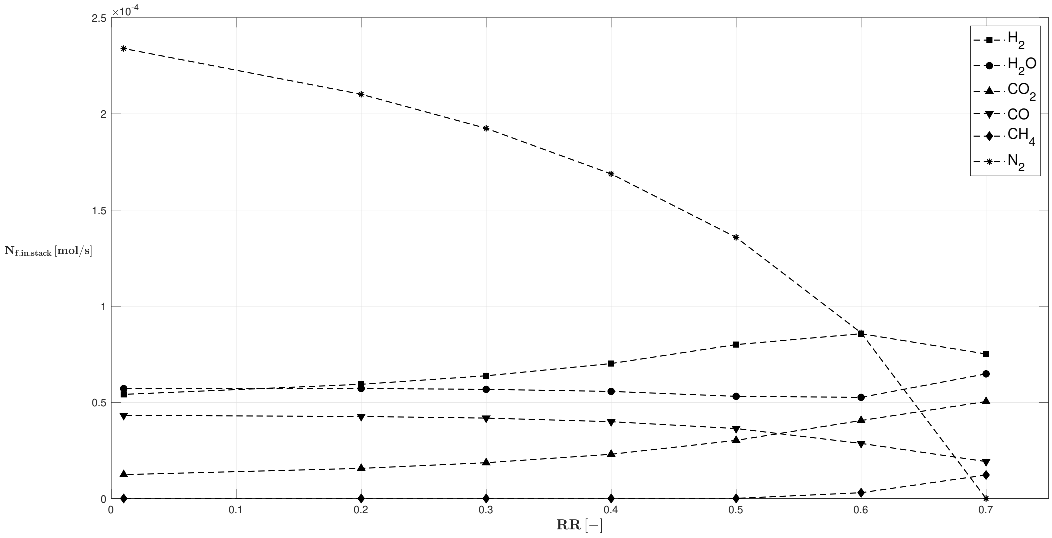

Figure E.6: Influence of recirculating ratio on the fuel molar flow at the stack inlet for I_{stack} = 15 A.

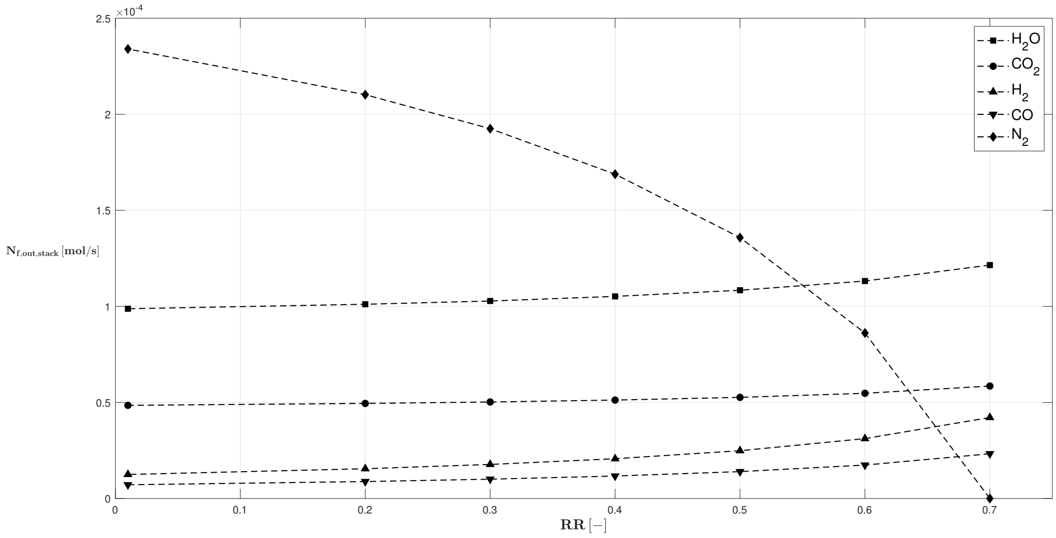

Figure E.7: Influence of recirculating ratio on the fuel molar flow at the stack outlet for I_{stack} = 15 A.

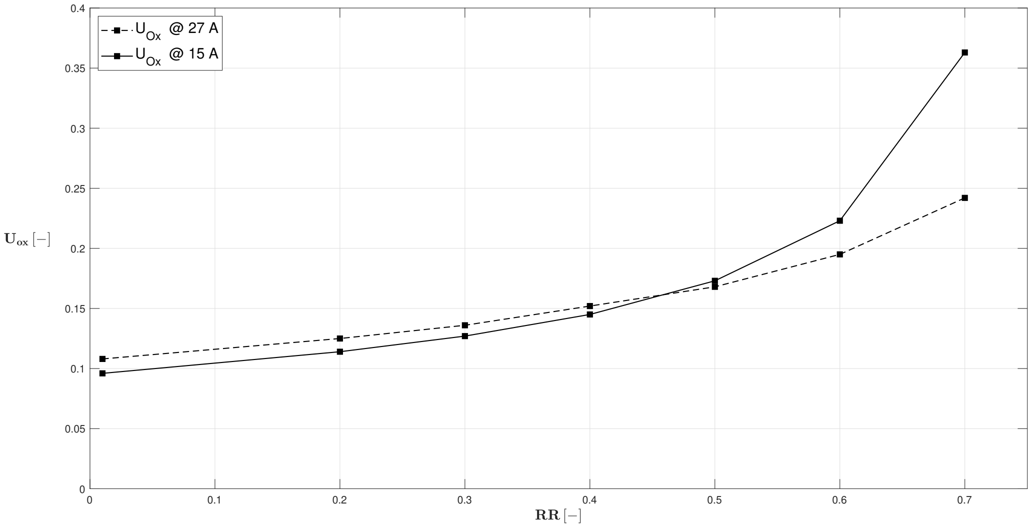

Figure E.8: Influence of recirculating ratio on the oxygen utilization. The comparison between I_{stack} = 15 A and I_{stack} = 27 A is shown.

Appendix F

Dynamic simulations

The figures below shows the results obtained when a current ramp of 0.25 A/min is applied during a load transient. In particular, Figures F.1, F.2 and F.3 show the profile of the stack inlet and outlet and the afterburner outlet molar composition during the load change. While Figure F.4 shows the temperature profile of the air and fuel flows. Specifically $T_{a,in}$ and $T_{f,in}$ represent the temperature of the air and fuel flow entering the stack, while $T_{f,out,HEx}$ represents the temperature at the fuel HEx outlet, thus at the adiabatic mixer inlet.

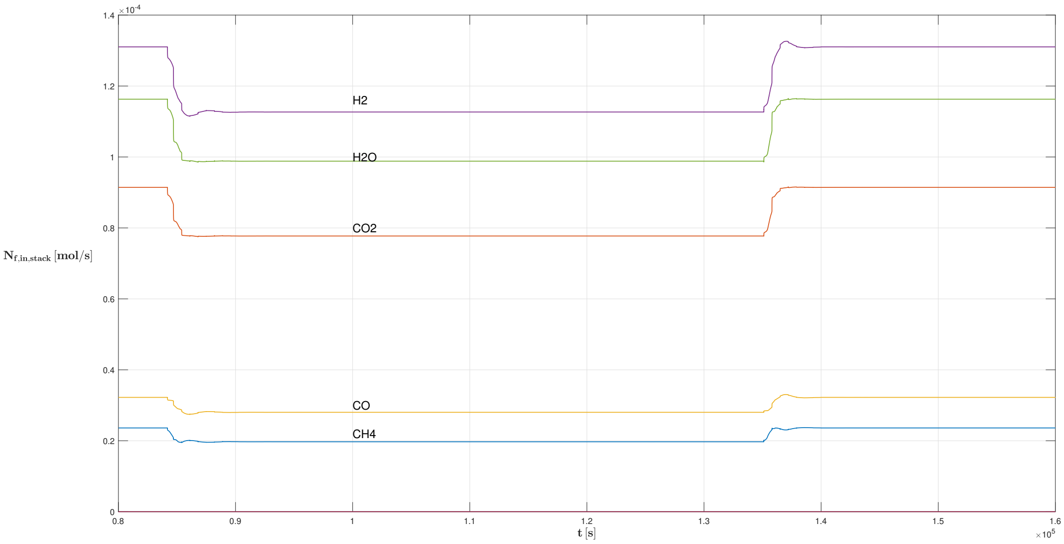

Figure F.1: Stack inlet composition during load transient.

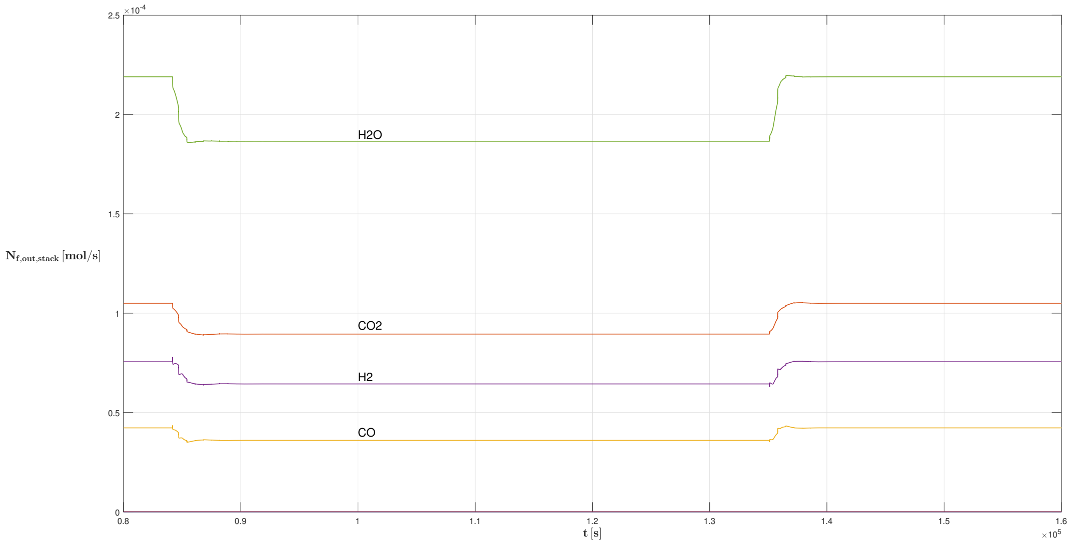

Figure F.2: Stack outlet composition during load transient.

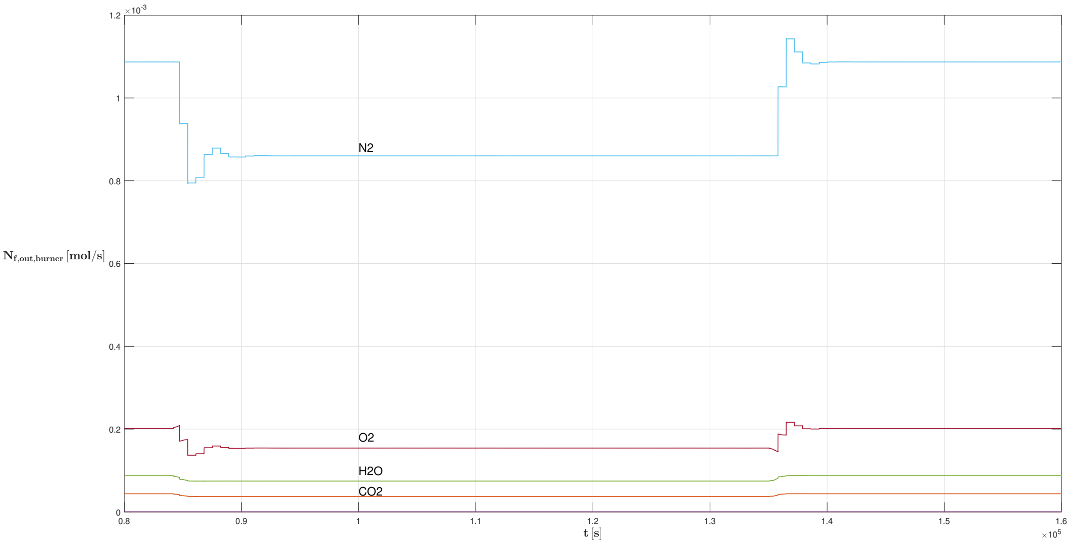

Figure F.3: Afterburner outlet composition during load transient.

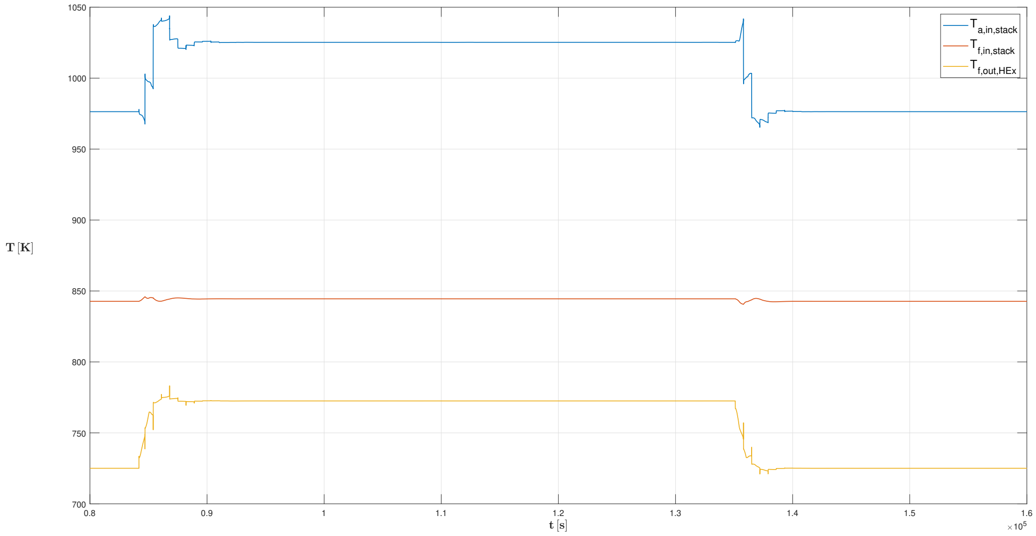

Figure F.4: Main flows operating temperature during load transients.

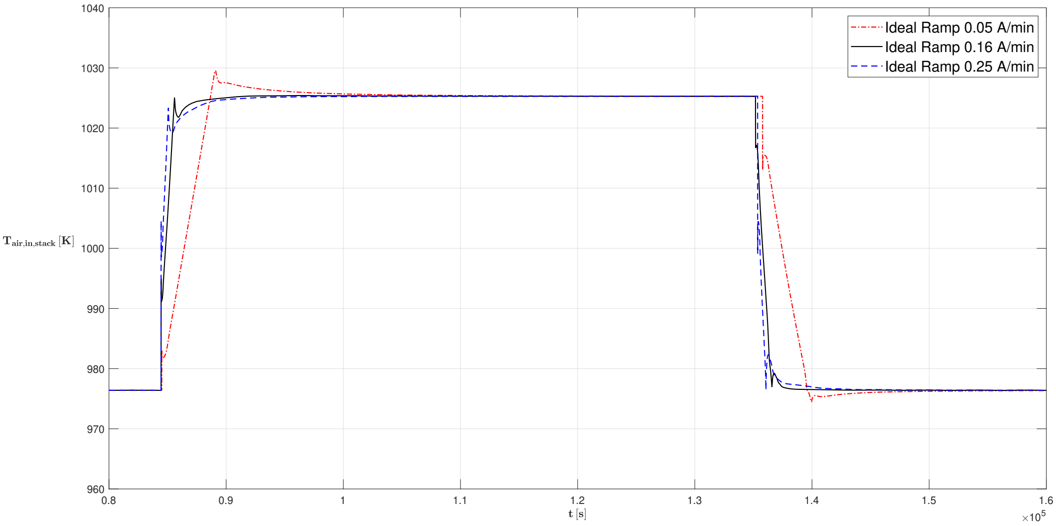

Figure F.5: Temperature of the air flow entering the stack for different ramp values using ideal control.

Acknowledgements

The past two years have been quite a journey. I had the privilege to meet and work with very interesting people and some of them have now become dear friends. I will take this opportunity to thank all those who have contributed, in their own way, to the conclusion of this adventure.

First, I would like to express my gratitude to my supervisor Dr. Ir. Lindert van Biert. Thank you Lindert for introducing me to the world of fuel cells and for giving me the chance of studying this very interesting topic. I think it is safe to say that your contribution has been fundamental for the completion of this work.

A special thanks to my supervisor Ir. Benny Mestemaker and the Royal IHC MTI team. Thank you for giving me the opportunity to work in such a nice environment.

Friends are the key point for a happy life. Thank you Dani, Kaan, Spyros, Lorenzo, Alfredo and Clemens for all the moments spent together and all the nice dinners. This journey would have not been the same without you all.

La famiglia viene prima di tutto. Ringrazio i miei genitori per avermi dato la possibilità di intraprendere questo traguardo e per tutti i loro insegnamenti. Le mie sorelle per la loro pazienza e la loro comprensione. Ringrazio i miei futuri cognati Luca, Francesco e Pierino perchè a modo loro hanno contribuito al raggiungimento di questo traguardo. Un ringraziamento speciale al nuovo arrivato Carmine. I tuoi sorrisi e i tuoi sguardi sono stati una perfetta distrazione durante le lunghe giornate passate davanti al pc. Benvenuto in questa pazza famiglia.

Un ringraziamento speciale a Mario, Carmela, Glenda, Iride e Lorenzo. Siete una seconda famiglia per me. Grazie per il supporto e la comprensione, specialmente negli ultimi mesi. Ringrazio tutta la truppa di Prenotazioni di Palma. Tornare giù è sempre un piacere. Grazie Carlo, Roberto e Neloy per esserci sempre stati. Sono contento che la distanza non ci abbia divisi. Siete degli amici davvero preziosi.

E questo mi porta ad una persona davvero speciale. Dafne, sei e sarai sempre la parte più importante della mia vita. Hai seguito tutti i miei traguardi e mi sei sempre stata accanto. Grazie della pazienza che hai avuto con me durante questo lungo perido e sopratutto durante la quarantena. Non so come avrei fatto se non ci fossi stata tu. Grazie per continuare a sopportarmi e supportarmi anche dopo 9 anni insieme. Grazie per tutti i momenti passati insieme. Sei l'amore della mia vita. Non vedo l'ora di scoprire cosa il futuro ha in servo per noi.

Pietro Uva, Delft, September 2020